

INFORMATION TO USERS

This manuscript has been reproduced from the microfilm master. UMI films the text directly from the original or copy submitted. Thus, some thesis and dissertation copies are in typewriter face, while others may be from any type of computer printer.

The quality of this reproduction is dependent upon the quality of the copy submitted. Broken or indistinct print, colored or poor quality illustrations and photographs, print bleedthrough, substandard margins, and improper alignment can adversely affect reproduction.

In the unlikely event that the author did not send UMI a complete manuscript and there are missing pages, these will be noted. Also, if unauthorized copyright material had to be removed, a note will indicate the deletion.

Oversize materials (e.g., maps, drawings, charts) are reproduced by sectioning the original, beginning at the upper left-hand corner and continuing from left to right in equal sections with small overlaps.

**ProQuest Information and Learning
300 North Zeeb Road, Ann Arbor, MI 48106-1346 USA
800-521-0600**

UMI[®]

**3D ORBITAL NAVIGATORS FOR MEASUREMENT
OF HEAD MOTION IN ECHO PLANAR
MAGNETIC RESONANCE IMAGING**

by

Najmeh Khalili Mahani, B. Eng.
Department of Biomedical Engineering,
Faculty of Medicine

A thesis submitted to the Faculty of Graduate Studies and Research
in partial fulfillment of the requirements of the
degree of Master of Engineering

McGill University, Montreal, QC, CANADA

July 2001



**National Library
of Canada**

**Acquisitions and
Bibliographic Services**

**395 Wellington Street
Ottawa ON K1A 0N4
Canada**

**Bibliothèque nationale
du Canada**

**Acquisitions et
services bibliographiques**

**395, rue Wellington
Ottawa ON K1A 0N4
Canada**

Your file Votre référence

Our file Notre référence

The author has granted a non-exclusive licence allowing the National Library of Canada to reproduce, loan, distribute or sell copies of this thesis in microform, paper or electronic formats.

The author retains ownership of the copyright in this thesis. Neither the thesis nor substantial extracts from it may be printed or otherwise reproduced without the author's permission.

L'auteur a accordé une licence non exclusive permettant à la Bibliothèque nationale du Canada de reproduire, prêter, distribuer ou vendre des copies de cette thèse sous la forme de microfiche/film, de reproduction sur papier ou sur format électronique.

L'auteur conserve la propriété du droit d'auteur qui protège cette thèse. Ni la thèse ni des extraits substantiels de celle-ci ne doivent être imprimés ou autrement reproduits sans son autorisation.

0-612-75270-4

ABSTRACT

This thesis presents a motion compensation method based on *orbital navigator* echoes that measure the movement of a subject between subsequent acquisitions of a magnetic resonance image (MRI). The 3D orbital navigator method proposed addresses the speed requirements of a fast acquisition technique, namely echo planar imaging (EPI), used in functional MRI. Three orthogonal magnetic field gradient pulses were designed and implemented to produce circular sampling trajectories in the volume of the resonating spins of the subject under study. The variations in phase and magnitude of the subsequent navigator data samples serve as markers for motion occurring between repeated acquisitions. Algorithms to estimate the parameters of motion from the navigator signals were developed and their correctness and stability in the presence of noise were tested by means of numerical simulation. The phantom studies involving controlled rotation and displacement of an inhomogeneous test object during an MRI acquisition established the technique's accuracy. In-vivo experiments showed that the navigator echoes can be used in measuring the gross patient movement, as well as in monitoring the small displacements that may correlate with the respiratory cycle.

RÉSUMÉ

Cette thèse présente une méthode de compensation du mouvement, basée sur les échos du navigateur orbital, mesurant le mouvement d'un sujet entre acquisitions successives d'une image de résonance magnétique (IRM). La technique de navigateur orbital 3D proposé rencontre les conditions d'une technique d'acquisition rapide, à savoir la formation d'image planaire écho(IPE), utilisée dans l'IRM fonctionnelle. Trois impulsions de gradient magnétiques orthogonaux ont été conçues et mises en application pour produire des trajectoires circulaires de prélèvement dans le volume des spins de résonance magnétique du sujet. Les variations de phase et d'amplitude d'échantillons successifs de données du navigateur servent à repérer le mouvement entre acquisitions. Des algorithmes pour estimer les paramètres du mouvement des signaux de navigateur furent développés et leur exactitude et stabilité en présence de bruit testées au moyen de simulation analytique. Les études *in-vitro* impliquant une rotation contrôlée et le déplacement d'un fantôme non-homogène pendant une acquisition d'IRM ont démontré la précision de cette technique. Les expériences *in-vivo* ont démontré que les échos du navigateur peuvent être utilisés pour mesurer le mouvement brut du sujet, aussi bien que pour surveiller des petits déplacements, possiblement corrélés avec le cycle respiratoire.

Acknowledgment

In the past three years, I have been indebted to many a colleague who have provided me with invaluable intellectual support and friendship. I wish to thank Dr. Bruce Pike, my supervisors, whose great intelligence has granted me a view into the majestic field of MRI and neuroscience, not to forget his patience, generosity and humor that have eased the long journey of my thesis into a pleasant one. I am grateful to Dr. John Sled without whose flashing hints I would have remained lost in the dark labyrinths of statistical confusion. Special thanks to Valentina Petre and Dr. Alex Zijdenbos, who took my hand not only in friendship, but also in the *minc* tracks of *minctracc* . I owe my data validation to Mr. Eric Johnston who built the motion measurement set up for my phantom studies and to Mr. Christian Duval who shared his sophisticated laser motion sensors with me. Without the wonderful support of Andreas Lazda, Brad Gill and Jennifer Campbell I would not have endured, at times frustrating, process of programming the MR scanner. Many thanks to Bojana Stefanovic, Marguerite Wiekovska, Peter Petric and Ives Leveques who have made me the most comfortable in the lab during the writing of my thesis. The cooperation of the MR technicians is gratefully acknowledged. I wish to thank Ms. Pina Sorrini for her kind support and advice with regards to the administrative issues. Special thanks to Dr. Veronique Bohbot (and little Nikolas) who found me some time to translate the abstract in the last minute.

I thank Dr. Christopher Trueman whose encouragement and unparalleled mentorship extended well beyond the years that I worked in his lab as an undergraduate research assistant.

And, my fondest appreciation go to my husband, Reza Adalat, without whose loving care and support, without whose patience and selflessness, absolutely none would have been possible.

The financial support from the Natural Science and Engineering Research Council and The Canadian Institute for Health research are thankfully acknowledged.

TABLE OF CONTENTS

LIST OF FIGURES	8
GLOSSARY	9
CHAPTER 1	10
INTRODUCTION	10
CHAPTER 2	15
THEORETICAL BASIS OF MRI	15
2.1 <i>Nuclear Magnetic Resonance Phenomenon</i>	15
2.2 <i>Relaxation</i>	18
2.2.1 <i>Spin-Spin relaxation</i>	18
2.2.2 <i>Spin-Lattice Relaxation</i>	19
2.3 <i>Sources of MRI Signal</i>	19
2.3.1 <i>Sources of contrast</i>	19
2.3.2 <i>Spatial Localization of NMR Signal</i>	22
2.3.3 <i>Reconstruction Techniques</i>	25
2.4 <i>Image Resolution</i>	29
CHAPTER 3	31
FUNCTIONAL MAGNETIC RESONANCE IMAGING	31
3.1 <i>Sources of Signal in fMRI</i>	31
3.1.1 <i>Physiology of brain activation</i>	31
3.1.2 <i>Susceptibility induced signal due to brain activation</i>	33
3.1.3 <i>Perfusion measurement</i>	34
3.1.4 <i>ASL versus BOLD</i>	34
3.2 <i>FMR Imaging Sequences</i>	35
3.2.1 <i>Echo Planar Imaging</i>	35
3.2.2 <i>Fast Low Angle Shot (FLASH) Excitation</i>	38
3.2.3 <i>GRE vs. SE</i>	38
3.3 <i>Sources of Artifact in fMRI</i>	40
3.3.1 <i>EPI-related artifacts</i>	40
3.2.2 <i>Susceptibility-induced artifacts</i>	40
CHAPTER 4	42

THEORETICAL FORMULATION OF MOTION	42
4.1 <i>Inter-View versus Intra-View Motion</i>	42
4.2 <i>Effect of Displacement</i>	43
4.3 <i>Effect of Rotation</i>	44
4.4 <i>Effects of Velocity and Acceleration</i>	45
4.5 <i>Effects of Flow</i>	45
4.6 <i>Physiological Motion</i>	46
CHAPTER 5	49
MOTION COMPENSATION TECHNIQUES	49
5.1 <i>Motion Effect Reduction</i>	49
5.1.1 Gradient moment nulling	50
5.1.2 Phase-encode ordering	51
5.1.3 Modified acquisition techniques	52
5.2 <i>Motion Prevention Techniques</i>	53
5.2.1 Physical restraining	53
5.2.2 Acquisition control	54
5.3 <i>Motion Detection and Correction</i>	54
5.3.1 Motion estimation from data and post processing	54
5.3.2 Motion detection by navigator echoes	57
5.3.2.1 Diffusion weighted imaging with navigator echoes	58
5.3.2.2 fMRI with navigator echoes	60
CHAPTER 6	61
3D ORBITAL NAVIGATORS:	61
DESIGN AND IMPLEMENTATION	61
6.1 <i>Introduction</i>	61
6.2 <i>Pulse Sequence Design</i>	61
6.3 <i>Pulse Sequence Implementation</i>	66
6.4 <i>Correction Algorithms</i>	67
6.4.1 Detection of rotation angle and in-plane displacement	67
6.4.2 Correction	70
CHAPTER 7	73
3D-ORBITAL NAVIGATORS: EXPERIMENTS	73
7.1 <i>Numerical Simulations</i>	73
7.1.1 Methods	73
7.1.2 Results	76
7.1.3 Discussion	76
7.2 <i>Phantom Experimentss</i>	79
7.2.1 Methods	79
7.2.2 Test of translation	81
7.2.2.1 Results	81
7.2.2.2 Discussion	81
7.2.3 Test of rotation	84
7.2.3.1 Results	84
7.2.3.2 Discussion	84

7.2.4 Complex motion	87
7.2.4.1 Results	87
7.2.4.2 Discussion	88
7.3 <i>In-Vivo Human Experiments</i>	89
7.3.1 Gross subject motion	89
7.3.1.1 Methods	89
7.3.1.2 Results	90
7.3.1.3 Discussion	90
7.3.2 Monitoring the respiratory cycle	90
7.3.2.1 Method	90
7.3.2.2 Result	90
7.3.2.3 Discussion	91
CHAPTER 8	97
CONCLUSION	97
8.1 <i>Summary</i>	97
8.2 <i>Future Work</i>	99
REFERENCES	100

List of Figures

Figure	Title	Page
2.1	Spin alignment in presence of external B-field	13
2.2	RF-excitation and transverse magnetization	14
2.3	Contrast variation with sequence	19
2.4	Slice selection	22
3.1	Standard 2DFT vs EPI	34
5.1	Gradient moment nulling	48
5.2	Effect of motion on back-projection vs 2DFT acquisition	50
6.1	Orbital Navigator waveform and trajectory	61
6.2	Effect of flip angle on signal intensity	62
6.3	Navigator-mounted EPI sequence	62
6.4	Navigator based motion correction algorithm	70
7.1	Digital Radon Phantom	72
7.2	Reconstructed Radon phantom from analytical Fourier expression	73
7.3	Magnitude and phase behavior of simulated navigator	73
7.4	Sensitivity of motion detection algorithm to different noise levels	75
7.5	Accuracy of simulated rotation detection	76
7.6	Accuracy of simulated translation detection in X direction	76
7.7	Accuracy of simulated translation detection in Y direction	77
7.8	Agar phantom and movement mechanism	78
7.9	Magnitude and phase of navigator due to stepwise displacement	80
7.10	Calculated displacements	80
7.11	Accuracy of calculated displacements	81
7.12	Example of displacement correction	81
7.13	Magnitude and phase of navigators due to stepwise rotation	83
7.14	Accuracy of calculated rotation	84
7.15	Effect of rotation angle on correlation coefficient of the magnitude of the navigators	84
7.16	Accuracy of rotation detection	85
7.17	Example of rotation correction	85
7.18	Interleaved rotation and displacement	86
7.19	Accuracy of detection of complex motion	87
7.20	Measurement of sagittal in vivo movements	89
7.21	Effect of motion correction on difference signal	90
7.22	Example of in-vivo motion correction	90
7.23	Motion induced by breathing	92
7.24	Regional correlation of the brain movement with the breathe cycle	93
Table 2.1	Different pulse sequences and signal intensity equations	18
Table 2.2	Reconstruction techniques and corresponding sequences	25

Glossary

ω	Larmor frequency
ADC	Analogue to digital converter
ASl	Arterial spin labeling
B_0	Static magnetic field
B_1	Radiofrequency field
BOLD	Blood oxygen level dependant
CBF	Cerebral blood flow
CBV	Cerebral blood volume
DWI	Diffusion weighted imaging
EPI	Echo planar imaging
FLASH	Fast low angle shot
fMRI	Functional MRI
FOV	Field of view
$G(t)$	Gradient field vector
GMN	Gradient moment nulling
GRE	Gradient recalled echo
ICMR _{GL}	Local metabolic rate of glucose
ICMR _{O2}	Local metabolic rate of oxygen
M	Magnetization vector
M_0	Net magnetization
MRI	Magnetic resonance imaging
M_{xy}	Transverse magnetization
M_z	Longitudinal magnetization
NMR	Nuclear magnetic resonance
RF	Radiofrequency
SE	Spin echo
SNR	Signal to noise ratio
T_1	Spin-lattice relaxation time
T_2	Spin-spin relaxation
TE	Time of echo
TR	Time of Repetition

Chapter 1

INTRODUCTION

Artifacts in any imaging modality can hinder reliable interpretation of the images. Eddy currents, field and tissue inhomogeneity, inadequate or residual radiofrequency (RF) excitation, chemical shift, and motion, to name a few, are sources of artifacts in magnetic resonance imaging(MRI). Restoring an MR image from blurring, ghosting, intensity inhomogeneity, colored and white noise, and edge ringing effects is the purpose of many a researcher's investigation; this thesis focuses on one method of eliminating motion-induced artifacts.

Motion artifacts in MRI vary with the source of motion, the capabilities of the imaging equipment and the image acquisition methods. The nature of the artifact, whether it is a simple shift in the boundaries of the image, a blurred anatomy, ghosting, or a total shape distortion, depends not only on the extent of displacement but also on when during an image acquisition it happens. These factors will be thoroughly explained throughout this thesis but a few brief examples will serve to illustrate the complexity of the problem of motion compensation. Periodic and unrestrainable moving organs, such as heart and chest, or gross patient movement can cause signal degradation, blurring or ghost images that replicate across the field of view and can undesirably mask or mimic

pathology. Another complexity is the variability of the effects that the same source of motion has on different imaging methods. For instance, the ghosts in a multi-slice 2D spin-warp image, acquired by scanning the volume on a Cartesian grid, repeat themselves along the x-, y- or z-axis, depending on the direction of the motion and the direction of sampling, while those in a three dimensional (3D) projection reconstruction, which is based on scanning the volume along spokes in a 3D spherical coordinate system, appear at a radial distance from the image. Furthermore, determining the time course of motion with respect to the speed of scanning can provide information on how to optimize the imaging procedure for minimized artifacts.

Ideally, one would like to make the images as resistant as possible to any source of motion, be it flow, rigid displacement or nonlinear deformation (such as breathing). It is also desirable to prevent motion-induced inconsistencies between subsequent acquisitions of multiple frames of a repeating acquisition, even if each individual image is artifact free.

The prime goal of any motion compensation research is to minimize the artifacts as much as possible and to extract the parameters of motion, such as coordinates of displacement, as well as its velocity, acceleration and pulsatility, during or after acquisition, such that the effects can be perfectly reversed. While all the above can be mathematically realized and digitally simulated, MRI is constrained by physics, physiological and engineering facts and compromises. Fast imaging reduces the occurrence of motion during acquisition of a frame, be it a line, a slice or a volume, but it requires specialized hardware and it often lowers signal to noise ratio and image resolution. Monitoring of cardiac and respiratory cycles and imaging during the still periods can eliminate periodic ghost artifacts. Measurement of the rigid body displacement during acquisition can be used to improve the reconstructed image. Nevertheless, both these techniques increase the imaging time. Rough approximation of changes in the boundary conditions of moving tissues, resulting in shape distortion and inhomogeneity artifacts, is far from accurate because boundary conditions vary with the anatomy.

Presently, there are three general approaches to the problem: motion prevention, motion correction and motion artifact reduction. Motion prevention ranges from simple restraining of the subject to sophisticated real-time re-acquisition of motion-contaminated data. Motion correction techniques range from post processing of reconstructed images to measurement and estimation of phase deviations between different measurements of the same object. Motion artifact reduction techniques rely on modified acquisitions that minimize the susceptibility to phase error due to microscopic and macroscopic movement. Gradient moment nulling, modified trajectories and fast imaging techniques fall in this category by improving the robustness of the imaging sequence against phase related imperfections. Techniques such as gating and triggering, often combined with those above, synchronize the data acquisition with the periodic motion pattern of the subject.

The choice of motion detection methodology depends, to a great extent, on the requirements of the imaging technique. MRI has long produced exquisite anatomical images. As functional MRI is becoming a routine diagnostic tool, demands on quality are increasing and the necessity of producing fast and stable images is becoming paramount. Functional MRI relies on measuring the signal changes, induced by increased metabolism of neurons activated during the performance of a certain task or responding to a specific stimulus. fMRI involves repeated acquisition of MR images while the subject is presented with a periodic stimulus or task. Given that the signal changes due to cerebral metabolism are focused in a very small region (or regions), any intra-view motion, i.e. motion *during* acquisition of a frame, degrades the MR signal, making fast imaging indispensable. Furthermore, since activation maps are obtained by statistical analysis of small signal changes between repeated measurements of like frames, eliminating any factor such as small inter-view motion, i.e. motion *between* acquisition of different frames, that produces inconsistency is crucial.

This thesis is motivated by increased interest in functional MRI studies of the brain, that necessitate motion monitoring and correction prior to performing post-

processing statistical analyses. In fMRI, small motion or misalignment of frames can produce signal intensity variations that lead to erroneously interpreted activation. The statistical analysis of the data does, in most cases, average out the random motion effects at the expense of experimental SNR. Monitoring motion might also bear interesting physiological information or provide insight as to how stimulus correlated motion affects the experiment. To accommodate as many of these requirements as is feasible, *orbital navigators* are implemented as a tool to measure the inter-view motion-related variability. Navigator in MRI refers to an invariant acquisition of a fraction of the entire magnetic resonance signal, between the acquisition of different views. Usually an arbitrary navigator is assumed as the reference and the phase and magnitude of the subsequent navigators are compared against the reference one in order to extract the parameters of motion, i.e. the extent and the orientation of the displacement and/or rotation. The relevant principles of MRI are described in the following chapters. To put the concept of navigators in a context, suffice it to say here that the MR signal can be described in terms of the spatial Fourier transformation of the spin distribution. Depending on how navigators traverse the coordinates of the Fourier space, they are categorized as linear, orbital or spiral. Although the mathematical formulation of the problem varies with the shape of navigator trajectories, the principle is that translational and rotational movement of the object in an NMR experiment results in phase and amplitude shifts in the raw (Fourier) MR signal, respectively.

The orbital navigators proposed here are three perpendicular circles in frequency (or Fourier) space. Each circle is formed by two orthogonal sinusoidally-varying magnetic field gradients. The radius of the orbital navigator, determined by the amplitude and duration of the gradient fields, determines the resolution of motion detection. The NMR signal is acquired simultaneously with the formation of the orbital trajectories of the navigators.

While the circular sampling of data space simplifies the algorithm to calculate rotation, the abundance of data points, sampled at a constant radius, increases the accuracy of finding the displacement coordinates. The orbital navigators are formed and

acquired in a few milliseconds and do not affect the repetition time between different frames. Since fMRI experiments are based on periodic tasks being performed during imaging, the repetition time between acquisitions is of great importance. Based on these considerations, this project examines the robustness and sensitivity of orbital navigator-based motion detection in fMRI.

The theory of nuclear magnetic resonance (NMR) and the physics of MRI are reviewed in the next chapter. In Chapter Three, the principles of functional MRI, basics of echo planar imaging (EPI) and the sources of artifacts in fMRI are introduced. In the fourth chapter, the types and effects of motion, be it rigid body movement or periodic physiological displacements, are discussed and formulated. A review of the literature on motion correction and/or detection methods in Chapter Five lays the groundwork for our choice of the 3D orbital navigator technique. In Chapter Six, our gradient design and the correction algorithm implementation are presented. The experimental results and the accuracy of correction algorithm are examined in Chapter Seven. Concluding remarks in chapter eight provide a summary of the project and discuss future work.

Chapter 2

THEORETICAL BASIS OF MRI

Magnetic resonance imaging (MRI) is a non-invasive technique that has been in use for exquisite anatomical imaging for almost 20 years. It is now evolving to open an insightful eye into a variety of features including the chemical state of tissue, blood circulation, and physiological changes pertinent to neuronal activation, by means of methods such as MR spectroscopy (MRS), angiography (MRA) and functional MRI, respectively. This chapter is dedicated to a review of the basic principles of MRI relevant to the problem of motion correction. More complete introduction to the principles of MRI can be found in [1,2].

2.1 Nuclear Magnetic Resonance Phenomenon

The nuclear magnetic resonance (NMR) phenomenon is particular to nuclei(or spins) with an odd number of protons and/or neutrons in response to an external magnetic field. The basic phenomenon of NMR can be described in terms of quantum mechanics or classical mechanics, with the latter sufficing to treat the macroscopic behavior relevant to MRI.

A single proton can be thought of as positive charge uniformly distributed on a spinning sphere that gives rise to a magnetic moment which is co-linear with the angular

momentum of the nucleus, $\hbar\mathbf{I}^1$ (where \hbar is plank's constant (divided by 2π) and \mathbf{I} is the quantum mechanical spin which is integer or half integer). Although neutrons are electrically uncharged, they possess a charge inhomogeneity that induces a slightly lower magnetic moment of opposite direction. The opposing fields of pairing protons or pairing neutrons can eliminate the magnetic moment. For the purposes of medical NMR imaging, hydrogen, with a single proton, not only has the largest magnetic moment, it also is the most abundant nuclei in biological specimens, hence it is the nuclei of choice in MRI.

As depicted in Figure 2.1, in the absence of an external magnetic field, magnetic moments (or spins) of protons are randomly oriented and have zero net magnetization. If a volume of hydrogen atoms is immersed in a static magnetic field, governed by the quantum mechanics, the magnetic dipole moments assume either low or high energy levels and align parallel or anti-parallel to the direction of the static field, respectively. The vector sum of the magnetization vectors from all the spins results in the net magnetization, \mathbf{M}_0 , which is in the direction of \mathbf{B}_0 ², the applied static magnetic field.

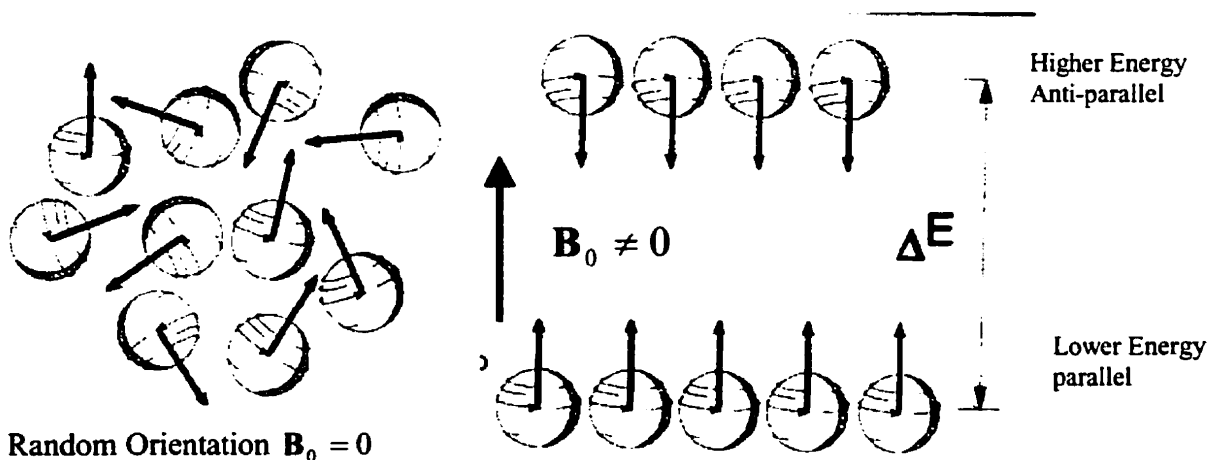


Figure 2.1: Randomly oriented hydrogen spins assume two possible energy states in the presence of an external magnetic field and align parallel or anti-parallel to the direction of the \mathbf{B}_0 field. A slightly greater number of protons exist in parallel direction and the vector sum of all the magnetic moments results in net magnetization along the direction of external field [1].

¹ Bold characters represent vector quantities.

² Adapting the conventional NMR coordinate system, the external magnetic field and the net magnetization vector at equilibrium are both along the z-axis.

Interaction of proton's magnetic moment with the external magnetic field results in a torque that induces a gyroscopic precession of the proton about its axis. The angular frequency of this precession, known as Larmor frequency is proportional to the strength of the magnetic field and the gyromagnetic ratio γ , which is particular to the atom type. Larmor frequency is described as:

$$\omega_0 = \gamma B_0 . \quad 2.1$$

For NMR signals to be detectable, the net magnetization vector must be tilted away from the thermal equilibrium discussed above into the transverse plane, i.e. the plane perpendicular to direction of the static field. This is achieved by applying an RF pulse of specific frequency. From the quantum mechanical point of view, for transition to take place, the frequency of B_1 (the RF pulse,) multiplied by the Plank's constant must be equal to the energy gap between the parallel and anti-parallel states of the magnetization. From the classical point of view, if the angular rotation of the magnetic field vector of the RF pulse occurs at the Larmor frequency ($\omega_0 = \gamma B_0$), the B_1 (RF) magnetic field appears stationary with respect to the rotating frame reference of the precessing spins. Keeping in mind that the B_1 field is in the transverse plane, as depicted in Figure 2.2, it tilts the net magnetization vector \mathbf{M} , away from longitudinal axis. The tilt angle and the size of the transverse magnetization vector depend on the amplitude and duration of the B_1 pulse.

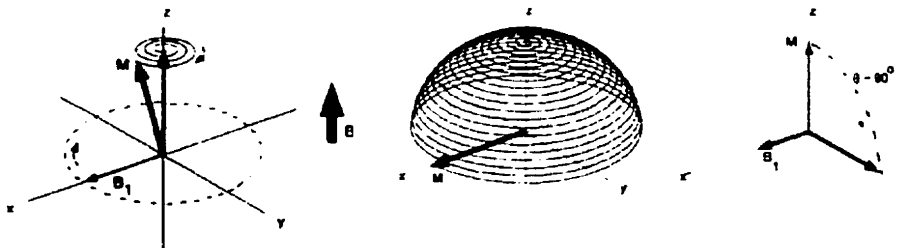


Figure 2.2: Schematic presentation of NMR signal induction due to 90° RF excitation. B_1 is at the precessional larmor frequency hence it appears stationary and perpendicular to the rotating net magnetization vector. B_1 generates a torque on \mathbf{M} which converts the longitudinal magnetization to transverse magnetization[2].

2.2 Relaxation

As the transverse component of \mathbf{M} precesses about the main field axis (z -axis), it induces an electromagnetic signal in an RF receiver coil placed perpendicular to the transverse plane. This signal decays with time due to loss of phase coherence of individual spins over time and is known as the free induction decay or FID signal. Spin-spin interactions, as well as internal and external field inhomogeneities enhance the dephasing of the transverse magnetization signal. The decay of transverse magnetization and its return to equilibrium, i.e. longitudinal magnetization, are exponential processes that constitute the relaxation mechanisms.

2.2.1 Spin-Spin relaxation

If the net magnetization is placed in the xy -plane it will rotate about the z -axis at Larmor frequency. In real life, the individual spin moments comprising M_{xy} experience a slightly different magnetic field. The local field perturbation, caused by neighboring nuclear dipoles or electron fields, results in a dispersion in Larmor frequencies and hence dephasing of the rotating magnetization vector. The longer the elapsed time, the greater the dispersion in precessional frequencies and hence greater the phase variation will be.

The time constant that describes the decay of the transverse magnetization, M_{xy} , is called the spin-spin relaxation time, symbolized as T_2 . The decay of M_{xy} is described as:

$$M_{xy}(t) = M_{xy}(0)e^{-t/T_2}. \quad (2.4)$$

In fact, two factors contribute to the decay of transverse magnetization: 1) molecular interactions, as mentioned before, lead to a pure T_2 effect; and 2) static variations in B_0 that lead to an enhanced dephasing effect. The combination of these two factors is what actually results in the decay of transverse magnetization in an FID. The combined time constant is called T_2^* (often pronounced T-two-star) and it comprises the

T_2 decay due to molecular processes as well as the effect of inhomogeneities in the magnetic field:

$$\frac{1}{T_2^*} = \gamma\Delta B_0 + \frac{1}{T_2} \quad (2.5)$$

Thus, the observed decay of M_{xy} in a FID is given by:

$$M_{xy}(t) = M_{xy}(0)e^{-t/T_2^*} \quad (2.6)$$

2.2.2 Spin-Lattice Relaxation

At equilibrium, the net magnetization vector is along the direction of the applied magnetic field (conventionally designated as z-axis). The time constant which describes the exponential growth of M_z to its equilibrium value following excitation is called the spin-lattice relaxation time (T_1). The equation governing this behavior as a function of the time, t , after its rotation into transverse plane (90° excitation) is:

$$M_z(t) = M_0(1 - e^{-t/T_1}). \quad (2.7)$$

In case of a 180° excitation, $M_z(0) = -M_0$, the magnetization vector is placed along the negative z-axis and its recovery is governed by

$$M_z(t) = M_0(1 - 2e^{-t/T_1}). \quad (2.8)$$

T_1 is therefore defined as the time constant for the exponential recovery of the longitudinal component of magnetization. The T_1 relaxation process depends on the interaction of excited spins with the molecular lattice that surrounds them.

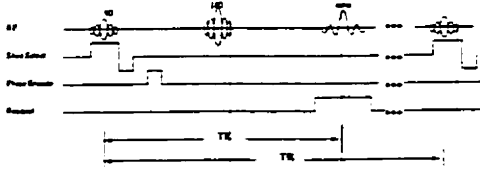
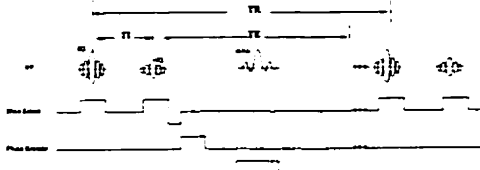
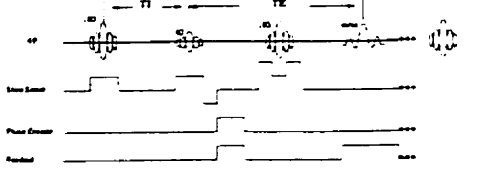
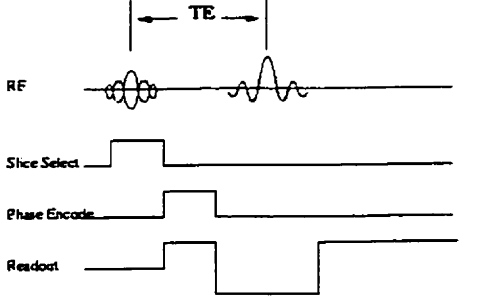
2.3 Sources of MRI Signal

2.3.1 Sources of contrast

In MRI, the contrast is dependant on not only on the number of nuclei present (proton density), which determines the magnitude of the net magnetization vector, but also on the relaxation characteristics that are determined by the timing, order, polarity and repetition frequency of the RF excitation and the gradient magnetic fields. A specifically ordered combination of RF and gradient pulses is known as a pulse sequence.

In order for a tissue type or pathology to be visible in an MR image, its signal intensity must differ from the adjacent tissues. The signal intensity, denoted as S , is determined by the specifications of the pulse sequence and the tissues NMR properties (T_1 , T_2 and proton density). Present MRI technology is founded on three basic pulse sequence techniques : spin echo, inversion recovery, and gradient recalled echo sequences. The intrinsic contrast variables are 1) spin-lattice relaxation time or T_1 , 2) spin-spin relaxation time T_2 or , 3) proton density, PD and 4) T_2^* . A detailed discussion of how different pulse sequences result in different contrast is beyond the scope of this report. Suffice it to say that the RF pulse envelope and its duration determine the excitation pulse angle that, long with proton density, repetition time (TR), and the time of echo (TE), defines the contrast characteristics of the image. The signal intensity equations of the basic pulse sequence types are presented in Table 2.2. In this table, P is a function of proton density, multiplied by a constant factor that depends on the sensitivity of the imaging circuitry, e.g. the strength of the static magnetic field and the gain of the receiver coil. Figure 2.3 illustrates the instrumental role of TR, TE , T_1 , T_2 and the RF flip angle in differences in image contrasts.

Table 2.1 Different pulse sequences and their corresponding signal intensity equations.

<p>Spin Echo</p>	$S = P(1 - e^{-\frac{-TR}{T1}})e^{-\frac{-TE}{T2}}$	
<p>Inversion Recovery (180°-90°)</p>	$S = P(1 - 2e^{-\frac{TI}{T1}} + e^{-\frac{TR}{T1}})$	
<p>Inversion Recovery- Spin Echo (180°-90°-180°)</p>	$S = P(1 - 2e^{-\frac{TI}{T1}} + e^{-\frac{TR}{T1}})e^{-\frac{TE}{T2}}$	
<p>Gradient Recalled Echo</p>	$S = P(1 - e^{-\frac{TR}{T1}}) \frac{\sin \theta e^{-\frac{TE}{T2}}}{1 - \cos \theta e^{-\frac{TR}{T1}}}$	

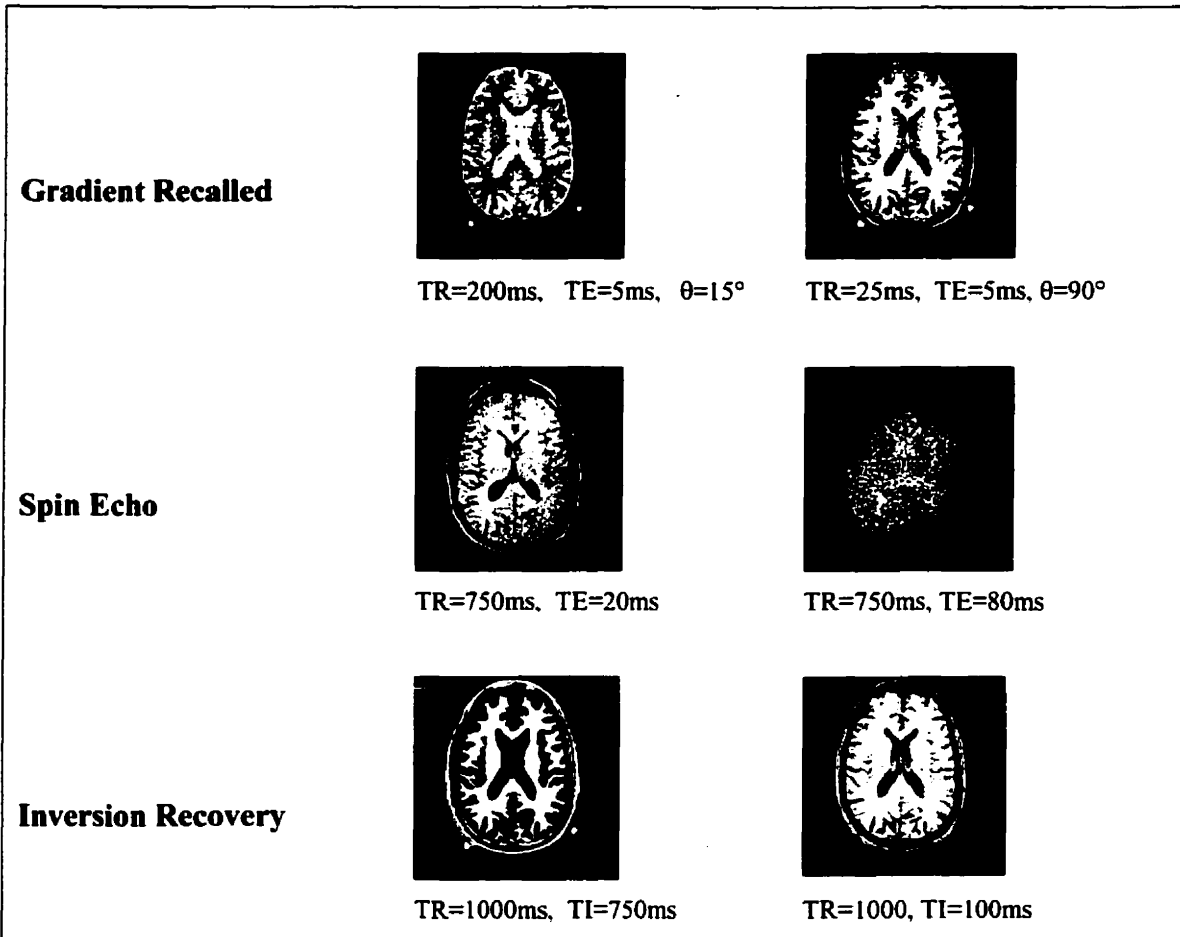


Figure 2.3: The contrast characteristics of an image vary with the acquisition protocol as well as the timing specifications of a sequence. It is possible to obtain different contrast information, from the same acquisition sequence, by varying the echo and repetition times of the imaging paradigm.

2.3.2 Spatial Localization of NMR Signal

So far, it has been shown that certain nuclei, immersed in a static homogeneous field and under influence of an RF excitation, begin resonating and emit a signal whose amplitude is regulated by the spin density and relaxation characteristics. To localize a signal, its phase and frequency are forced to vary with spatial coordinates. This is achieved by superimposing a spatially variant magnetic field $G(x, y, z, t)$ – a gradient, upon the homogeneous static field that varies the Larmor frequency of the nuclei,

described in equation 2.1, along the coordinate system of the gradient fields. In general, the behavior of a magnetization vector is described by the Bloch equation [2]:

$$\frac{d\mathbf{M}}{dt} = \mathbf{M} \times \gamma \mathbf{B} - \frac{M_x \mathbf{x} + M_y \mathbf{y}}{T_2} - \frac{(M_z - M_0) \mathbf{z}}{T_1} \quad (2.8)$$

where

$$\mathbf{M} = M_x \mathbf{x} + M_y \mathbf{y} + M_z \mathbf{z}, \quad (2.9)$$

denotes the transverse and longitudinal components of net magnetization vector and

$$\mathbf{B} = \mathbf{B}_0 + \mathbf{B}_1(t) + \mathbf{G}(t), \quad (2.10)$$

where

$$\mathbf{B}_0 = B_0 \mathbf{z} \quad (2.11)$$

$$\mathbf{B}_1(t) = B_1(t)(\cos \omega_0 t \mathbf{x} - \sin \omega_0 t \mathbf{y}) \quad (2.12)$$

$$\mathbf{G}(t) = G_x(t) \mathbf{x} + G_y(t) \mathbf{y} + G_z(t) \mathbf{z} \quad (2.13)$$

represent the static magnetic field, the RF pulse rotating at Larmor frequency in a plane perpendicular to the direction of the main magnetic field, and the gradient fields, respectively.

To be able to determine the position of spins, each region should experience a unique magnetic field. This is achieved by magnetic field gradients. Assuming time varying linear gradient fields, $G_x(t)$, $G_y(t)$ and $G_z(t)$, the precessional frequency experienced by nuclei at coordinates x , y , and z at time t will be

$$\omega(x, y, z, t) = \gamma(B_0 + G_x(t)x + G_y(t)y + G_z(t)z). \quad (2.14)$$

Applying an RF pulse at Larmor frequency $\omega_0 = \gamma B_0$ and solving the Bloch equation for the transverse magnetization will give :

$$M(x, y, z, t) = M_0(x, y, z) e^{-t/T_2(x, y, z)} e^{-i\omega_0 t} e^{-i \int_0^t \gamma(G_x(\tau)x + G_y(\tau)y + G_z(\tau)z) d\tau} \quad (2.15)$$

where M_0 describes the longitudinal magnetization at the time of excitation.

In an ideal MRI systems, the RF receiver coil is uniformly sensitive over the entire volume of interest, hence the detected signal is a uniformly weighted summation of all precessing transverse magnetization in the volume,

$$S_r(t) = \iiint_{x,y,z} M(x,y,z,t) e^{-i(\omega_0 t + \gamma \int_0^t \tilde{G}(x,y,z,\tau) d\tau)} dx dy dz, \quad 2.16$$

where $M(x,y,z)$ is a function of NMR parameters such as proton density, T_1 and T_2 , as defined by the Bloch equation.

Assuming a rotating frame of reference, the base band signal $S(t)$ can be obtained by demodulating $S_r(t)$ with the larmor frequency ω_0 :

$$S(t) = S_r(t) e^{+i\omega_0 t} \quad 2.17$$

or

$$S(t) = \iiint m(x,y,z) e^{-i2\pi[k_x(t)x + k_y(t)y + k_z(t)z]} dx dy dz \quad 2.18$$

where

$$m(x,y,z) = M(x,y,z,t) e^{-i\gamma\omega_0 t} \quad 2.19$$

and

$$k_x(t) = \frac{\gamma}{2\pi} \int_0^t G_x(t) d\tau \quad 2.20$$

$$k_y(t) = \frac{\gamma}{2\pi} \int_0^t G_y(t) d\tau$$

$$k_z(t) = \frac{\gamma}{2\pi} \int_0^t G_z(t) d\tau$$

denotes the spatial frequency variables defined as k-space in a spatial Fourier transformation domain . The signal equation 2.18 represents a 3D Fourier transformation indicating that the baseband signal is formed by a volume integral of magnetization multiplied by a spatially dependent phase factor. Therefore, the magnetization function of the object, $m(x,y,z)$, can be retrieved from the measured signal $S(t)$, by means of inverse Fourier transformation, given that the trajectory of $S(t)$ has covered sufficient part of the k-space [2].

As indicated by equation 2.20, the sampling trajectories are defined by integrating the gradient vectors whose amplitude determines the speed of covering the k-space. Flexibility to generate different gradient waveforms and sample on trajectories of different shapes has extended MRI beyond the capabilities of CT and PET scanning.

2.3.3 Reconstruction Techniques

The principles of NMR image reconstruction revolves around Fourier transformation of the raw data but the details of transformation (i.e. integration paths) vary with the coordinates of the k-space trajectory -- determined by the gradient waveforms-- over which the NMR signals are collected (Table 2.2).

By far the simplest and most common reconstruction technique in MRI is the 2DFT method. To obtain a 2DFT-MRI, the RF excitation must be restricted to a slice of a given thickness. The process of slice selection involves confining the resonance frequency of the slice to a narrow bandwidth, $\Delta\omega$, by applying a perpendicular linear gradient, simultaneously with a shaped RF pulse of $\Delta\omega$ bandwidth (Figure 2.4).

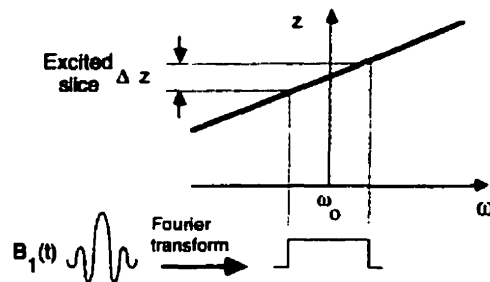


Figure 2.4: Schematic representation of interaction of gradient field with RF pulse in slice selection. To obtain a rectangular slice profile, a sinc shaped RF pulse is applied during the slice-select gradient. This translates into a Fourier transformation of the sinc function, which is a rect whose width is determined by the the bandwidth of the RF, as well as the slope of the slice select gradient[2].

Having selected a specific plane, the next step is to determine the x and y dimensions of the pixels. This process, also known as spin warping, is achieved by multiplying the $m(x,y)$ signal by a special frequency weighting factor by means of phase encode and frequency encode gradients. By convention and without loss of generality, the frequency encode or the readout gradient, is applied along the x-axis before and during

the formation of the echo to modulate the frequency of the spins according to their position along the x -axis. In order to traverse the axis perpendicular to the readout axis, stepwise linear increments of the phase encode gradient are applied after the slice select and prior to frequency encode gradients. Phase and frequency encoding repeat as long as sufficient k -space data, corresponding to the required FOV is obtained (Table 2.1).

Although obtaining a sharp slice profile is the major challenge in multi-slice 2DFT MRI, it is easy to implement. Furthermore, because of the low bandwidth in the readout direction combined with multitude of phase encoding steps, spin-warp imaging results in good SNR that is proportional to $\sqrt{T_{read} N_{pe} N_{excitation}}$.

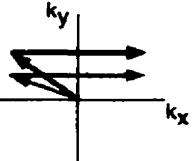
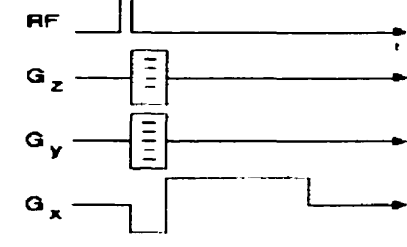
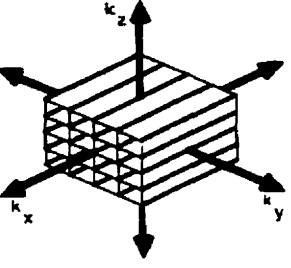
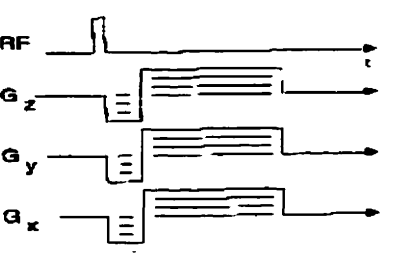
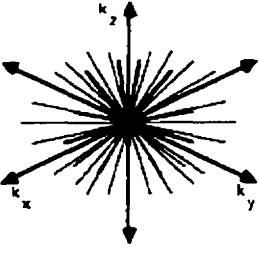
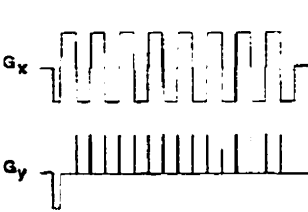
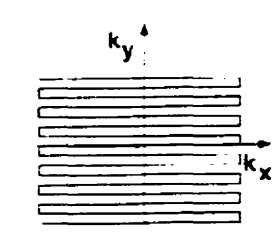
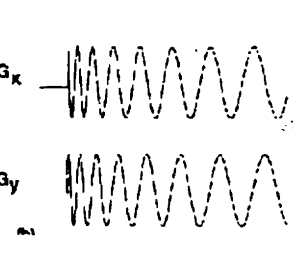
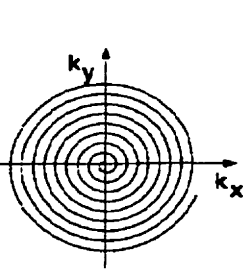
In the back-projection reconstruction method, a one-dimensional field gradient is applied at gradually increasing polar angles, and the NMR spectrum is recorded for each gradient. Projection reconstruction is based on the central slice theorem according to which, the 1-D Fourier transform of the projection of an image along an arbitrary axis corresponds to the data along the same axis of the 2D-Fourier transformation of that object. In terms of SNR, this technique is superior due to over sampling of the data at the center of k -space, where the frequencies of the gross features of the object are concentrated. However, the acquisition time in a 2D radial acquisition is π times longer than in 2D Cartesian sampling³. Furthermore, since back-projection reconstruction results in blurring, often a linear filter known as M-filter is used to enhance the edges of the image, thus the noise becomes colored and correlated with the large structures of the image. Higher sampling density at the origin also colors the noise.

Echo planar imaging (EPI), by benefiting from fast switching gradients, rapidly traverses an entire k -space trajectory after a single excitation. Since EPI is instrumental to fMRI, the in depth discussion of its properties are left to Chapter 3.

³ The Nyquist criterion in 2D sampling requires that $(N_x \cdot N_y) > 2(k_{max} \cdot FOV)$ while in radial sampling of the back-projection method $(N_\theta \cdot N_r) > 2\pi (k_{max} \cdot FOV)$

Similar to Cartesian EPI's, spiral trajectories provide high temporal resolution and low sensitivity to phase deviations due to motion. Spiral sequences make efficient use of the gradient hardware within the scanner and the smooth sinusoidal variation of the gradients helps in reducing eddy currents. Nevertheless, similarly to the back-projection method, k-space in spiral imaging is not uniformly sampled and if the readout time is long, relaxation effects can result in radial blurring of the reconstructed image. Furthermore, the coverage of the k-space is limited by the slew rate -- the time it takes a gradient to reach its highest amplitude-- that depends on the switching capability of the scanner gradients. The greatest drawback of spiral imaging rests in image reconstruction that requires determining weighting factors to compensate for the non-uniformity of data samples and in interpolation the spiral data set onto a Cartesian grid to make use of the FFT (fast Fourier transformation algorithm) for reconstructing the image.

Table 2.2 K-space trajectories, produced by different pulse sequences, result in different reconstruction methods[2].

Reconstruction Method	Pulse Sequence	Trajectory
2D Fourier Transform		
3D Fourier Transform		
3D Projection Reconstruction		
Echo Planar		
Spiral		

2.4 Image Resolution

In image acquisition the major parameters to be considered are: 1) image contrast, which is a function of proton density and relaxation times of different tissue types and 2) imaging speed, which is inversely related to SNR and image resolution.

The ability to resolve two features in an image is a function of many variables; T1, T2, signal-to-noise ratio, sampling rate, slice thickness, and image matrix size. The resolution of an image is determined by: 1) the choice of reconstruction technique and acquisition trajectory, 2) the receiver bandwidth and filtering of the raw data to ensure that the entire field of view (FOV) is spanned and 3) pixel size and sampling rate, governed by the Nyquist sampling criteria, according to which, the minimum sampling rate must be set to twice the highest frequency of the object, to prevent aliasing. Optimizing other imaging variables, as will be discussed shortly, involves improving some features at the expense of others.

The spatial resolution of an image depends on FOV and the matrix size that are determined by the strength of the gradient fields. Improving spatial resolution, involves increasing the bandwidth of the image that is defined as the frequency content of the image over the FOV. For instance, If N_x is the number of sample points in the frequency encode direction, and if the readout completes in t seconds, then the image bandwidth is $\pm 0.5 N_x / t$ Hz and the voxel bandwidth in phase encode direction is $1/t$ Hz. Although increasing the spatial resolution reduces the partial volume effects, it also reduces SNR that inversely relates to the squared root of the voxel bandwidth. One way of obtaining high resolution images without suffering loss of SNR is to increase the strength of the static field. A stronger field however, increases the sensitivity to certain artifacts, results in higher RF absorption at the surface while reducing the depth of RF penetration and increases the T1 relaxation time, and hence can reduce the contrast. Another way of enhancing the SNR is to reduce the receiver bandwidth. Since SNR is inversely proportional to the squared root of the receiver bandwidth, lowering it will not only

improve the SNR but will also filter electronic and other extraneous noise sources outside the frequency range of the signal. Decreasing the gradient amplitude, on the other hand, must be carefully designed to avoid significant chemical shift artifacts between water and fat. Therefore, as it can be seen, optimization in MRI is a dynamic interconnected problem that should be addressed depending on the specific imaging goals.

Chapter 3

FUNCTIONAL MAGNETIC RESONANCE IMAGING

3.1 Sources of Signal in fMRI

Functional magnetic resonance imaging (fMRI) is a non-invasive technique for estimating the increased neuronal activation of the brain of a subject responding to a stimulus or a specific task. Neuronal activity results in increased metabolic demand for glucose and oxygen that are delivered via cerebrovascular system. By measuring the changes in blood flow, volume and oxygenation in cortical areas of the brain, fMRI determines variations of magnetic resonance signal due to local metabolic or hemodynamic changes in the activated area.

3.1.1 Physiology of brain activation

Metabolically, the brain is one of the most active organs of the body. The average rate of oxygen consumption by entire brain is about 49 ml O₂ per minute, accounting for 20% of the resting body oxygen consumption[3]. At a cellular level, not only neurons, but also glial and vascular endothelial cells consume energy and play an active role in the flux of energy substrates into the brain. However, neurons contribute to almost 50% of cerebral cortical volume; therefore, brain energy metabolism predominantly reflects energy metabolism correlated with neuronal activity. The high energy demands of the

brain are almost exclusively met by oxidative metabolism of glucose; however, the local reservoir of oxygen in the brain is very minimal and since blood is the only carrier of oxygen into the brain tissue, the amount of oxygen consumption correlates with cerebral blood flow (CBF) that leads to increased local capillary density and hence, increased cerebral blood volume (CBV). It is worth mentioning here that there are two adjustment mechanisms in place for regulation of the metabolic demands of the brain. In long term adjustment, since local CBV is proportional to local CBF, the flow per capillary remains constant. Furthermore, since local metabolic rate of glucose ($ICMR_{GI}$) is directly related to local metabolic rate of oxygen ($ICMR_{O_2}$), oxygen extraction fraction between different regions is invariant hence the local ratio of oxyhemoglobin and deoxyhemoglobin is unchanged. In short term adjustment, i. e. during transient increase in neuronal activity, glucose consumption and consequently oxygen consumption is increased [4,6,9,10]. The fact that the density of capillaries, i.e CBV, cannot change as rapidly as the neuronal metabolism has opened the door to great discussions about how fractional changes in CMR_{O_2} and CBF are regulated.

Although it seems logical that an increase in local metabolism would necessitate a proportional increase in cerebral blood flow, in 1986, Fox *et al* reported a pronounced discrepancy between large stimulus induced increase in CBF and a relatively small CMR_{O_2} , as well as a large increase CMR_{GI} versus a much smaller oxygen consumption. They coined the term uncoupling to describe the dissimilar responses of CMR_{O_2} and CBF to physiological activation [4] and suggested that the CMR_{O_2} shortfalls were met through anaerobic glycolysis [5]. This uncoupling is differently explained by Buxton *et al.* [6] who suggest that disproportional CBF increase versus CMR_{O_2} compensates for the limited diffusibility of oxygen from blood to brain; increasing the velocity of perfusion above the speed of oxygen consumption results in increased intravascular/tissue diffusion gradient that facilitates the oxygen delivery.

Unlike Fox *et al*, several groups have now reported clear increases in oxidative glucose consumption [7] during the neuronal activation. Based on the coupling theory, in spite of disparity between the fractional changes in CBF and CMR_{O_2} , there is a distinct

relationship between their percentage changes. An important study by Hoge *et al* [8] have shown an invariant 2:1 coupling relationship between CBF and CMRO₂ during physiological stimulation. The significance of this finding rests in the simultaneous measurements of blood oxygenation level and perfusion that were interleaved during graded visual stimulation. They showed that fractional changes in oxygen consumption and blood flow did not depend on stimulus type, nor on the tissues with different levels of cytochrome oxidase. While these findings argued against Fox's anaerobic metabolism, they supported the role of diffusion-gradient limitations on oxygen delivery[9].

3.1.2 Susceptibility induced signal due to brain activation

In the previous section, we established that the neuronal activation is followed by increased metabolism that necessitates increased availability of oxygen at the site of activation. Almost 98% of the blood oxygen is transported by hemoglobin molecules inside the red blood cells[10]. Each hemoglobin consists of four protein subunits each centered around a heme group whose central iron atom binds weakly and reversibly with an oxygen molecule forming oxyhemoglobin. Since there are four iron atoms in hemoglobin, depending on partial pressure of oxygen in plasma, hemoglobin can bind to up to four oxygen atoms. During neuronal activation, the increased rate of oxygen consumption results in an increased diffusion gradient from blood cells to the tissue and the oxygen leaves the oxyhemoglobin and produces deoxyhemoglobin in which the heme iron has up to four of its six outer electrons unpaired [11]. While quantum stacking of electrons in an atom involves symmetric cancellation of spin moments for each pair of electrons, materials with an unpaired electron --known as paramagnetic material-- have a non-vanishing permanent spin moment that creates a non-zero dipole magnetic field, which aligns along an applied magnetic field and results in atomic magnetization. The magnetic moment of the electron is significantly higher than that of ¹H nucleus, resulting in a disruption in the coherence of ¹H spins precessing in the local magnetic field, leading to a local change in T_2^* time constant. Therefore, increased presence of deoxyhemoglobin produces local magnetic field inhomogeneity, giving rise to blood oxygen level dependent (BOLD) contrast mechanism in MRI where imaging timing parameters are set to maximize the T_2^* contrast[12].

3.1.3 Perfusion measurement

Aiming to detect the local changes in blood flow and/or oxygen consumption due to transient activation of the brain, fMRI gives rise to two classes of techniques: perfusion (CBF) measurements and susceptibility measurements. The latter method, known as BOLD was explained in the previous section. In this section the basics of perfusion technique are explained and the two methods are compared.

Arterial spin labeling (ASL), the basic method for the dynamic measurement of CBF, relies on measuring the flow of magnetically labeled water molecules in the tissue being imaged. The water molecules in the tissues are constantly exchanged with those in the blood flowing through capillaries. If the water content of a slab proximal to the imaging tissue is excited (by an RF pulse), its inflow perturbs the total magnetization present in that tissue and results in image intensity changes on the order of 1% [13]. Subtracting two images with different arterial magnetization is the basis of flow measurements techniques.

3.1.4 ASL versus BOLD

As mentioned earlier, BOLD signal arises from oxygen extraction in capillaries and deoxyhemoglobin flow into venous circulation which may be removed from the site of excitation. ASL signal, on the other hand, results from arterial inflow of tagged water molecules into the imaging slice. Although the exchange of water between capillary and tissue is bi-directional and fast, but since the vascular compartment is much smaller than tissue compartment and the time constant for outflow of tagged spins into the venous system is very slow (~1min) compared to the imaging speed (<2 sec), ASL is localized to arteries, capillaries and brain tissue [13].

Increase in the BOLD signal at 1.5 Tesla is often on the order of 1-4% of the raw data signal strength. Small subvoxel motion can easily change the raw signal by a few percent and thus drown the BOLD signal. Perfusion related increase in ASL is only 1% of the raw image intensity, therefore, it requires very high SNR to be practical. However,

since ASL relies on difference images whose signal intensity reflects the amount of perfusion occurring in the imaged slice, it scales with the raw image intensity, hence, a small increase in the raw signal intensity corresponds to 50-100% change in the intensity of the difference image, making it robust to small motion correlated signal variations. Nevertheless, the delay between activation and the time that the tagged spins reach the imaging slice makes BOLD measurements superior in terms of temporal resolution.

3.2 fMRI Imaging Sequences

Enhancing the temporal resolution of sampling the task-related cortical signal variations is at the core of functional brain imaging. However, in NMR imaging, the spatial resolution and the quality of the image are directly related to the imaging time. There are three general categories of functional image acquisition, EPI, spiral acquisition and FLASH (fast low angle shot). Either one of these acquisition methods can be based on GRE (gradient recalled echo) or SE (spin echo) sequences.

3.2.1 Echo Planar Imaging

Echo planar imaging (EPI) has been established as the most effective tool for fMRI, to date. EPI benefits from sophisticated hardware capabilities that enable rapid switching of the gradients used for the sampling of the k-space after a single excitation. EPI allows implementation of both spin-echo and gradient-echo, single or multi-slice imaging. The k-space trajectory of EPI is similar to a 2DFT acquisition; however, as depicted in Figure 3.1, while a conventional 2DFT sequence involves one RF excitation per line acquisition of the k-space, in EPI an entire k-space trajectory is acquired following a single excitation (i.e. in a single shot). The speed of EPI depends on the ability of readout gradients to switch to a high amplitude in a short time. Typically, the readout time for each echo (k-space line) is less than 1 ms which makes acquisition of an entire slice (e.g. 128x128 matrix) in almost 100 ms possible. The rise time of gradients is determined by di/dt , which, for a rise time of 300 μ s to 2.4 Gauss/cm gradients, requires a driving voltage of 300 V for maximum current of 250 A and gradient coil inductance of 1mH. This high power demand is often met by non-linear amplifiers operating on

capacitive or inductive drivers, known as gradient boosters (e.g. Siemens Vision 1.5T scanner, Siemens Medical, Erlangen, Germany)

As was mentioned earlier, the neuronal activation results in deoxyhemoglobin susceptibility effects [14] that translate into increased T_2^* relaxation. Although T_2^* relaxation time constitutes the main contrast mechanism in BOLD fMRI, it limits the period of data acquisition, affecting the actual resolution and the SNR of an EPI image. However, the short scan times help in minimizing the inter-view bulk motion as well as cardiac and respiratory related artifacts during acquisition of one view (a slice in 2D EPI). The EPI related difficulties in fMRI are discussed in 3.3.1

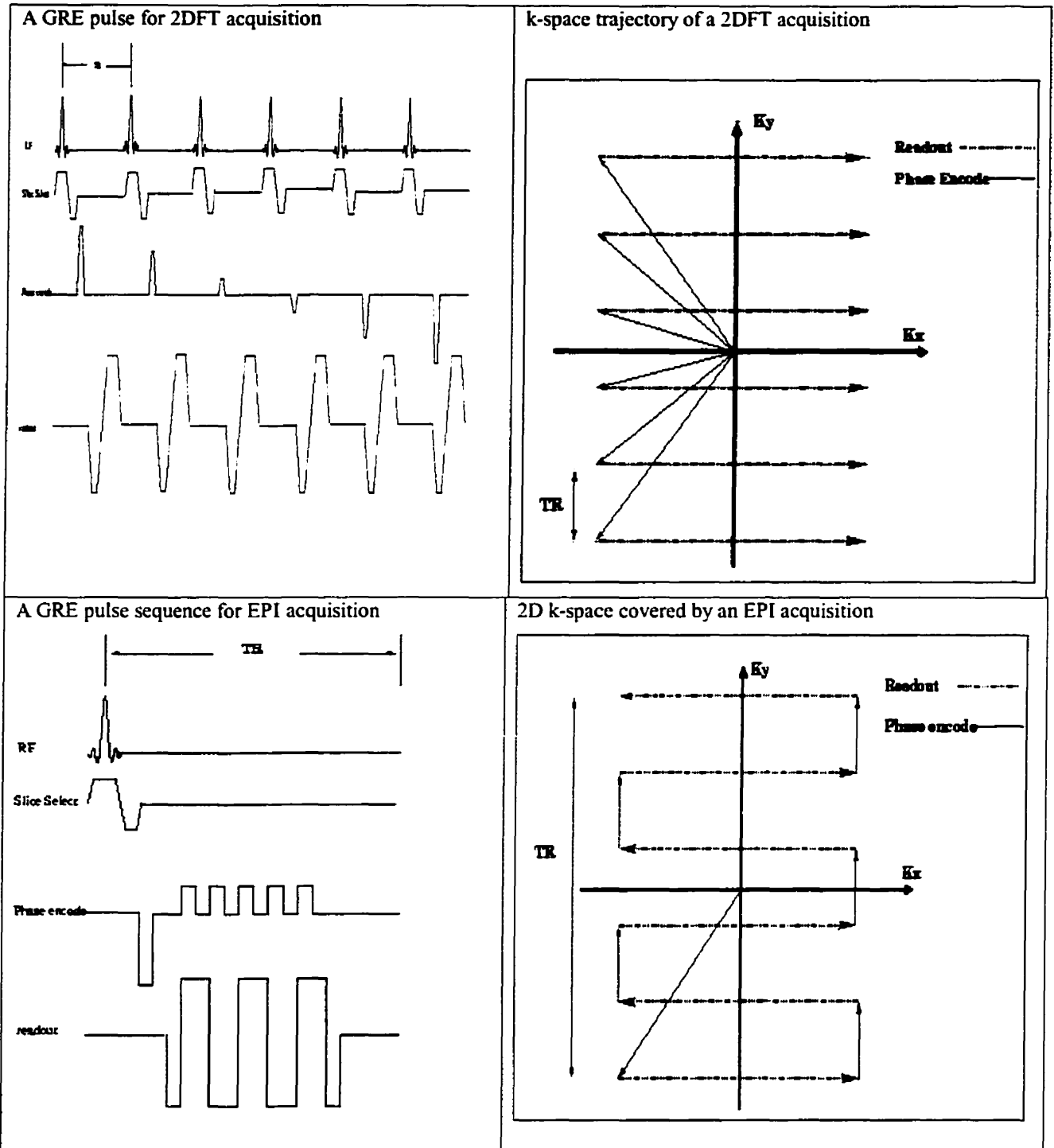


Figure 3-1: Differences between a standard 2DFT gradient echo and and EPI gradient echo acquisition. While in 2DFT each line is acquired after an RF excitation, the EPI acquisition completes after a single RF excitation. This is achieved by the ability of readout gradients to rapidly switch to a high power.

3.2.2 Fast Low Angle Shot (FLASH) Excitation

Complementary to EPI acquisition in fMRI, fast low angle shot gradient echo techniques provide fast scanning mechanisms, by shortening the repetition time compared to spin-spin (T_2) relaxation time, by means of small angle RF excitation that allows less longitudinal recovery time [12]. Reducing the TR to the order of, or less than T_2 , results in residual transverse magnetization whose state depends upon relaxation properties of the tissue, RF pulse energy and the applied gradients. A thorough description of the steady state behavior of echoes in FLASH is beyond the scope of this thesis, hence the discussion is limited to the timing and resolution of a typical FLASH acquisition compared to EPI.

Technically, FLASH resembles a conventional MRI sequence using multiple RF excitation, each producing one phase encoded MRI step per repetition interval. While a suitable TR for a 90° excitation may be as long as 6000 ms, it can be reduced to 50 ms or less for a 10° RF excitation. Compared to EPI, FLASH provides a better spatial resolution, however the imaging time is on the order of 2-6 seconds per image as opposed to ~ 100 ms in EPI acquisition, which makes FLASH much more sensitive to motion during acquisition [13].

3.2.3 GRE vs. SE

For a single slice GR echo image the signal for stationary spins within the slice is given by

$$S_{GE}(TR, TE) = \rho_H \exp\left(-\frac{TE}{T_2^*}\right) \sin(\alpha) \frac{1 - 2 \exp\left(-\frac{TR - TE/2}{T_1}\right)}{1 + \cos(\alpha) \exp\left(-\frac{TR}{T_1}\right)} \quad (3.1)$$

where ρ_H represents the proton density and α is the flip angle determined by RF excitation [15], as discussed in Chapter 2.

Similarly, the SE signal can be written as

$$S(TR, TE) = \rho_H \left[1 - 2 \exp\left(-\frac{TR - TE/2}{T_1}\right) + \exp\left(-\frac{TR}{T_1}\right) \right] \exp\left(-\frac{TE}{T_2}\right) \quad (3.2)$$

if $TR \gg TE$, the equation reduces to

$$S(TR, TE) = \rho_H \left[1 - 2 \exp\left(-\frac{TR}{T_1}\right) \right] \exp\left(-\frac{TE}{T_2}\right) \quad (3.3)$$

As can be seen in equation 3.3, T1 weighting is controlled by TR and T2 weighting is determined by TE.

Unlike the spin echo sequence, GRE does not refocus the phase accumulations due to static field inhomogeneity. This is reflected in the dependence of GRE signal on T_2^* , as opposed to dependence of SE on T_2 which is affected by the diffusion motion of spins. As discussed earlier, the fMRI experiments are designed to reflect the spin density and T_2^* relaxation times. In flow imaging, decreased TR of the GRE results in high intensity signal from the flow of unsaturated blood into the partially saturated imaging slice [16]. On the other hand, the refocusing pulse of SE sequence provides time-of-flight selection for spins that flow into the imaging slice between slice selection and 180° refocusing RF pulse, hence it suppresses the high velocity spins.

The susceptibility contrast of GRE and SE is a function of the size of the structure. Numerical simulation results [17, 18] and biophysical modeling [19] results have shown that unlike GRE, SE signal reduces with increase in the particle size. GRE is sensitive to inhomogeneities in larger structures (on the order of 20 μm) such as deoxyhemoglobin susceptibility effects in venules and veins. In addition to detecting venous blood signal, SE is sensitive to the local water diffusion gradient which is inversely related to the size of the structure. SE shows the greatest contrast for object on the order of 5-10 μm , such as capillaries [11].

3.3 Sources of Artifact in fMRI

3.3.1 EPI-related artifacts

The most desirable feature of EPI, its speed, is also the source of major artifacts. First of all, the signal to noise ratio (SNR) is highly reduced because of the large bandwidth resulting from the speed of the k-space trajectory. The large gradient fields that are turned on and off periodically also result in time-dependent eddy currents, which are problematic, over the period during which an entire k-space trajectory is sampled. Frequency shifts created by eddy currents, combined with the back and forth sampling of k-space creating phase discrepancies between odd and even lines of the data, result in a common artifact known as $N/2$ ghosting. In this artifact, a part of the image appears to be shifted by half the FOV. The $N/2$ ghost artifact can be prevented by calibration between signal acquisition and gradient activity or corrected for by acquiring non-phase encoded reference signals for calculation of phase drifts during the k-space readout.

In the phase encode direction, since the bandwidth is very low (30 Hz/pixel, 1.5 T), small frequency shifts due to non-homogeneous magnetization of the brain or chemical shift appear as significant spatial shifts (geometrical distortion) in the image. For example, in a 1.5 T system, the fat-water shift is about 220 Hz [13]. Compared to 30 Hz/pixel bandwidth of sampling in EPI's phase encode direction, the fat-water signals can be displaced by about 8 pixels.

3.2.2 Susceptibility-induced artifacts

Due to its non-homogeneous structure and non-isotropic geometry, reorientation of the head with respect to the magnetic field will change the magnetic field boundary conditions. Since different tissue types have different susceptibilities, the amplitude of the signal at the boundaries of tissues differs depending on the geometry and magnetic properties of the interface[20]. An approximate rotation of 5° in orientation of the head relative to B_0 field results in alteration of effective shim and residual field variations of up to 30 Hz [21].

Stimulus correlated motion, for example, results in amplitude changes in the base images that can appear as stimulus correlated false-activation. Hanjal et al [22] performed visual and motor tasks while retrospectively monitoring the subject's motion and obtained clear evidence of false activation where there was steep intensity changes on the source image, such as at the boundaries between brain, CSF and regions where there were inflow or susceptibility changes .

Respiration-related susceptibility artifacts can also contaminate the fMRI results by disturbing the B_0 field's homogeneity due to not only the movement of the chest, but also due to increased concentration of oxygen in the lung cavities [23] which can produce 2-3% signal variations in the head, the same order of magnitude as the activation signal[24]. Respiration can also cause rigid movement of the head and the brain tissue. Ryner et al [25] have shown wide spread signal changes within the brain, along the gyrus surfaces and at some edges of the brain, which they have attributed to susceptibility induced field variations due to brain and CSF contractions during the breathing cycle. The physical movement of the head due to breathing is confirmed by actual measurement of the head motion by infrared balloon sensors [26].

Chapter 4

THEORETICAL FORMULATION OF MOTION

The motion artifacts in MRI can result from rigid body displacements or nonlinear deformations of the structure being imaged. The problem addressed in this thesis is the rigid body movement of the object in the scanner that is a combination of rotational and translational displacements with respect to the iso-center of the magnet. As will be shown shortly, the effect of translational motion on the MRI signal is readily described by the Fourier shift theorem. The phase variations arising from rotation of the object about points other than the iso-center of the static magnetic field, however, cannot be as simply explained. In this chapter the mathematical expressions for both rigid body translation and rotation are derived and the effects of flow and physiological motion on the raw MRI signal are explained. Various techniques that detect and compensate for these motions are discussed in the next chapter.

4.1 Inter-View versus Intra-View Motion

The effects of motion depend on when during the acquisition it occurs. In terms of image acquisition, motion, regardless of its characteristics, can be categorized as: 1) inter-view motion and 2) intra-view motion [27]. The definition of view depends on the imaging sequence. A view is usually defined as the k-space data sampled following a single RF excitation. A view can be all the raw data for a single 2D slice, e. g. in EPI, or a single

line of Fourier data obtained during readout in a conventional spin warp sequence. Inter-view motion refers to displacements between the acquisition of individual views while intra-view effect refers to motion between excitation and readout or during the readout of the view. In other words, intra-view effects, e.g. blood flow[28] , are due to motion during echo time (TE) while inter-view motion refers to displacement of the object between TR's. In both inter- and intra-view motion, spin displacement alters the magnitude and shifts in the spatial frequency change the phase of successive views. These changes, as will be explained shortly, can be modeled as a complex function modulating the k-space [29] and can be used to invert the artifacts.

4.2 Effect of Displacement

This section formulates the effect of motion on a 2DFT, slice selective acquisition. Assume a 2D plane of excitation and define a reference view to be formed by the collective signal from each k-space data point as:

$$S(t) = \iint_{xy} m(x, y) e^{-i2\pi[k_x(t)x + k_y(t)y]} dx dy \quad (4.1)$$

If the object is moved by $(\Delta x, \Delta y)$ in the second view, then the signal would be:

$$S'(t) = \iint_{xy} m(x + \Delta x, y + \Delta y) e^{-i2\pi[k_x(t)(x + \Delta x) + k_y(t)(y + \Delta y)]} dx dy \quad (4.2)$$

or

$$\begin{aligned} S'(t) &= \iint_{xy} m(x', y') e^{-i2\pi[k_x(t)x + k_y(t)y]} e^{-i2\pi k_x(t)\Delta x} e^{-i2\pi k_y(t)\Delta y} dx dy \\ &= e^{-i2\pi(k_x(t)\Delta x + k_y(t)\Delta y)} \iint_{xy} m'(x, y) e^{-i2\pi[k_x(t)x + k_y(t)y]} dx dy \end{aligned} \quad (4.3)$$

where $x' = x + \Delta x$, $y' = y + \Delta y$ and $m'(x, y) = m(x', y')$.

In other words, in the Fourier domain

$$S(k_x, k_y, t) = S'(k_x, k_y, t) e^{i2\pi(k_x \Delta x + k_y \Delta y)} \quad (4.5)$$

which according to the shifting property of Fourier transform, can be expressed as

$$S(k_x, k_y, t) = S'(k_x - \Delta x, k_y - \Delta y, t) . \quad (4.6)$$

The above formula indicates that displacement in space domain translates to linear phase shift in frequency domain, hence the effects of motion can be removed by linear phase demodulation of the recorded signal (raw data), prior to reconstruction of image. The basic concept of extraction of phase discrepancies between a reference and a displaced view and demodulation of phase effects constitutes the core of the navigator-based, retrospective motion compensation techniques investigated in this thesis.

4.3 Effect of Rotation

Now assume a rotation of α° and a displacement of Δx and Δy . In this case the x and y coordinates will be

$$\begin{aligned} x &= x' \cos \alpha - y' \sin \alpha + \Delta x \\ y &= y' \cos \alpha - x' \sin \alpha + \Delta y \end{aligned} \quad (4.7)$$

hence

$$S'(t) = \iint_{xy} m'(x, y) e^{-i2\pi[(x' \cos \alpha - y' \sin \alpha + \Delta x)kx + (y' \cos \alpha - x' \sin \alpha + \Delta y)ky]} dx dy. \quad (4.8)$$

As can be seen in the above formula, calculation of the phase change in a single view Cartesian coordinate system would be cumbersome. Both formulation and detection of rotational motion are better expressed in a polar coordinate system. In other words, information about the rotation of the object around the center of Fourier space are inherently sampled over a circular trajectory. One difficulty associated with circular sampling rests in difficulty of reconstruction of an image from data points on a polar grid. Fast Fourier transformation (FFT) algorithms provide an efficient and easy reconstruction mechanism. Regardless of the sampling trajectory, image reconstruction often involves interpolation of the sampled data onto a Cartesian grid. The difficulty involved in the optimization of interpolation scheme in addition to hardware requirements, contributes to the relatively low popularity of imaging techniques such as spiral acquisition. A simple way of estimating the rotation between acquisition of each view would be to acquire fast echoes over simple orbital trajectories that sample only a small fraction of the FOV and are interleaved with the imaging echoes. These echoes, commonly known as orbital

navigators, are used for extraction of rotational and translational components of the motion and are thoroughly explained in Chapter 6.

4.4 Effects of Velocity and Acceleration

The analysis of the effect of velocity and acceleration of a moving object is particularly important when there is significant motion between excitation and the end of readout. Recall that the phase of the NMR signal coming from the bulk magnetization is

$$\phi = \gamma \int_0^t G(\vec{r}, t) \bullet \vec{r}(t) dt \quad (4.9)$$

where $\vec{r}(t)$ denotes the position vector in time. Expanding $\vec{r}(t)$ as a Taylor series:

$$\vec{r}(t) = \vec{r}_0 + \vec{r}' \frac{t}{1!} + \vec{r}'' \frac{t^2}{2!} + \vec{r}''' \frac{t^3}{3!} + \dots \quad (4.10)$$

where \vec{r}_0 denotes the initial position, \vec{r}' velocity, \vec{r}'' acceleration and \vec{r}''' pulsatility.

In general, moving spins with different velocities have different phases that lead to signal loss – intra-voxel dephasing – and ghosting by phase errors between views. To compensate for these effects, the phase difference due to velocity and acceleration may be nulled. The velocity effects are often associated with flow motion in blood vessels or translational tissue motion, e.g. chest movements during breathing. Gradient moment nulling, discussed in the following chapter, is often used to minimize such artifacts.

4.5 Effects of Flow

Flow can be modeled into three types: plug flow, laminar flow and turbulent flow [12]. In plug flow, all the spins in the vessel have the same velocity while in laminar flow, the velocity of spins is a quadratic variable of their radial position in the vessel. At higher velocities, the laminar flow changes to turbulent where in addition to a bulk flow component, there is a component of the fluid whose velocity fluctuates. The division between laminar and turbulent flow is set by the Reynolds number, which is a function of fluid density, velocity, tube diameter and the viscosity of the fluid. Assuming a straight circular tube of radius a and mean velocity \bar{v} , the plug flow velocity distribution is:

$$v(r) = \bar{v}, \quad 0 \leq r \leq a$$

and the velocity of laminar flow is parabolically distributed in the tube as:

$$v(r) = 2\bar{v}\left[1 - \left(\frac{r^2}{a^2}\right)\right], \quad 0 \leq r \leq a.$$

Although there are many causes for flow artifacts in 2DFT images, the mechanisms are either view-to-view fluctuations in the effective spin density (magnitude) and/or in the phase of the net voxel magnetization. The net voxel magnetization can vary due to 1) inflow of unsaturated spins into the section, 2) outflow of saturated spins out of the section and 3) variations in the amount of echo attenuation due to intravoxel phase dispersion which is due to the presence of different velocities within a single voxel [30].

A complete discussion of flow effects in MRI is beyond the scope of this chapter. In general, these effects depend not only on velocity and volume of the flow, but they also vary with the direction of the sampling in the k-space trajectory. While plug flow in readout direction causes blurring and phase degradation, it leads to image degradation and signal loss in slice-select direction and to misregistration artifacts in the phase encode direction.

4.6 Physiological Motion

Periodic physiological functions such as respiration and cardiac cycle are considered to be prominent sources of artifacts both in anatomical and functional MRI. While in anatomical imaging the periodic effects of respiratory motion cause ghosting[31], in functional MRI they may change the phase and magnitude of the signal throughout the cardiac cycle [15,16]. The ghosting due to periodic motion is a result of periodic phase modulation of the raw data, which often affects the raw data in the phase encode direction. The number of ghosts, n , is a function of T/TR , where T is the period of motion and TR is the time interval between excitations. The ghosts (i.e. erroneous images of periodically moving compartments) are separated by a distance equal to the extent of the FOV in phase encode direction divided by n .

For a typical fMRI experiment, an EPI acquisition with short repetition time on, the order of 100 ms, compared to average cardiac and respiratory cycles of 1s and 3-5 s, respectively, is relatively immune to these physiological artifacts. Nevertheless, respiratory and cardiac pulsation induce fluctuations in blood flow to the central nervous system and in the cerebrospinal fluid (CSF) that may introduce colored noise artifacts, especially if correlated with the stimulus presentation cycle. These fluctuations have two components. A relatively low amplitude and short duration pulsation, which is ascribed to arterial pressure change and corresponds to cardiac pulsation, plus a relatively high amplitude constant displacement of longer duration, which is ascribed to venous pressure changes and corresponds to respiratory cycle[13]. Furthermore, as blood flow in the cranial cavity increases, the brain expands and CSF and brain tissue moves in the direction of least resistant. The velocity of physiological brain motion is less than 1mm/s. So, unless TE is long, this type of motion does not result in significant phase change. In contrast, the high velocity flow, which causes arterial pulsation, leads to both phase and magnitude alteration in k-space that translate into intensity fluctuations, appearing as bands across the image[34]. In fMRI, a double problem may occur; the signal loss can erroneously mask the activation and ghosts of vessels, which appear with higher intensity, can be interpreted as activation [35].

It has also been shown[24] that the expansion and contraction of the lungs and heart in the chest cavity result in susceptibility induced magnetic field shifts that translate to resonant frequency (and consequently phase) shifts that produce artifacts on the order of 2-3% --approximately the same magnitude as activation related BOLD signals. Furthermore, respiration causes a small periodic phase variation of approximately 0.25 Hz [33].

Eye movement is another source of physiological motion in fMRI. Involuntary eye movements during resting conditions can cause substantial signal fluctuations in the phase-encoding direction even for a fast echo-planar imaging (EPI) sequence[36]. If the phase encode direction corresponds to the anterior-posterior, the eye motion induced ghosts can appear on the brain. One way of dealing with this problem is to choose the

phase encode direction more carefully so the ghosts appear outside the brain region or to use a slab saturation at the position of the eyes to suppress the eye signals[36].

Chapter 5

MOTION COMPENSATION TECHNIQUES

5.1 Motion Effect Reduction

Techniques that reduce the effect of motion can be divided into two categories – which are often combined; those that modify the acquisition sequence in order to minimize the effect of motion on the collected raw data and those that utilize data analysis and signal processing techniques to measure the motion, model it and invert its effects as much as possible. Techniques such as gradient moment nulling [30], phase encoded reordering [37,35], triggering [33, 38, 39], modified k-space trajectories[40], and fast acquisition [23-26] belong to the first group where the aim is to minimize the effect of motion induced signals during acquisition. In the second category, techniques such as post processing, averaging [43, 44], adaptive correction techniques [27, 46-48], and filtering [44, 49], to name a few, emphasize elimination of residual motion related artifacts that have not been prevented during acquisition. In this chapter the most relevant techniques are discussed in more details. It is important to note that this literature survey does not include the mathematical algorithms dealing with inter-view motion correction during image registration and has rather focused on the MR sequences and signal processing techniques that address both inter- and intra-view motion problem.

5.1.1 Gradient moment nulling

This technique is an important compensatory mechanism for intra-view artifacts due to acceleration and velocity related phase dispersions resulting from motion between excitation and detection of the NMR signal. In 1987, Pattany *et al*[50] developed a Motion Artifact Suppression Technique (MAST) that used a series of gradient echoes that were computed to cancel velocity, acceleration and pulsatility (or jerk) components of involuntary motion in MRI. This technique, which later evolved to be generally known gradient moment nulling (GMN), is based on the expansion of motion as a Taylor series, estimating the phase accumulation due to velocity, acceleration and pulsatility, and finally, canceling the accumulated phase by setting the first, second or higher moments of the gradient waveforms --corresponding to velocity, acceleration and jerk, respectively,-- to zero.

If the motion is not too complex, the trajectory $x(t)$ can be well approximated with a few terms of the Taylor series expansion:

$$x(t) = x_0 + v_0 t + \frac{1}{2} a_0 t^2 + \dots \quad (5.1)$$

where x_0 is the displacement of the spins with respect to the center of the k-space, v_0 is the velocity of moving spins and a_0 is the acceleration at $t=0$. The accumulated phase at TE, is therefore:

$$\Delta\phi = \gamma \left[x_0 \int_0^{TE} G(t) dt + V_0 \int_0^{TE} t G(t) dt + \frac{1}{2} a_0 \int_0^{TE} t^2 G(t) dt + \dots \right] \quad (5.2)$$

where the second and third terms represent the first and second moments of the gradient vector respectively. Motion induced phase shifts can be reduced by designing gradient pulses such that a certain number of their moments vanish (Figure 5.1).

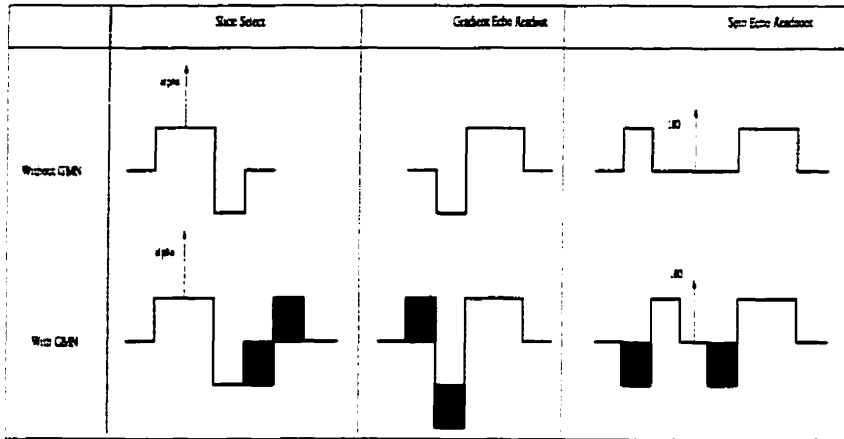


Figure 5.1 Modified gradient echoes with first order gradient moment nulling.

Gradient moment nulling does not prolong acquisition time significantly, nor does it require patient preparation or post processing of the data. GMN is widely used to compensate for intra-view motion artifacts in gradient and spin-echo sequences for vascular, head and spine, thorax and abdominal imaging [30,51]. In addition to motion compensation, GMN finds application in MRA, flow quantification, or even examination of sequence-dependent motion effects under a variety of conditions[35, 36].

5.1.2 Phase-encode ordering

The periodic nature of cardiac and respiratory motion translates into ghosting effects in the images. Phase-encode ordering techniques aim to destroy the coherence of the motion by altering the order of data acquisition depending on the position of the subject. In a normal phase encoding scheme, the gradient table contains values starting from a negative maximum to a positive maximum by steps of ΔG_y and the data is acquired monotonically from $-k_{y \max}$ to $k_{y \max}$. In ordered phase encoding, information about the pattern of motion is obtained from special transducers, such as chest straps, attached to the patient prior to each RF excitation and the particular value for k_y is chosen based on the point in the period of motion. Phase encode reordering is based on the assumption that inter-view rigid body translations within an imaging volume only affects the phase of k space and that this effect can be modeled through a complex modulation function

$$M(k_y) = e^{-i2\pi \frac{\Delta y(k_y)}{N_y} k_y} \quad (5.1)$$

where $\Delta y(k_y)$ represents the number of translation pixels and N_y is the number of pixels in the phase encode direction. The artifactual k-space data would then relate to the stationary data as

$$F_{\text{artifact}}(k_x, k_y) = F_{\text{stationary}}(k_x, k_y)M(k_y) - F_{\text{stationary}}(k_x, k_y) \quad (5.2)$$

or

$$F_{\text{artifact}}(k_x, k_y) = F_{\text{stationary}}(k_x, k_y)(M(k_y) - 1) \quad (5.3)$$

The goal in phase encoded reordering is to chose k_y such that the modulus of the M function becomes one. Reordered phase encoding can be implemented in any conventional multi-view sequence without prolonging the imaging time.

Some of the common methods of phase reordering such as ROPE (Respiratory Ordered Phase Encoding) [54], COPE (Centrally Ordered Phase Encoding) [44] and POPE (Projection Ordered Phase Encoding) [55] have proven useful in elimination of respiratory ghosting effects. Phase encode ordering is also implemented to address the sensitivity to motion in 3D MRI [37]. It must be noted however, that although this method reduces respiratory ghosts successfully, it does not reduce blurring, nor ghosting from other movements.

5.1.3 Modified acquisition techniques

Glover and Pauly [56] have shown that projection reconstruction (PR) techniques are intrinsically advantageous over spin warp methods in reducing motion effects. In the projection reconstruction technique, oversampling of the low spatial frequency components provides intrinsic averaging of gross features of the subject[56]. Furthermore, while motion-generated inconsistencies in spin warp methods appear as ghost artifacts in phase encode direction , in PR the ghosts appear as streaks emanating perpendicularly from moving objects, therefore artifact energy is spread in all directions, often into the outer boundaries of the anatomical image (Figure 5.2).

Kruger et al [57] have proposed an orthogonal correlation algorithm for reducing the effects of motion induced ghost artifacts. In their method two data sets are obtained by swapping the phase and the frequency axes. While the image content of the data correlates, the ghosts do not, therefore the artifacts in the resultant image are greatly reduced. This method is applicable to any 2DFT acquisition technique, and is easily implemented, however, it doubles the acquisition time.

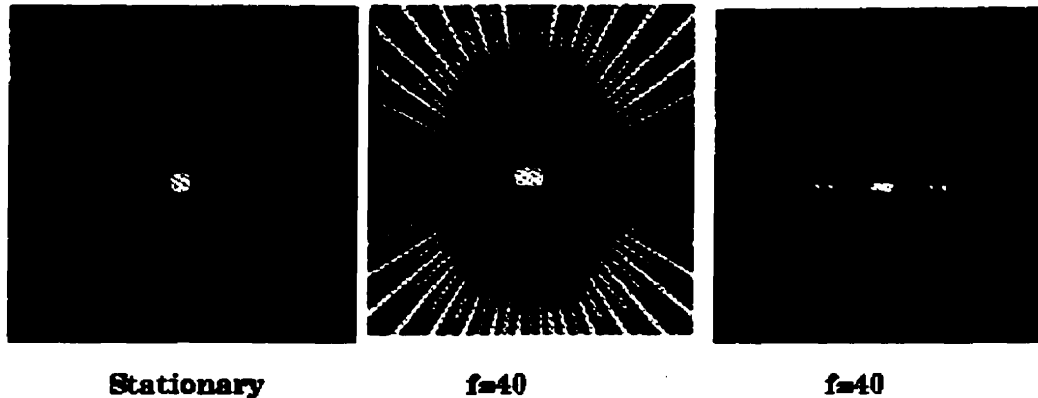


Figure 5.2: A point object has been sinusoidally moved in the phase encode direction about its origin. Ghosts in the projection reconstruction method appear as streaks removed from the center of the FOV as opposed to the ghosts in the phase warping acquisition, which are repeated across the FOV along the direction of movement[56].

5.2 Motion Prevention Techniques

The amplitude of the motion modulation function is directly related to the extent of the displacement of the object, measured in number of pixels rather than in centimeters [58]. The easiest way of reducing motion artifacts in an MR image is to restrain motion either in image space by minimizing the physical movement of the subject, or in data space by avoiding acquisition during the motion or rejecting the motion contaminated acquisitions.

5.2.1 Physical restraining

Physical restraining, depending on the anatomic site, and the cooperation of the patient are the most trivial, yet effective ways of limiting the extent of patient movement. Strapping chest devices[45], bite bars [8] and vacuum pillows[26], are used to minimize the effects of breathing or gross body movements. Patient cooperation is a determining

factor in the usefulness of such devices. Nevertheless, physical restraining is not a viable option in imaging organs with internal movements such as dilation of heart and brain. In such cases gating and triggering provide the means of minimizing the effect of their displacement.

5.2.2 Acquisition control

Suppressing the acquisition of erroneous data requires a priori knowledge or monitoring of the spatial extent or the temporal frequency of motion. This information is used to modify the acquisition sequence in order to avoid artifactual measurements.

Gating techniques are based on defining a displacement threshold. If the anatomical object moves beyond the threshold during an acquisition, the data is disposed of and the acquisition is repeated [59]. While gating is basically a motion rejection technique, triggering is a preventative mechanism associated with periodic motion. By monitoring physiological activity, for instance the electrical signals obtained by electrocardiograms (ECG), triggering allows the repetition time (TR) to vary such that all data acquisition occurs at the same phase of motion, hence reducing the blurring and the ghosts [60,42], which makes it a standard remedy for respiratory and cardiovascular related artifacts.

5.3 Motion Detection and Correction

Identifying a correct model of motion is the first step in post-processing correction of motion related degradations. The basic models of motion are translational, rotational and dilational movements. Parameters of a motion model can be determined from either the corrupted data or during acquisition by means of navigator echoes, laser detectors or chest straps.

5.3.1 Motion estimation from data and post processing

As explained in Chapter 4, inter-view motion, such as motion between phase encoding steps, introduces a phase factor that depends on the object's displacement from the reference point. Korin et al [61] proposed a compensation scheme based on

estimation of motion from phase differences between views of an object moving within a slice with a known linear velocity. The robustness of their technique, considering the fact that in clinical cases the time course of the motion is nonlinear, relies on a piecewise linear estimation of the velocity.

Phase retrieval by post-processing analysis of the reconstructed image is probably the simplest method of correcting translation-related artifacts. In this method, the image data is Fourier transformed and the phase portion of the transformed data is used to determine shifts. Hedley *et al* [62] proposed an improved iterative algorithm that removed the noise outside the region of interest before Fourier transformation of the image and then obtained the linear phase shifts by the method of least squares. This method was further improved by Zoroofi *et al* [63] who proposed to remove the readout translational motion by spectrum shift method prior to retrieval of phase shifts in readout and phase encode directions. The spectrum shift method is based on edge detection. To minimize the effects of noise on the sharpness of the edges, two high intensity gray level markers were positioned on each side of the object.

Lauzon and Rutt[64] proposed a hybrid method in which they combine a moderate speed high contrast (MOHICON) and a fast low contrast (FALCON) acquisition technique to obtain a formalized k-space for determining generalized motion modulation, (be it translational, rotational or dilational) based on the Fourier projection slice theorem [64]

Entropy focus criteria have also been used to reduce image degradation due to noise [66] and motion [67]. The entropy focus criterion, E , is defined as

$$E = -\sum_{j=1}^S \frac{B_j}{B_{\max}} \ln \left[\frac{B_j}{B_{\max}} \right], \quad (5.4)$$

where S is the number of image pixels and B is the modulus of a pixel (pixel intensity). Entropy minimization, as a focus criterion, favors high contrast and is used to remove motion induced ghosts from low intensity regions of the image. Entropy maximization prevents low intensity data from being obscured by noise. In [68], Atkinson *et al* have

modeled motion as a series of time dependent displacements, discretized into nodes, with the timing of each node corresponding to a line acquisition. The motion is then approximated in a piecewise linear fashion from these time trajectories and the entropy focus criteria is used to optimize the best motion parameter that produces the highest quality image. This method is also expanded to correct for rotational motion.

In addition to entropy focus criterion, image quality can be measured by metrics such as properties of image histogram[69], image gradients[70], auto-correlation and standard deviation[71] as auto-correction metrics.

In real time imaging, often the motion contaminated acquisitions are discarded and the acquisition process is iterated. The diminishing variance algorithm (DVA) makes use of a preliminary data set as reference and measures the displacement of the object for each frame of the data and adds them to a histogram of shifts[72]. The frame that needs to be re-acquired is then found from determining the frame with largest weighted distance from the computed mode, mean, or some other centering measurement of the histogram.

EMOTIONAL FIRE (Evaluation of MOTION and reALignment for Functional Imaging in REal time), introduced by Mathiak and Posse [73] performs a rigid body motion correction of a complete multi-slice EPI data set within a single TR. Optimization criteria of this algorithm is based on minimization of difference between the reference and the shifted image in a quadratic sense. Estimator gradients in translational direction are calculated by derivative of intensity $dS/dx = 1/2(S(x+l,y,z) - S(x-l,y,z))$. The rotational components are obtained by $dS/d\theta_z = x.dS/dy - y.dS/dx$ and dilation gradients are expressed as $dS/dCx=x.dS/dx$, analogously for all directions. Correction for the estimated movement is performed by reslicing with linear interpolation on a shifted grid. This algorithm offers real-time motion correction of multi-slice fMRI with a temporal resolution of 1-2 sec and improved activation maps are reported.

5.3.2 Motion detection by navigator echoes

The concept of navigator echoes was first introduced by Ehman and Flemler [47] as a means of quantitative motion detection and correction. Using mathematical techniques, they adaptively corrected the raw data for global view-to-view motion or bulk phase shifts due to intra-view tissue motion. To measure these effects, they proposed the use of spatially encoded echoes to track position and phase of the object within the field of view. Comparison between the successive non phase-encoded navigators yielded a measure of phase variations in the direction of displacement. Phase demodulation of the raw data in the direction of the motion corrected the image displacements. This method improved the results in case of 2D in plane motion, but it did not compensate for the cases that the structures were moving in and out of the plane of excitation. Korin *et al* 1990 [46] proposed a correction technique for 3D imaging that enabled measuring the motion in a plane perpendicular to the plane of acquisition. Their method acquired sagittal navigators in combination with axial imaging slices.

The methods compensating for in plane rotation of the imaged object were first introduced by Korin *et al* [74]. Due to the elliptical shape of the head, the linear navigators previously used did not change sufficiently in the presence of rotation in order to provide a reliable measure of the angular movement. Therefore, they attached tunable markers to the head. The markers were chosen to have signal intensities higher than the head in the phase encode direction such that the profile of the marker appears distinguished on the linear navigator echo. Shifts of frequency peaks, corresponding to the markers on the spectral profile of the navigator data were used to determine rotation. The markers were formed from concentric circles so that their spatial frequency did not change with head rotation and remained in the same profile as the navigator's.

An alternative to the fiducial marker method was introduced in 1995 by Fu *et al* [75]. In this method the navigator echoes were formed by sinusoidal gradients and were thus acquired on a circular k-space trajectory, known as orbital navigators, centered at the origin of the k-space. The grounds for using orbital navigators for detection of rotation lies with the Fourier rotation theorem: rotation of the object about the origin by an angle

α will produce an equal rotation of its Fourier transform. If the center of rotation is away from the origin, then according to Fourier shift theorem, it produces a phase shift proportional to the distance of center of actual rotation from the origin of k-space, as discussed in the previous chapter. Therefore, information about the rotation of the signal are readily encoded in the amplitude of the navigator echoes while the translations are encoded in the phase variations of the navigator signal. Recently, Welch et al [76] have shown the feasibility of 3D rigid body motion detection via spherical navigator echoes. A spherical surface is sampled uniformly so that every sample point is equally sensitive to rotation about or translation along any axis. The ability to capture all six degrees of freedom in a single 13 msec TE of the spherical navigator makes it attractive to fMRI and cardiac imaging.

The navigator echo motion correction scheme has been proven to be particularly reliable in the fMRI and diffusion weighted imaging (DWI).

5.3.2.1 Diffusion weighted imaging with navigator echoes

Overcoming the effects of macroscopic motion, while retaining the sensitivity to microscopic diffusion of water molecules is a major technical difficulty in DWI. The large gradients needed in DW sequences have very large moments and are thus extremely sensitive to the slightest motion that results in a large phase dispersion, masking the small amplitude variations due to the diffusion gradients. Navigator techniques were first used in DWI by Ordidge [77] whose technique differed from the original navigators by an extra spin echo; the navigator echo, without being phase encoded, was followed by the phase encoded image echo. Anderson and Gore [78] have used navigators with diffusion gradients in the phase encode direction to obtain information about rotation around the slice select axis. Since diffusion gradients are large, the phase error along a diffusion gradient echo is dominant. They have formulated the phase error due to rotation as:

$$d\hat{\phi}_{rot} = \gamma \int \bar{G}(t) \times \bar{\theta}(t) dt \quad (5.5)$$

in other words,

$$d\phi_x = \gamma \int [G_y(t)\theta_z(t) - G_z(t)\theta_y(t)] dt \quad (5.6)$$

$$d\phi_y = \gamma \int [G_z(t)\theta_x(t) - G_x(t)\theta_z(t)]dt$$

$$d\phi_z = \gamma \int [G_x(t)\theta_y(t) - G_y(t)\theta_x(t)]dt$$

where $\bar{\theta}(t)$ is the rotation vector. As can be seen from the formula, phase error due to rotation in any given direction can be isolated if there is no rotation in the other two directions or if the gradient in that direction is significantly larger than the gradients in the other two directions. While navigator measurement serves in finding the zero order phase error, the linear phase increase along the diffusion gradient determines the first order phase error.

Crespigny *et al* [79] showed that the SNR of DWI can be improved by switching the position of navigator and image echoes. Furthermore, the robustness of the navigator echo technique can be improved by performing the phase correction step in frequency domain. Ulug *et al* [80] measured a reference phase map and phase demodulated the raw image data to match the phase profile of this reference map in order to correct the motion related phase variations.

DW navigated techniques can also be extended to include two navigator echoes in read out and in phase encode direction in order to account for the rotational motion of the head whether the diffusion sensitizing gradients are along readout or phase encode direction [81]. The spiral-navigated [82] interleaved EPI have been proven to be time efficient and motion robust means for DWI of acute stroke.[83]. Due to their superior image quality, the multiple echo acquisition techniques (e.g. fast spin echo, FSE) are preferred over single shot EPI methods. Mori *et al* [84] have proposed a novel twin echo navigator method in order to monitor inter-echo and intra-echo train phase errors in FSE type sequences. Usually, incorporating the navigator echoes into fast imaging techniques such as FLASH requires modification to the echo train and hence results in loss of sensitivity. Nevertheless, Norris and Driesel[85] have performed navigator based real-time motion correction along with RARE (rapid imaging with relaxation enhancement) DWI, whereby the navigator correction is performed online, in the intervals between a DW preparation and subsequent imaging sequence. The real-time mechanism allows for

correcting the zeroth order phase errors by pulsing the B_0 -coil of the system. The first order phase shifts, induced by translation of spins, are compensated for by adjusting the gradients just prior to acquisition of data.

5.3.2.2 fMRI with navigator echoes

Physiological motion, such as cardiac pulsation and respiration, discussed in Chapter 4, leads to signal fluctuations in fMRI which can result in false activation peaks. Due to the time constraints of fMRI acquisitions, the conventional full spin-echo navigator gradient methods are not optimal. Hu *et al*[86] tested the effects of respiration on the phase of a navigator gradient-echo. The navigator echo, which was acquired in the readout direction of a FLASH sequence right after the small angle excitation, preceded the image echo.

Real-time adaptive motion correction in fMRI, first proposed by Lee *et al* [87], provides a means of prospectively correcting the image by detecting the bulk head motions and repeating the acquisition after having adjusted the gradients for the subsequent EPI acquisitions. Using Orbital navigators, this prospective real-time correction method can be used to correct for both inter-image and intra-image, in-plane and through plane multi-axial motion [69, 70].

In addition to DWI and fMRI, the success of the navigator echo technique has been proven in MRA [71, 72], brain-motion studies [73, 74], stroke imaging [94], respiratory motion compensation [95], heart motion [96] as well as in quantification of low velocity motion [97], that establish this method as a flexible and promising tool in general motion compensation.

Chapter 6

3D ORBITAL NAVIGATORS:

Design and Implementation

6.1 Introduction

Techniques of dealing with motion in NMR imaging were described in Chapter 4. Of all those, the features that make orbital navigators most suitable for fMRI are: its speed of formation of orbital echoes, which are simultaneously acquired with great resolution, and the approximately uniform SNR over data points. Most importantly, it is the abundance of navigator data points relative to time and k-space coverage that allows accurate estimation of the parameters of the complex motion.

The primary purpose of this thesis is to provide a means for correction of view-to-view in-plane bulk head movements in time series images obtained from a single shot EPI (ssEPI) acquisition. To achieve this, three orthogonal orbital navigators were added to a BOLD-EPI measurement sequence in order to yield information on the nature and magnitude of in- and through-plane movements, that potentially degrade activation maps.

6.2 Pulse Sequence Design

The navigator pulse sequence was adapted to a gradient echo, BOLD measurement, single shot EPI sequence with a 90° flip angle RF excitation, 64x64 pixels and TR= 100 ms (per slice). The EPI sequence is equipped with a fat suppression based on spectral pre-

saturation. A non phase-encoded measurement of the central readout axis in forward and backward directions provides a calibration measure to extract the phase offset inherent to EPI acquisition of odd and even lines. This data is used during reconstruction to correct for $N/2$ ghost artifacts.

The acquisition parameters of the orbital navigators include, the RF excitation pulse, the radius of the orbital trajectory, which is determined by the gradient power and the duration of the gradient pulse, and the TR of the navigator acquisition. The objectives in choosing the parameters of the navigator acquisition are: 1) high SNR, 2) adequately high angular resolution and 3) speed, to minimize the chances of intra-navigator motion, as well as motion between the acquisition of the navigators and the image frame.

The first criterion in our implementation of the orbital navigators was to minimize the duration of the navigator acquisition so that the EPI repetition time TR is not significantly lengthened. The speed of creating the orbital trajectories is limited by the minimum gradient raster time of 10 microseconds, which is also the time duration associated with each amplitude point of a gradient pulse waveform (1.5T Siemens Vision system, Siemens, Erlangen, Germany). Each circular trajectory can be smoothly generated by 128 data points, i.e. during 1280 micro seconds, however, additional gradients are needed to center the trajectories about the origin of the k-space in the appropriate planes. The gradient waveforms, generated with Matlab, (Figure 6.1(a)) correspond to co-centered orthogonal orbital trajectories that are at the same radial distance from the origin of the k-space. The readout of data, however, does not cover the entire trajectories formed, but only a fraction of it that corresponds to the orbital navigators (Figure 6.1(a,b)). The process of executing the complete orbital trajectory is 11.64 ms but the total navigator readout time is 3840 microseconds (i.e. 3 x 1280 microseconds).

The gradients designed above trace the trajectory at a radial distance equal to :

$$k_r = \frac{\gamma}{2\pi} \int_0^{T/4} (\sin(2\pi/T) + \cos(2\pi/T)) dt, \text{ where } T = 1280 \text{ microseconds.}$$

The nominal k_r , generated by the external gradient waveforms of peak amplitude 1mT/m is 8.51 m^{-1} and it can be scaled up or down proportionally to the field strength of the gradients. The important factors in choosing the radius of the orbital navigators are the SNR and the structure of the magnitude of the navigator data that allows resolving the small shifts due to rotation in the magnitude data. While a smaller radius provides a better SNR, the finer detail of the object corresponds to higher frequencies, farther from the center of k-space. For a given radius in k-space, one way of increasing the SNR is to increase the power of the excitation RF pulse. Recall that the main criterion in the pulse sequence design was to minimize the time of the formation and acquisition of the navigators, therefore, a small angle rectangular RF pulse was chosen to non-selectively excite the spins of the objects. The RF power must be high enough for the FID signal of the last navigator to be sufficiently high, yet is must not be too high so as to leave traces in the magnetization history of the main EPI sequence. Optimization tests (see Table 6.1 and Figure 6.2) indicated that $k_r = 22.139 \text{ 1/m}$ ($\sim 8 / \text{FOV}$) and a rectangular RF pulse with 20° flip angle provides a good compromise between the SNR and the spatial resolution of the object.

As illustrated in Figure 6.3, in every slice, following fat saturation (not shown in the Figure), a rectangular pulse non-selectively excites the spins and the navigator echoes follow immediately. Care is taken to rewind the phase of the gradient echoes to prevent a shift in the center of the k-space for the following phase offset and EPI measurements.

Table 6.1: SNR for various radii of the orbital navigators and different RF flip angles

α \backslash Kr	5.1 1/m	13.62	22.126	30.636
10	89.7	76.5	69.4	32.7
15	117.0	102.8	61.82	46.8
20	125.147	108.68	76.62	62.02
25	111.3	88.67	80.54	55.47
30	105.0	108.1	81.96	64.181

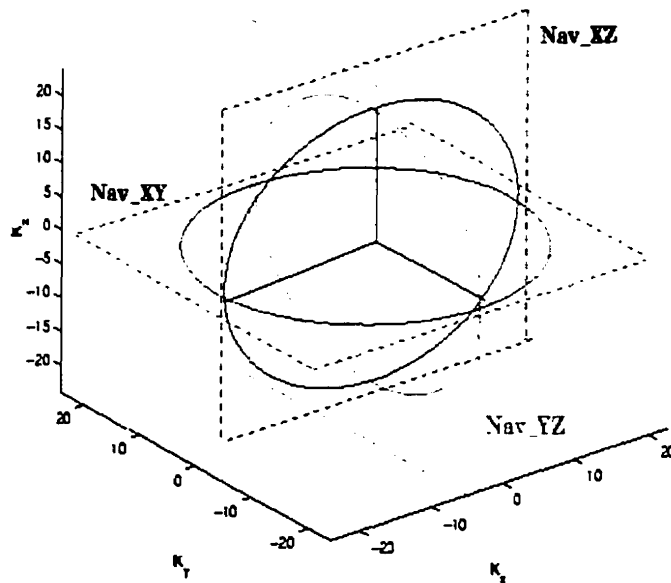
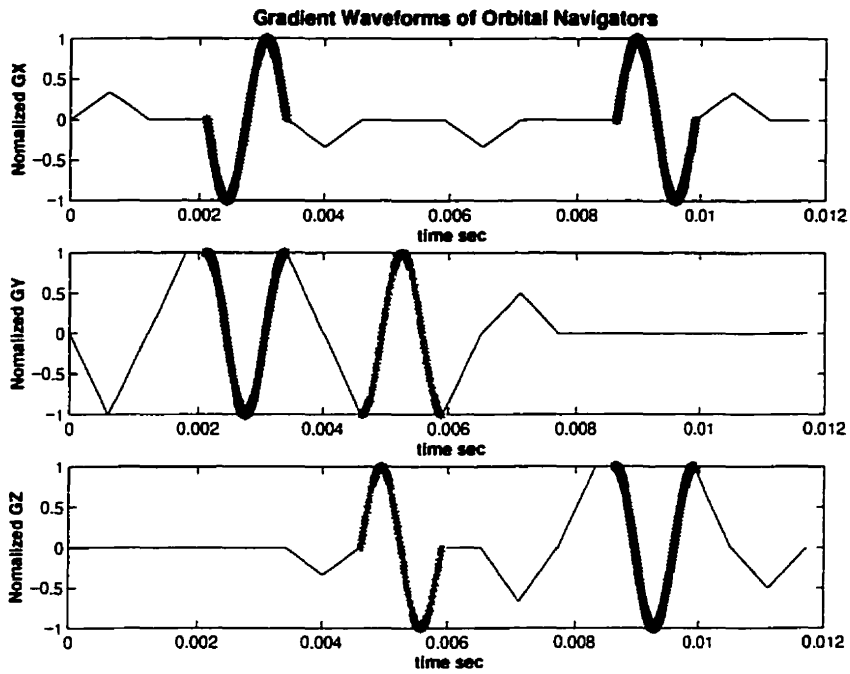


Figure 6.1: a: Gradient waveforms forming three orthogonal orbital navigator trajectories. during the first 0.6 ms, the navigator gradients are turned on to warp the phase to certain radius in k-space. The data acquisition is completed during sinusoidal waveforms (highlighted regions) that correspond to the radial trajectories of b. After a full cycle of each navigator completes, the gradients are rephased to place the next orbital navigator at right radius in the right plane. b shows the acquired trajectories.

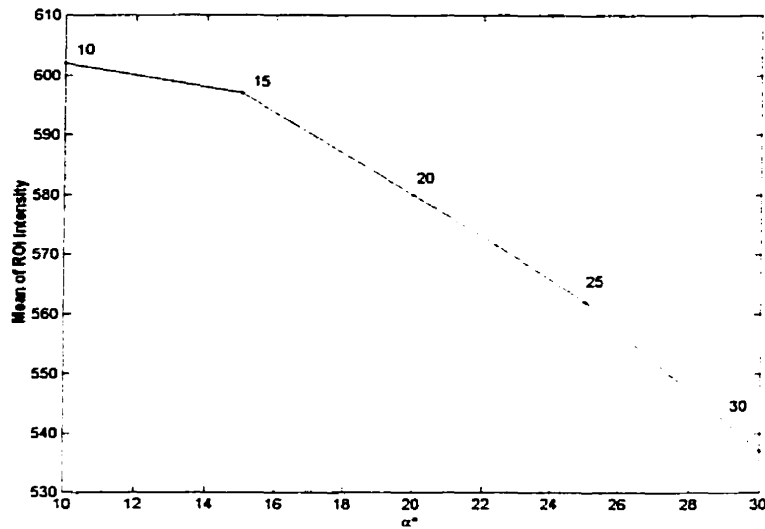


Figure 6.2: Increasing the flip angle of the RF pulse of the navigators lowers the signal intensity in the EPI acquisition. For various flip angles, the mean of the region of interest was obtained by averaging the mean intensity of multiple measurements of a single slice image of a homogeneous water phantom.

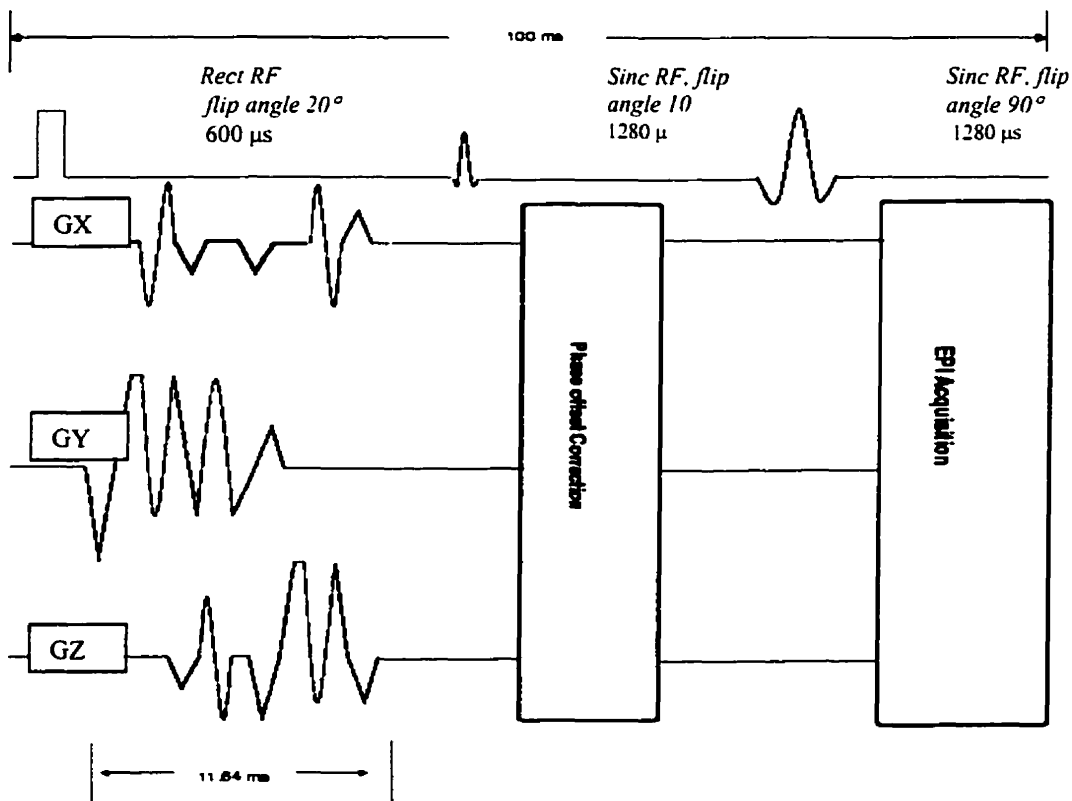


Figure 6.3: Schematic presentation of the navigator equipped EPI sequence with TR=100 msec. The navigator acquisition precedes the image acquisition sequence. The three orthogonal orbital trajectories are formed within 11.64 ms but, each navigator is sampled over 1.28 ms. The sampling intervals are illustrated in red.

6.3 Pulse Sequence Implementation

The experiments were performed on a 1.5 Tesla, Siemens Magnetom Vision system, (Siemens, Erlangen Germany). The orbital navigator pulses were generated by Matlab and compiled by **GENPULSE**, a tool that creates gradient data files readable by the Magnetom Vision system. The gradient data file consisted of 1164 data points at 10 microseconds (the minimum raster time allowed) intervals. Having compiled the external gradient files, they are imported into a program called **PARGEN** (PARAmeter GENerator) that specifies the timing factors of acquisition by providing an interface between the NUMARIS software (operating system) and the Magnetom Vision hardware, in addition to flags that enable user interface functions. All of the image reconstruction tasks are performed via **SPL** (Signal Processing Language) which is an integral part of all measurement related operations on the **NUMARIS/3**.

The navigator data is received via the RF head coil, which serves the dual purpose of RF excitation and signal detection. The cutoff frequency of the lowpass filter is determined by PARGEN with respect to the duration of ADC (analogue to digital conversion). In our sequence, the readout time factor is set to 512 microseconds, which is equal to the duration of acquiring each line of the EPI (readout direction). For a 5mm resolution 64x64 image, the bandwidth in the readout direction of the EPI acquisition is 125 kHz. However, since the navigator gradient waveforms are generated over a finite number of points with a sampling rate of 10 microsecond (raster time), the Magnetom system requires that the ADC duration for acquisition of navigator echoes be a multiple of 10 μ s. Another limitation of the SPL is that the ADC acquisition macro (*sp_adc_rec*, an SPL specific module) does not allow acquisition of different size vectors. Thus the bandwidth of the navigator readouts becomes 50 kHz, which is in the cutoff frequency range of the low pass filter. To increase the bandwidth data acquisition can be performed over smaller segments of the circular navigator, e.g. on each lobe, and the data can be concatenated during postprocessing.

Since SPL does not allow exportation of various size matrices, orbital navigator measurements are formatted as an image file containing 4 lines of data per each navigator; the real, imaginary, phase and the magnitude, which are extracted from the raw data. Data correction and final image reconstruction are performed on PCs running Matlab programs on a Linux platform.

6.4 Correction Algorithms

Having obtained complex data samples from orbital navigators, rotation angles and phase differences due to spatial displacement can be calculated. The ***Rotation Theorem*** of Fourier transform states that *rotation of an object in space results in an equal rotation in its Fourier transform domain*. Assuming $S(k_r, \theta)$ represent the polar form of the complex signal of an orbital trajectory centered at the origin of k-space of the reference object, an angular shift of α around the center of the image results in an equal rotation in the frequency data, yielding in complex $S(k_r, \theta - \alpha)$ whose correlation with $S(k_r, \theta)$ results in an m -point shift in the magnitude of the sampled data, which is robust to phase shifts due to translations. The rotation, can be obtained from $(2\pi m/N)$, where N is number of samples on trajectory that increases from 0 to 2π at a radial distance k_r from the center of k-space. It should be noted that the rotation theorem holds for rotation occurring about the origin of the space, in reality however, the center of rotation is usually shifted from the center of the object [75]. Furthermore, real motion is not constrained to rotation and it involves displacements from the reference position. Either one of these problems can be addressed by ***Shift Theorem***, which states *displacement of an object in a space results in a phase shift in the Fourier transformed space*, the displacement from the origin can be determined from the phase information of the raw data.

6.4.1 Detection of rotation angle and in-plane displacement

It is important to first note that although the set of three navigator echoes spans 3D coordinates of the k-space, individually, they acquire data on a 2D plane. In other words, three data sets obtained from the navigator echoes are capable of resolving the parameters of rotation and displacement happening in the same plane as the navigator

trajectory. However, since navigator trajectories are sampled with high radial resolution ($2\pi/128$ rads) within only 1.3 ms, the speed and resolution provides grounds for assuming that the navigators have captured the motion parameters in all directions simultaneously, hence a motion vector in 3D can be estimated.

The following algorithms obtain the parameters of in-plane motion in xy -, xz - and yz -planes and without loss of generality, assume that the reference frame is at the center of the FOV. In general, the xy -plane corresponds to the slice plane (transverse), even if it is an oblique measurement, the yz - and xz -planes correspond to sagittal and coronal planes, respectively.

In a 2D coordinate system, the Cartesian k -space can be converted to polar coordinates as:

$$k_x = k_r \cos\theta \text{ and } k_y = k_r \sin\theta \text{ and in object space, } r = x \cos\theta + y \sin\theta .$$

Therefore, the reference signal in polar coordinates is

$$S(t) = \iint_{r\theta} m(r, \theta) e^{i2\pi k_r r} dr d\theta^4 \quad (6.1)$$

where $m(r, \theta)$ is a function of the radius and the magnetization signal obtained at that radius from the Bloch equation. When the object is displaced to coordinates (x', y') by a rotation of α and displacement of $(\Delta x, \Delta y)$, the reference coordinates (x, y) would become

$$\begin{aligned} x &= x' \cos \alpha - y' \sin \alpha + \Delta x \\ y &= y' \cos \alpha + x' \sin \alpha + \Delta y \end{aligned} \quad (6.2)$$

therefore

$$\begin{aligned} r' &= [x' \cos \alpha - y' \sin \alpha + \Delta x] \cos \theta + [x' \sin \alpha + y' \cos \alpha + \Delta y] \sin \theta \\ &= [x' \cos(\theta - \alpha) + y' \sin(\theta - \alpha)] + \Delta r \end{aligned} \quad (6.3)$$

where

$$\Delta r = \Delta x \cos \theta + \Delta y \sin \theta \quad (6.4)$$

⁴ Notice that the circular integral element is $rdrd\theta$ and that r is integrated into function. $m(r, \theta)$

Substituting the new reference values into equation 6.1, the new received signal in the case of motion becomes

$$\begin{aligned}
S'(k_r, \theta, t) &= \iint_{xy} m'(r, \theta) e^{i2\pi k_r (r' + \Delta r)} dr d\theta \\
&= \iint_{xy} m(r', \theta - \alpha) e^{i2\pi k_r (r' + \Delta r)} dr d\theta \\
&= e^{i2\pi k_r \Delta r} \iint_{xy} m(r', \theta - \alpha) e^{i2\pi k_r r'} dr' d\theta' \\
&= S(k_r, \theta - \alpha, t) e^{i2\pi k_r \Delta r}.
\end{aligned} \tag{6.5}$$

This equation indicates that rotational motion can be detected from the magnitude of the orbital navigators and that rotation is insensitive to any concurrent translation that is entirely encoded in the phase component of the navigator [75]. Having obtained the magnitude signal of orbital navigators, the rotation angle, α , is determined from cross correlation of the magnitude of the reference navigator with the magnitude of the navigators of subsequent frames.

The second step is to find the displacements of the object by means of examining the phase of the navigator echoes. To do so, it is necessary to rotate the navigator signals back to the reference frame prior to determining phase variations associated with physical displacement or off-center rotation. This involves shifting the complex navigator data by m points. The angular phase difference and consequently, the displacements x_0 and y_0 can be then obtained as described in reference [75]:

$$\begin{aligned}
\Delta\varphi(k_r, \theta) &= \varphi_{S(k_r, \theta)} - \varphi_{S(k_r, \theta - \alpha)} = 2\pi k_r (\Delta x \cos \theta + \Delta y \sin \theta), \\
\Delta x &= \frac{1}{k_r} \int_0^{2\pi} \Delta\varphi(k_r, \theta) \cos(\theta) d\theta \quad \text{and} \quad \Delta y = \frac{1}{k_r} \int_0^{2\pi} \Delta\varphi(k_r, \theta) \sin(\theta) d\theta.
\end{aligned} \tag{6.4}$$

Alternatively, a new k_r trajectory can be calculated by taking the rotation angle into account

$$\begin{aligned}
\Delta\varphi(k_r, \theta) &= \varphi_{S(k_r, \theta)} - \varphi_{S(k_r, \theta - \alpha)} = 2\pi k_r (\Delta x \cos(\theta - \alpha) + \Delta y \sin(\theta - \alpha)), \\
[\Delta\varphi(x, y)]_{N \times 1} &= 2\pi k_r [\cos(\theta_n - \alpha) \quad \sin(\theta_n - \alpha)]_{N \times 2} \begin{bmatrix} \Delta x \\ \Delta y \end{bmatrix}_{2 \times 1}
\end{aligned} \tag{6.5}$$

where θ_n denotes the incremental sampling of azimuth angle from 0 to 2π . Δx and Δy are determined from solving the above linear system[88].

Due to presence of noise and phase unwrapping errors, estimation of displacement from the phase data by the above methods may be unstable. Although low pass filtering the data improves the results to some extent, they remain far from perfect. A Nelder-Mead simplex algorithm, implemented in Matlab, is used to non-linearly fit the complex navigator data to a complex reference by demodulating the phase of the navigator as a function of dx and dy , expressed in the form of $e^{-j(k_x \cos(\theta) dx + k_y \sin(\theta) dy)}$. The fit determines dx and dy that minimize the distance, L between the reference (S_{ref}) and the phase demodulated xy -navigator data (S_{nav}) in a least square sense:

$$L(d_x, d_y) = \sum_{i=1}^N \left| S_{ref}(\theta_i) - e^{-j(k_x \cos(\theta_i) dx + k_y \sin(\theta_i) dy)} S_{nav}(\theta_i) \right|^2 \quad (6.6)$$

where θ_i is the angle at which the navigator data is sampled. The procedure is repeated analogously in xz and yz directions.

6.4.2 Correction

As stated by Fourier rotation theorem, if an object is rotated, its frequency components in the Fourier domain are rotated as well. However, in EPI acquisitions, the data samples are obtained over a finite dimension Cartesian grid, which can be seen as a 2D **rect** filter truncating the raw data. Unless realtime motion detection and gradient adjustment mechanisms are in place, the orientation of this **rect** filter does not vary with the rotation of the Fourier domain. Consequently, while comparing frames to the reference, some of the rotated raw data may fall beyond the boundaries of the rectangular sampling grid of the reference image. Given the limited extent of head motion in fMRI studies, this problem does not pose a major difficulty in our case and the most limiting factor in correction of rotation is optimal interpolation of the rotated data to fit the rectilinear grid anticipated by the fast Fourier transformation algorithm used in image reconstruction. Interpolation algorithms themselves introduce artifacts to the reconstructed image [74] which are not well tolerated in low SNR fMRI studies.

The first step in correcting the effects of a complex motion is to correct for phase shifts resulting from translation or off-center rotation. Translation-related errors can be resolved by phase demodulation of the entire raw data space by $e^{-j\Delta\varphi_x}$ across the y axis and $e^{-j\Delta\varphi_y}$ across the x axis of the raw image [47] where

$$\Delta\varphi_x(i) = 2\pi\Delta x k_{xi} \text{ where } k_{xi} = i \frac{1}{FOV_x} \text{ and } i = -N/2 \rightarrow N/2 \text{ and similarly,}$$

$$\Delta\varphi_y(i) = 2\pi\Delta y \pi k_{yi} \text{ where } k_{yi} = i \frac{1}{FOV_y} \text{ and } i = -N/2 \rightarrow N/2.$$

Having phase demodulated the raw data, to correct for rotation, first the image is reconstructed by 2D Fourier transform and then the reconstructed image is rotated by the measured angle. The image rotation is done by first, obtaining the center of rotation, which is assumed to be the center of gravity (COG) of the images, and then resampling the image by means of linear transformation. The transformation matrix was calculated from the parameters of rotation, i.e. the center of rotation, the rotation axes and rotation angles, by **minctracc**, an image registration software package developed at the Brain Imaging Center [98].

Alternatively, Runge *et al* [43] have proposed a method where following the correction of phase shifts, the phase of every measured data point $F(k_x, k_y)$ is transformed as

$$\varphi(x, y, Kx, Ky) = (Kx, Ky) \begin{pmatrix} \cos\alpha & -\sin\alpha \\ \sin\alpha & \cos\alpha \end{pmatrix} \begin{pmatrix} x \\ y \end{pmatrix} \quad (6.7)$$

and the image is reconstructed from the summation of all data points:

$$I(x, y) = \left| \sum_{k_x, k_y} F(k_x, k_y) e^{-j\varphi(x, y, k_x, k_y)} \right|, \text{ without FFT.} \quad (6.8)$$

In this work, the first of the above correction algorithms is implemented as a part of the post processing procedure in fMRI analysis. Figure 6.4 schematically illustrates the prospective motion correction procedures as implemented.

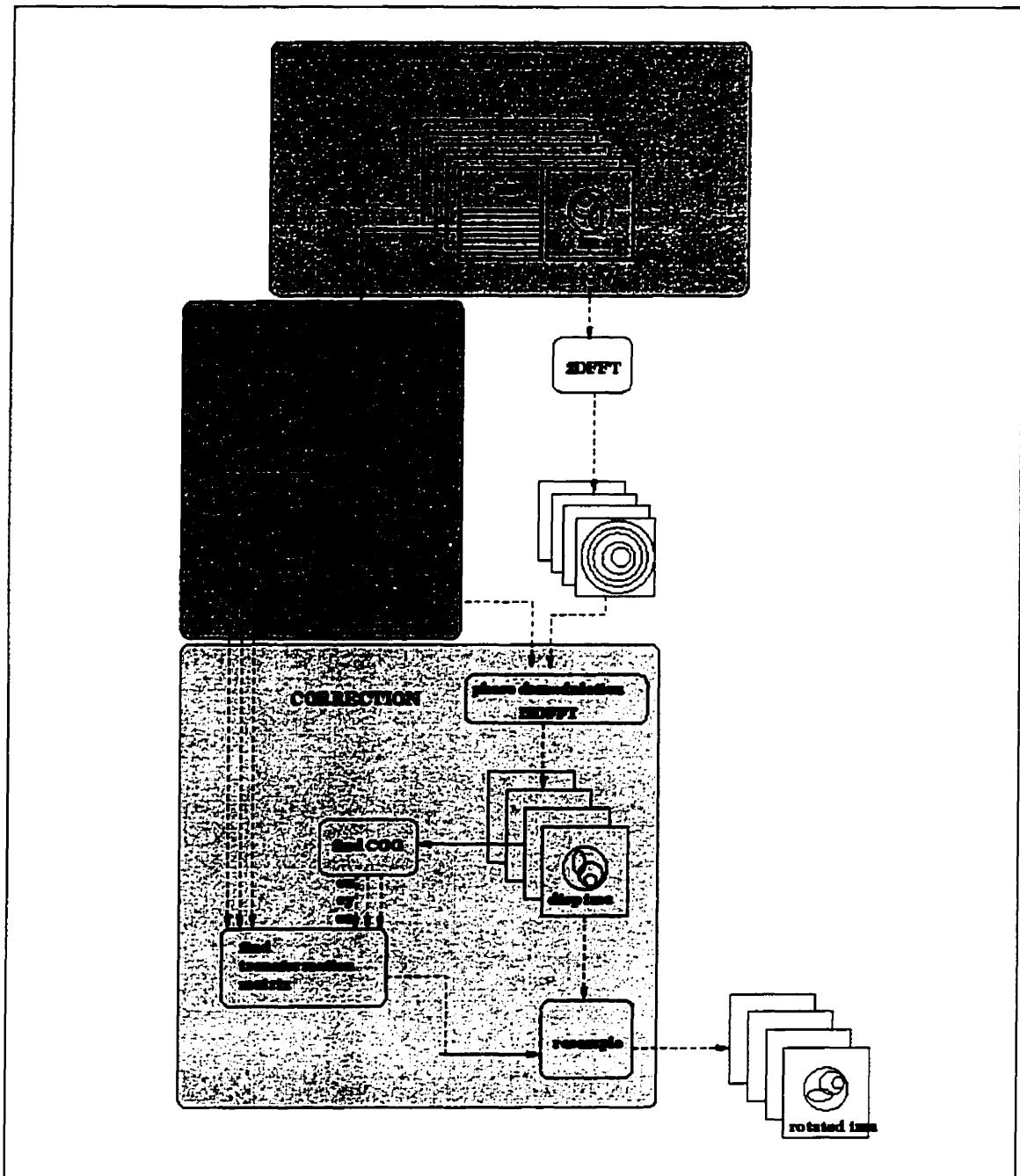


Figure 6.4: Each data set consists of two files that are exported from NUMARIS to local file system. The files are of the same format; one of them carrying the reconstructed image and the other, the profiles of the three navigator echoes, saved as lines of the image matrix. Motion detection involves extracting the motion parameters by calculating the difference in phase and the shifts in magnitude of all navigators with respect to the phase and magnitude of the reference navigator. Having obtained the displacements and the rotations, phase demodulation of the Fourier transformation of the image corrects the translational displacement, this corrected image is then rotated about its center of gravity by the angle calculated in the previous step, by means of linear transformation.

Chapter 7

3D-Orbital Navigators: *Experiments*

7.1 Numerical Simulations

To validate the motion estimation algorithms, an analytical phantom was designed in the Fourier domain and the navigator data was simulated by evaluating the analytical function at coordinates corresponding to an in plane orbital trajectory. Random complex noise was added to the simulated navigator profiles and the accuracy of the algorithm in presence of noise was tested.

7.1.1 Methods

The phantom was constructed by multiple elliptical objects positioned at different angles and positions from the center of the image. The phantoms were both constructed in image domain (Figure 7.1) and reconstructed from the analytical Fourier transformation (Figure 7.2).

Analytical navigator data set was obtained by evaluating the function F over a circular trajectory at radial distance k_r ,

$$\begin{aligned} k_x &= k_r \cos(\theta) \\ k_y &= k_r \sin(\theta) \end{aligned} \quad (7.1)$$

where $\theta = [0 \ 2\pi]$, is defined over 128 points, providing an azimuthal resolution of $2\pi/128$ rad or 2.81° and k_r is chosen to be $10/\text{FOV } m^{-1}$.

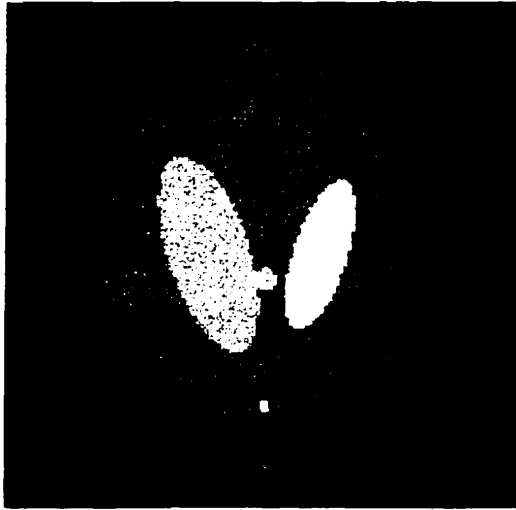
A rotation of φ rads and displacement of dx and dy modify function F as:

$$F' = e^{-j(k_x dx - k_y dy)} F(k'_x, k'_y, C_i, a_i, b_i, \alpha_i, x_i, y_i) \quad (7.2)$$

where

$$\begin{bmatrix} k'_x \\ k'_y \end{bmatrix} = \begin{bmatrix} k_x \\ k_y \end{bmatrix} \begin{bmatrix} \cos(\varphi) & \sin(\varphi) \\ -\sin(\varphi) & \cos(\varphi) \end{bmatrix} \quad (7.3)$$

Figure 7.3 illustrates the profile of the analytical orbital navigator corresponding to phantom of image 7.2 before and after displacement.



$$\text{Image} = \sum_{i=1:N} I(C_i, a_i, b_i, \alpha_i, x_{0i}, y_{0i}),$$

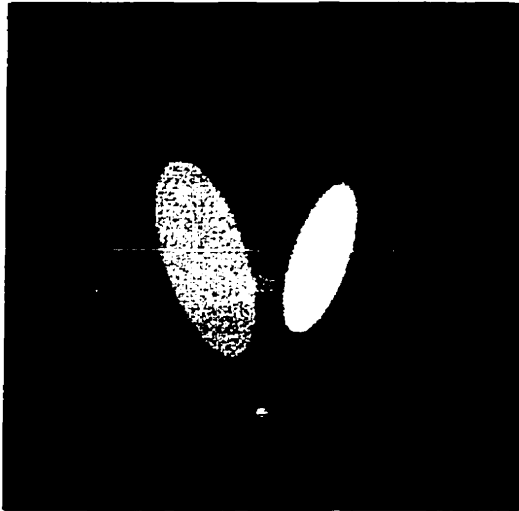
where

$$I(C_i, a_i, b_i, \alpha_i, x_{0i}, y_{0i}) = \begin{cases} C_i & \text{if } \frac{(X-x_{0i})^2}{a_i^2} + \frac{(Y-y_{0i})^2}{b_i^2} \leq 1 \\ 0 & \text{otherwise} \end{cases}$$

where

$$\begin{bmatrix} X \\ Y \end{bmatrix} = \begin{bmatrix} x \\ y \end{bmatrix} \begin{bmatrix} \cos(\alpha_i) & \sin(\alpha_i) \\ -\sin(\alpha_i) & \cos(\alpha_i) \end{bmatrix}$$

Figure 7.1: Digital radon phantom is created geometrically by assigning different contrast values to the pixels that correspond to an elliptical surface on a Cartesian grid.



$$\text{Image} = \text{IFT}_{2D} \sum_{i=1:N} F(k_x, k_y, C_i, a_i, b_i, \alpha_i, x_{0i}, y_{0i}),$$

where

$$F(k_x, k_y, C_i, a_i, b_i, \alpha_i, x_{0i}, y_{0i}) =$$

$$C_i (\pi a_i b_i) e^{-i\phi_i} \frac{J_1(\sqrt{(K_x a_i)^2 + (K_y b_i)^2})}{2\pi \sqrt{(K_x a_i)^2 + (K_y b_i)^2}}$$

where

$$\phi_i = k_x x_{0i} + k_y y_{0i}$$

and

$$\begin{bmatrix} K_x \\ K_y \end{bmatrix} = \begin{bmatrix} k_x \\ k_y \end{bmatrix} \begin{bmatrix} \cos(\alpha_i) & \sin(\alpha_i) \\ -\sin(\alpha_i) & \cos(\alpha_i) \end{bmatrix}.$$

Figure 7.2: This phantom is obtained from inverse Fourier transformation of the analytical expression of each of the ellipsoids. The analytical Fourier domain expression for an ellipse is an elongated jinc function. The image is obtained over a 128x128 Cartesian grid in k-space, with $\Delta k = 200/64 \text{ m}^{-1}$.

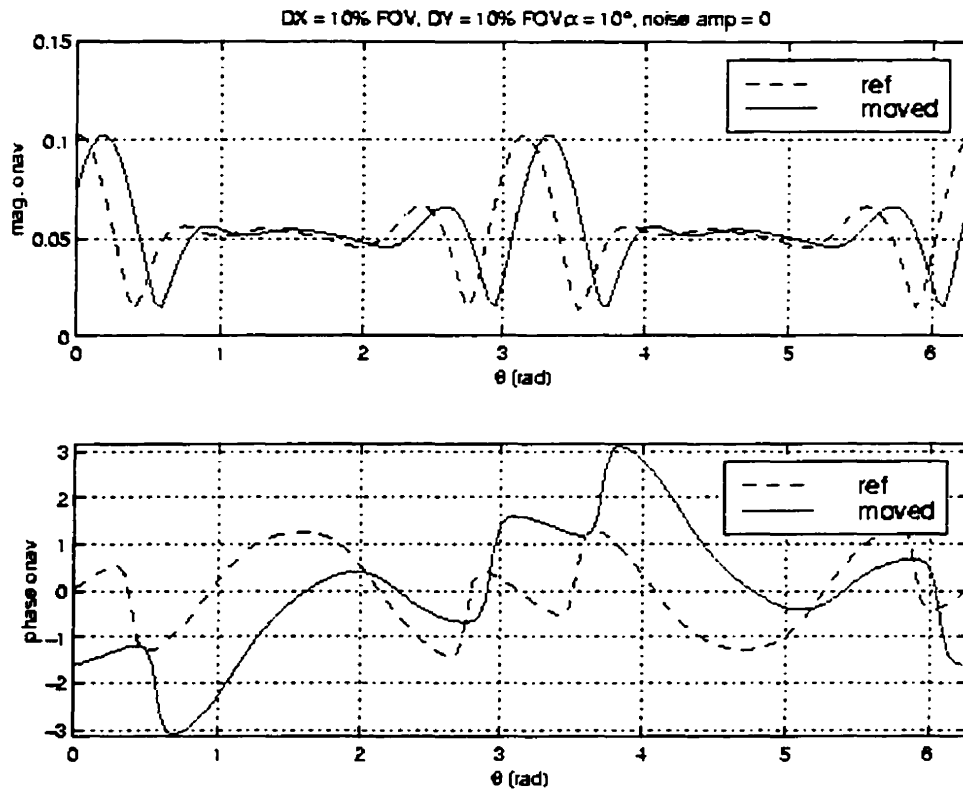


Figure 7.3: Magnitude and phase behavior of navigator echoes in presence of rotation and displacement. The magnitude of the navigator echo is just shifted equal to rotation angle, the phase undergoes a linear increment, in addition to being shifted along the azimuth angle. This phase difference is a sinusoid whose amplitude is proportional to DX and DY.

To test the sensitivity of the motion parameter estimation to noise, complex random noise was added to both the reference and the displaced analytical complex navigator data. The signal to noise ratio was defined as

$$SNR = \frac{\mu_{|S_{nav}|}}{\sigma_{|noise|}}$$

i.e. the mean of the magnitude of the navigator signal over the standard deviation of the noise magnitude.

7.1.2 Results

In the first set of tests, the simulated phantom was displaced by 10% of FOV in X direction and rotated by 10 degrees and displacement and rotation were calculated as the noise magnitude was increased. As illustrated in Figure 7.4, the accuracy of the motion detection algorithm is relatively independent of low noise, and that errors are below the sub-pixel range. The second test involved testing the accuracy of the algorithm to the extent of rotation and displacement in the presence of random complex noise. In these tests, for a constant SNR, the simulation phantom was shifted in x and y direction and rotation in the xy-plane (see Figure 7.5).

7.1.3 Discussion

One of the limitations in calculation of motion parameters is to detect the sub-sample shifts due to rotation from the magnitude data and to revert this shift in the profile of the corresponding raw data prior to estimating the displacement parameters from the phase analysis. One way of overcoming this problem would be to increase the sampling rate. Although a viable option in simulation, timing constraints of the actual MR experiment, as discussed in the previous chapter, do not allow for very high sampling frequencies. Therefore, cubic interpolation was chosen as a means of decreasing the sampling intervals. Figures 7.5, 7.6 and 7.7 demonstrate the accuracy of motion estimation algorithm in presence of noise for increasing displacements and rotation angle. The interpolation factor for these results was heuristically chosen to be 5, thus increasing the azimuthal sampling intervals from 2.81° to 0.56° .

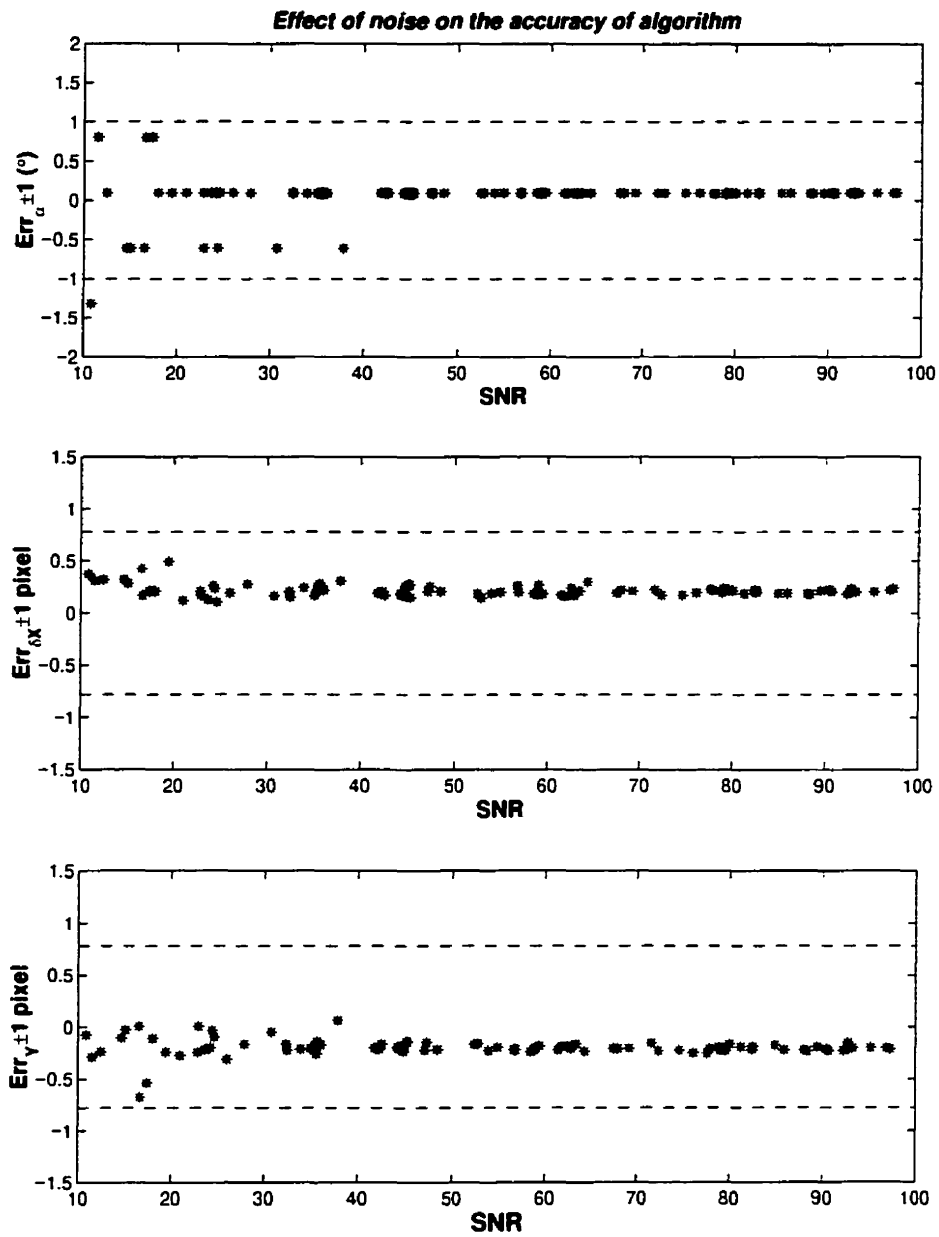


Figure 7.4: The sensitivity of motion detection algorithm to random normal noise was tested. Random noise of increasing amplitude was added to both reference and rotated navigator data and displacements obtained from measurements were compared to those imposed.

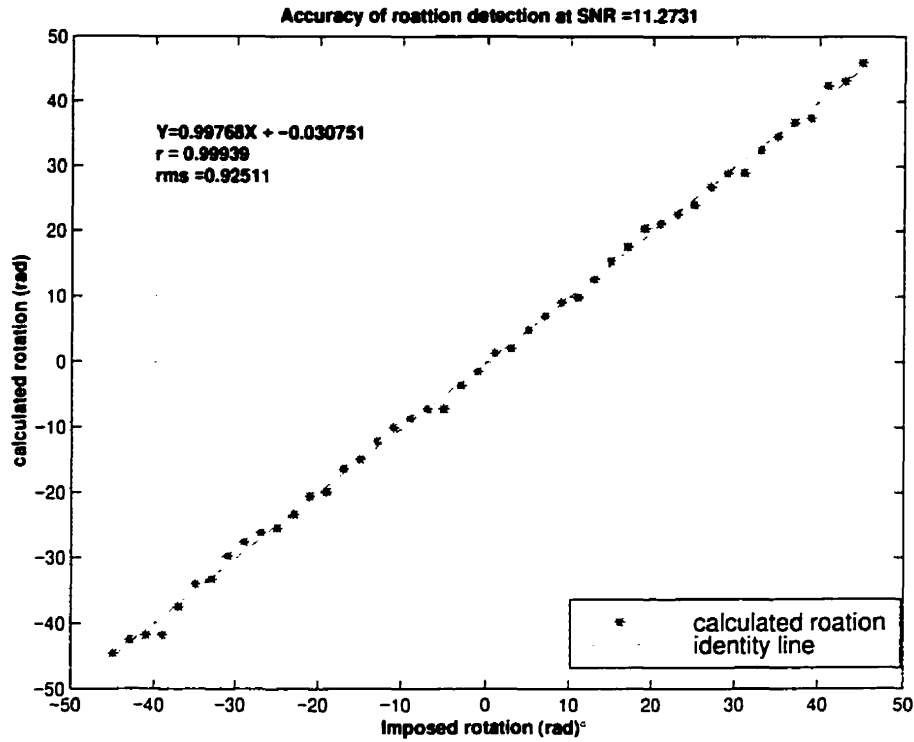
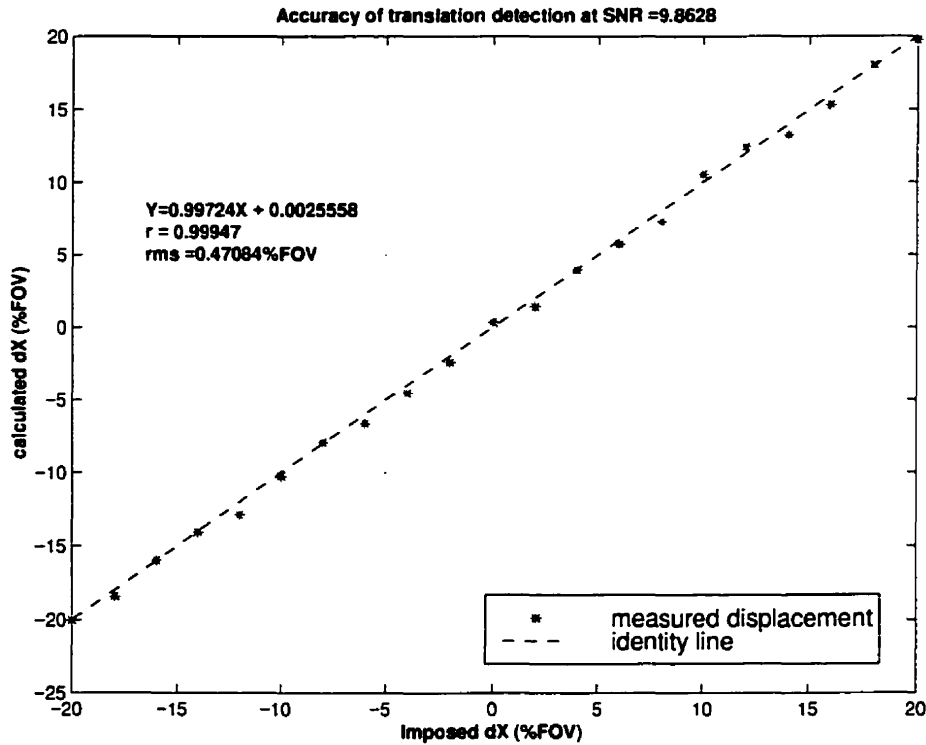


Figure 7.5 The rotation angle was varied between $-\pi/4$ to $\pi/4$, the algorithm extracts the rotation angles correctly from the noise contaminated navigator magnitude.



7.6 To test the accuracy of translation detection along X axis, the phantom was gradually moved by as far as 25% of FOV in X direction, while being kept offset by 10% of FOV in the Y direction. A constant rotation of 10° was applied. SNR was set to ~ 9 that corresponds to the realistic SNR of the navigators.

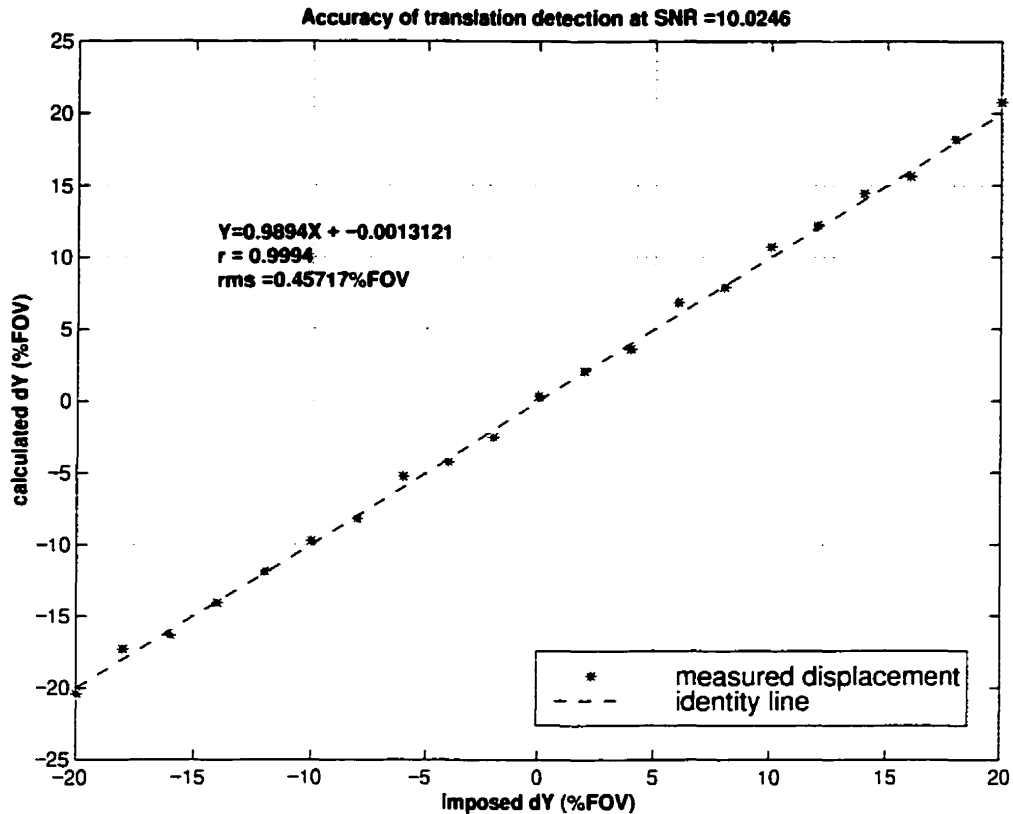


Figure 7.7: Similarly to above the accuracy of translation detection along Y axis was validated by shifting the analytical phantom gradually in y direction in presence of noise.

7.2 Phantom Experimentss

In vitro phantom studies were performed to validate the accuracy of the Fourier shift and rotation theorems in real MRI experiments.

7.2.1 Methods

A solid phantom consisting of contrasting layers of agar gel with 1%, 2%, 4% and 8% concentrations plus two water- and one air-filled tubes was prepared. A phantom support was designed to allow controlled axial rotation and longitudinal displacement of the phantom (Figure 7.8). The phantom was connected to the rotating axel of the support system by a plastic universal joint that creates a backlash of $\sim 0.5^\circ$; the accuracy of the rotation mechanism of the support system was tested with a laser displacement sensor (LDS 90/40, DynaVision, Dynamic Control System, Vancouver, Canada) capable of resolving rotation increments of 0.33° . Phantom support which is installed in the head coil allows two degrees of motion freedom: axial rotation and sagittal translation. The

rotations are measured by a protractor, centered about the longitudinal axis of the phantom, which slides along a ruler. The measurement support device is installed at the end of the magnet and is operated manually. The rod connecting the support system to the phantom is long enough (~1 meter) to ensure that the magnetic field homogeneity is not affected by the operator.

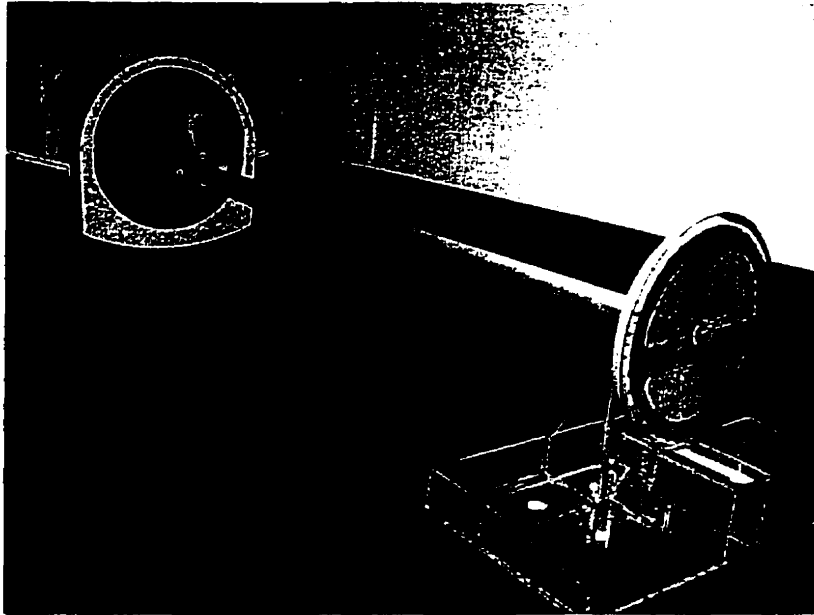


Figure 7.6: The phantom support and the measurement mechanism

The phantom experiments involved:

- 1) test of translation where 123 single slice images of the phantom were obtained sagittally in the YZ plane of the magnet, while the phantom was moved in the sagittal direction after every 10 acquisition.
- 2) test of rotation where 123 single slice images of the phantom were obtained axially in the XY plane of the magnet, while the phantom was rotation about the center of the object, i.e, z-axis.
- 3) test of complex motion where single slice EPI acquisitions were performed in axial(xy) plane while the object was shifted along $\pm z$ -axis and rotated about the z-axis in both direction.

To ensure that the data is collected at the steady state, three first frames of each study were discarded.

7.2.2 Test of translation

7.2.2.1 Results

To observe the changes of the navigators raw data to gradual displacement, the magnitude and the phase of the repeated measurements of the navigators are extracted from the raw navigator data and saved as image files separately (Figure 7.9). These files are analyzed separately and the parameters of motion are extracted for each navigator data (Figure 7.10). To test the accuracy of the measurement, the measured displacements were linearly fit to the actual displacement vector and plotted (Figure 7.11). The rms error and the correlation coefficient between actual and measured displacements were calculated as measures of accuracy. Motion correction algorithm based on phase demodulation was tested for the case of 22 mm sagittal displacement (Figure 7.12).

7.2.2.2 Discussion

As illustrated in Figure 7.9, the translational motion affects only the phase of the navigators that spans the axis of motion, in this case, XZ and YZ planes. The XY navigator in this case, is perpendicular to the plane of motion and the small phase shifts are more likely to be due to signal changed due to new structures that enter this plane. As expected from the Fourier shift theorem, the magnitudes of the navigator echoes in all three cases remain unchanged. Figure 7.9 illustrated that the navigators have high SNR and stable phase that ensures small variance between different estimation of the same displacement (Figure 7.10). The slight (~0.1 mm) increase in the first displacement may reflect the translational backlash produced as the operator moves the phantom. A comparison of the actual displacement with those obtained from the navigator-based estimation yields a correlation coefficient factor of $r=0.9993$ and an rms error of 0.85mm. A linear fit of the estimated data to the actual measurements gives a slope of 1.0128 (Figure 7.11) that confirms the accuracy of the motion detection technique.

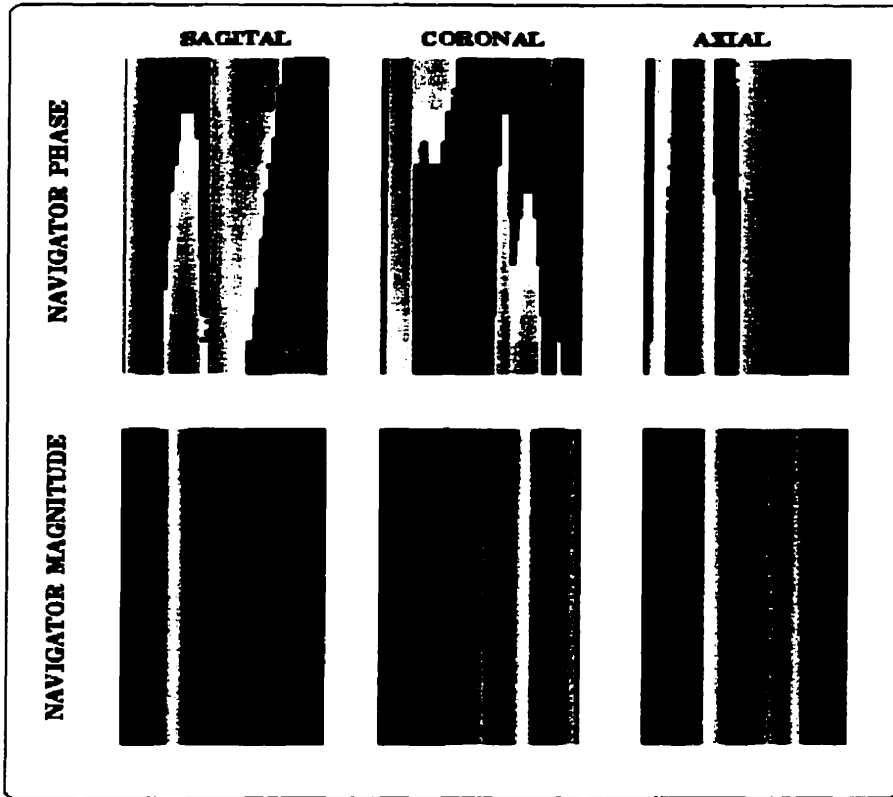


Figure 7.9: Magnitude and phase of each navigator extracted from the raw data obtained from repeated measurements of a phantom that moves in the sagittal direction after every 10 measurements.

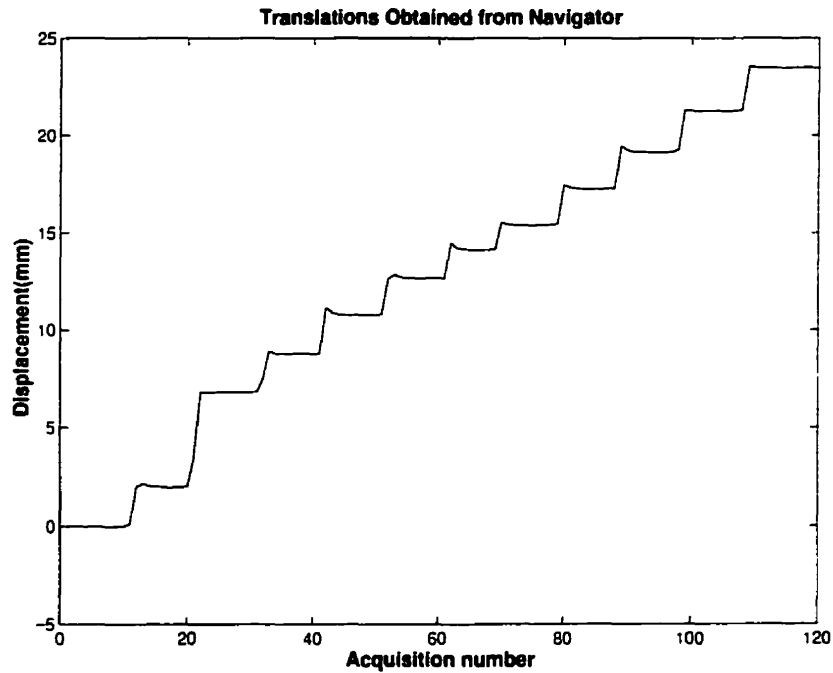


Figure 7.10: Test of stability of translation measurement; the stepwise increments correspond to the displacement of the object from the reference position after every 10 acquisition.

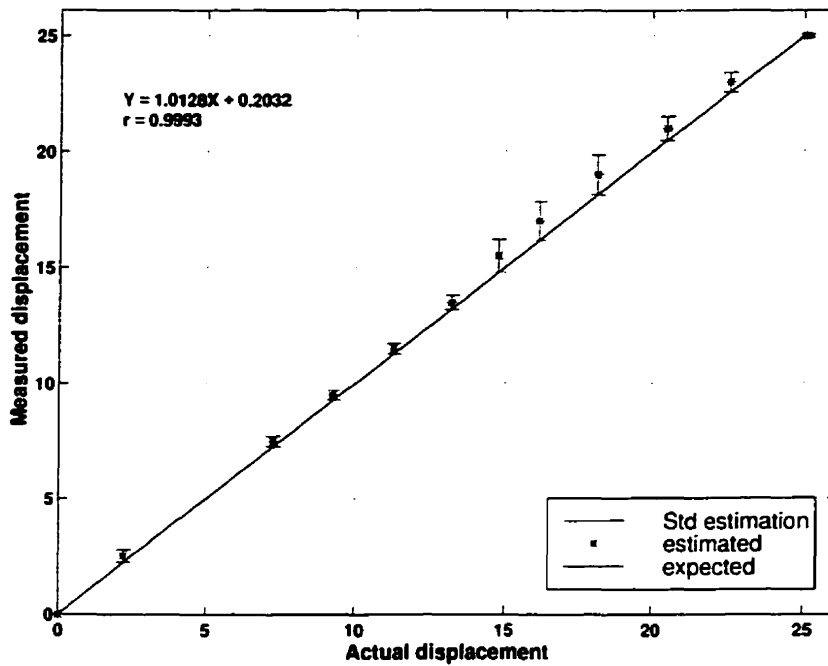


Figure 7.11: Accuracy of motion detection algorithm. Error bars correspond to the standard deviation of displacements obtained at each position.

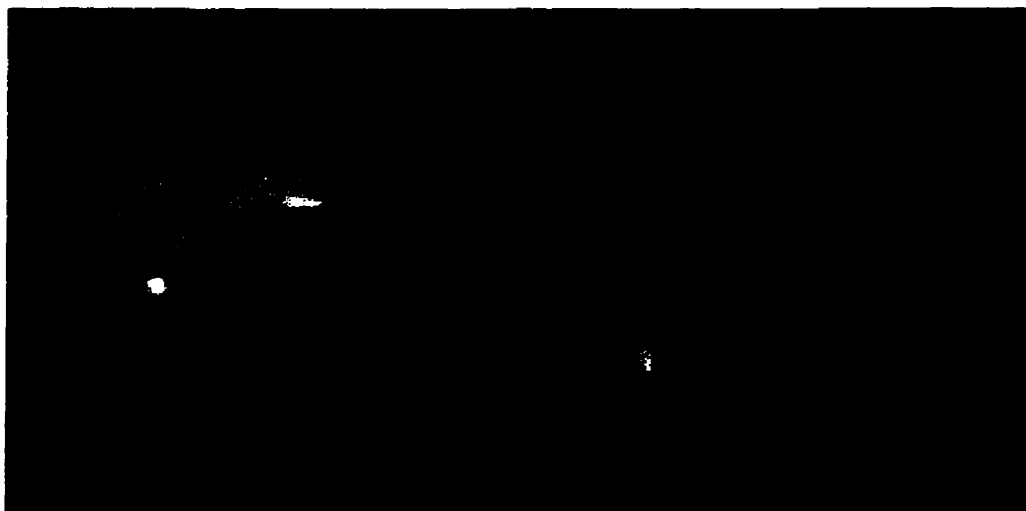


Figure 7.12: Example of difference images before and after correction. The phantom was displaced by 22 mm in the sagittal direction.

7.2.3 Test of rotation

7.2.3.1 Results

Figure 7.13 illustrates the small shifts corresponding to angle increments of $\sim 2.5^\circ$ in the magnitude of the axial navigators while the phantom was gradually rotated from 0 to 30° (The first obvious shift corresponds to 6° rotation). These shifts correspond to stepwise rotations calculated by the algorithm, demonstrated in Figure 7.14. Similarly to above the parameters of rotation were estimated from the navigator data and the accuracy of estimation was verified by calculating rms error, correlation coefficient and the slope of fitting the estimated parameters to the actual measurement data. It was observed that the similarity between the shape of the magnitude of the reference and the current navigator decreased as the rotation angle increased. Figure 7.15 demonstrates a stepwise decrease in correlation between the reference and the navigator as the rotation angle increases.

7.2.3.2 Discussion

One of the problems with the rotation algorithm is the quantization noise arising from the proximity of the maximum peak of the cross correlation function that determines the shifts in the magnitude data. One of the sources of this problem could be the low azimuthal resolution of the navigator sampling. In full circle navigators, the sampling intervals are $360^\circ/64$; in other words, each shift corresponds to 5.63° . In order to increase the angular resolution of the navigators, the magnitude of the navigators was cubically interpolated (by a factor of 9). Although this reduced the magnitude of the quantization noise, it did not eliminate it. Another possibility to increase the sampling rate would be to acquire the navigator data over half a circle, thus increasing the angular resolution by a factor of two.

It was observed that the cross correlation coefficient decreases with increments in rotation angle (Figure 7.15). One possible cause of this drift would be a small shift at the iso-center of the orbital navigator gradients that results in deviation from the Fourier rotation theorem. The other cause may be small through plane motion, due to backlash of the device and the torque produced during rotating the object, that introduces signal from new structure into the profile of the navigator data. In either case, the accuracy of rotation

correction was limited to a range of 0-30°. Figure 7.16 illustrates the rotation angles obtained from navigators versus the actual rotation angles. A correlation of 0.98 between the calculated and the actual rotations demonstrates accuracy of the technique. The rms error was of the order of 0.37° and a slope of almost one was obtained from linear fitting of the measurements to the identity line (Figure 7.16). Figure 7.17 shows an example of the corrected image in case of 20° rotation.

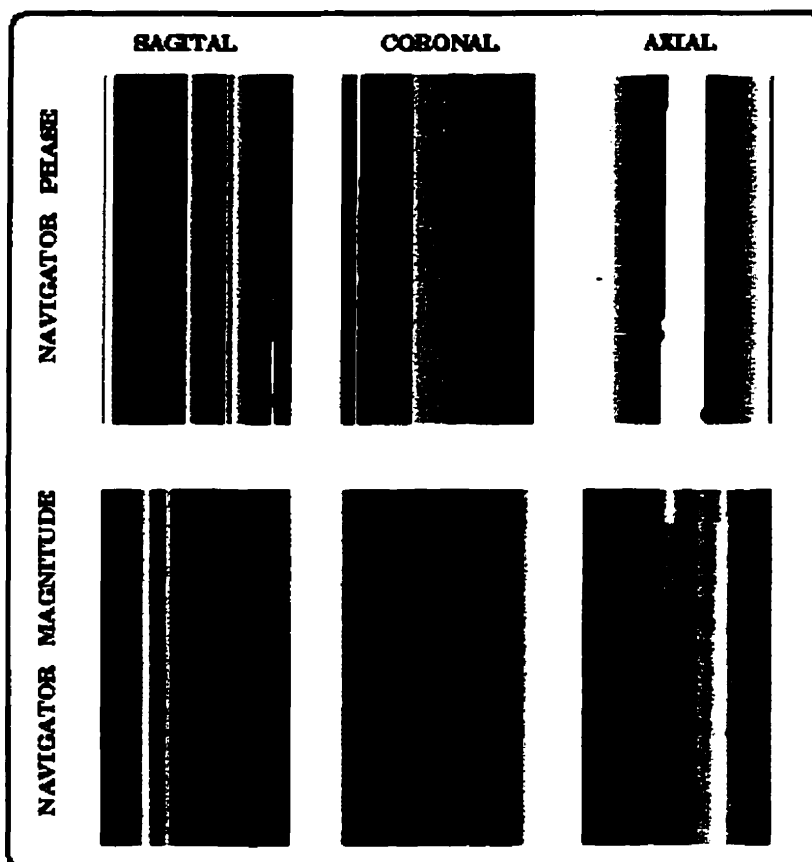


Figure 7.13: Magnitude and phase of repeated acquisitions of each of the navigators during the rotation of the phantom in the axial plane are extracted separately and displayed.

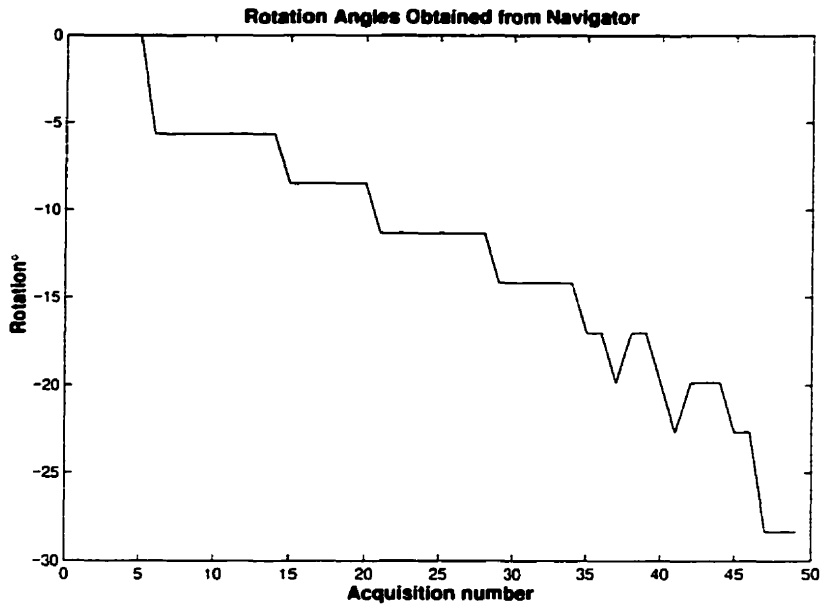


Figure 7.14 The stability of rotation algorithm in actual measurements was tested. Multiple measurements of the phantom in rotated positions were obtained and the data was interpolated by a factor of 4.

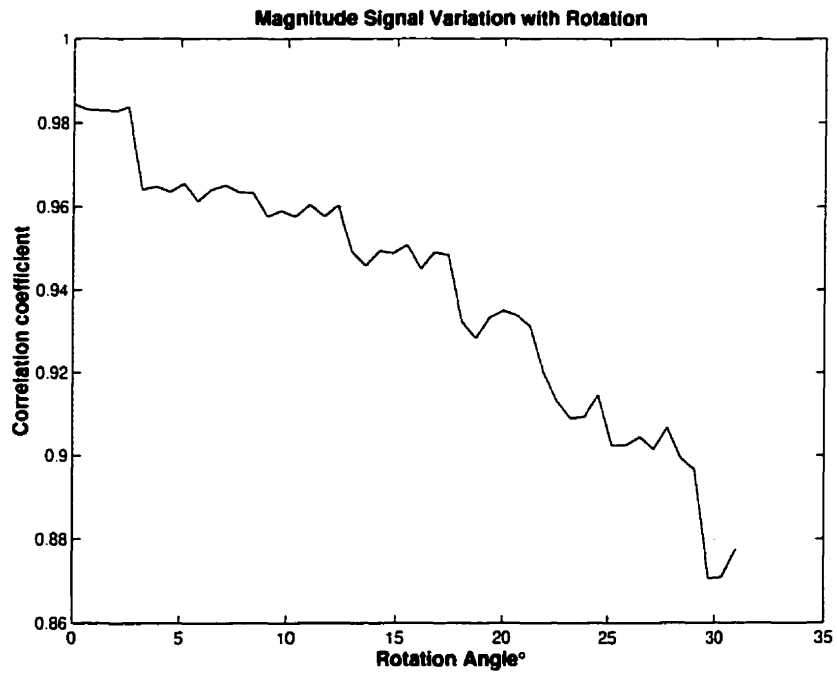


Figure 7.15: The correlation coefficient between the reference and the rotated navigators decreases with increase in the rotation angles.

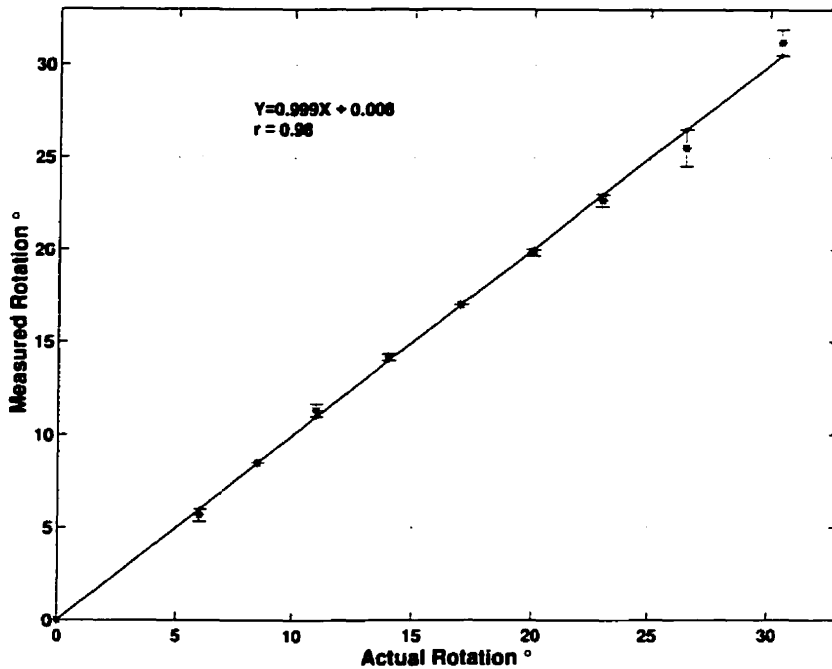


Figure 7.16: Comparison of the rotation angles obtained from navigator echoes versus actual measurements. The error bars represent the mean of error between actual and estimated rotation angles.

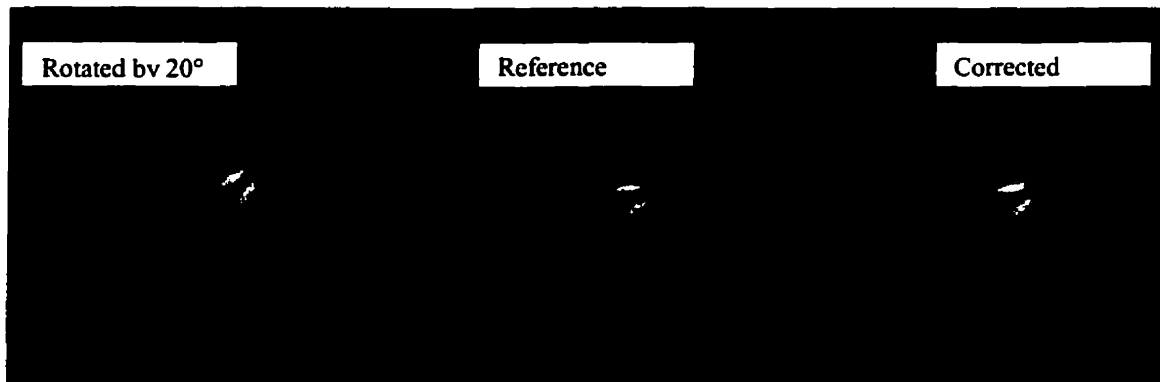


Figure 7.17 Rotation correction was automatically performed using *mincresample* package. The transformation matrices were obtained from the parameters of motion.

7.2.4 Complex motion

7.2.4.1 Results

In this experiment, the rotational and translational movements of the phantom were interleaved. Figure 7.18 illustrates the amplitude of sagittal (Δz) shifts and axial rotations on the same plot in order to show the order of their execution in the acquisition cycle. The purpose of this test was to ensure that navigator echoes measure the displacements in 3D regardless of the direction of EPI acquisition. Figure 7.19 shows the parameters of motion along different axes where the longitudinal motion is estimated

from both coronal(xz) and sagittal(yz) navigators and the transverse displacements are extracted from axial navigators (xy) (Figure 7.19c).

7.2.4.2 Discussion

The purpose of this test was to assess the accuracy of multi-axial motion measurements and to show that the navigator measurements are independent of the preferred direction of the EPI acquisition. As illustrated in Figure 7.19, the displacements along x and y direction are insignificant compared to those in along z -axis. The small displacements in x and y directions correlates with the degree of rotation and could be due to the slight offset shift of the iso-center of the orbital gradient fields from the center of the k -space. These displacements can also be caused by the torque-induced shifts along the axis of rotation, as discussed earlier. The rms errors are of the order of 0.87 mm and 0.98°. The slight difference in the Δz 's obtained from coronal and sagittal navigators may reflect the delay of ~ 3 ms between the acquisition of these echoes. This test establishes that the measurement of motion is independent of the preferred plane of acquisition and that the navigators can resolve parameters of multi-axial motion.

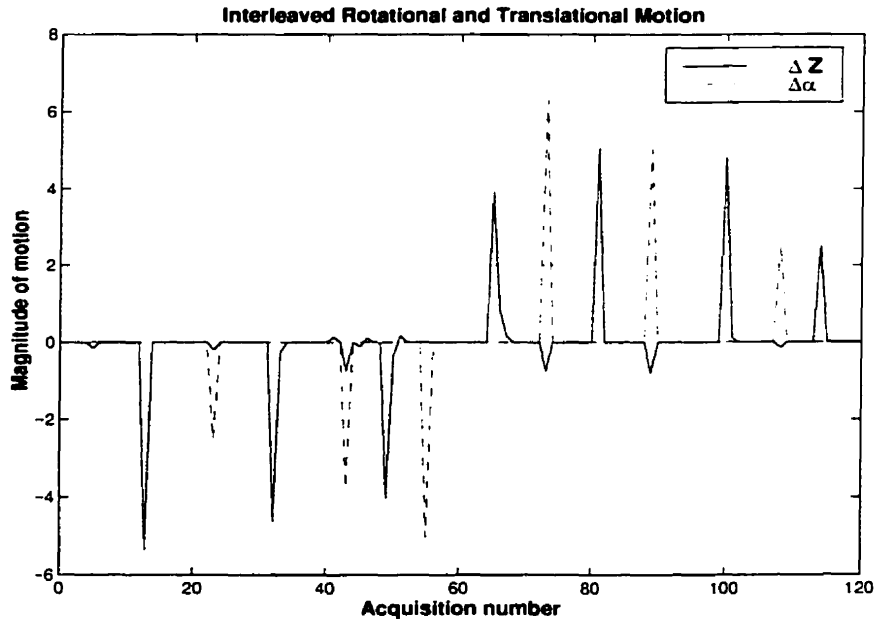


Figure 7.18 Interleaved rotation and translations are presented simultaneously to show the timing of the event. The y-label of the graph corresponds to the magnitude of rotation (about z-axis) in degrees and that of translation (along z-axis) in mms.

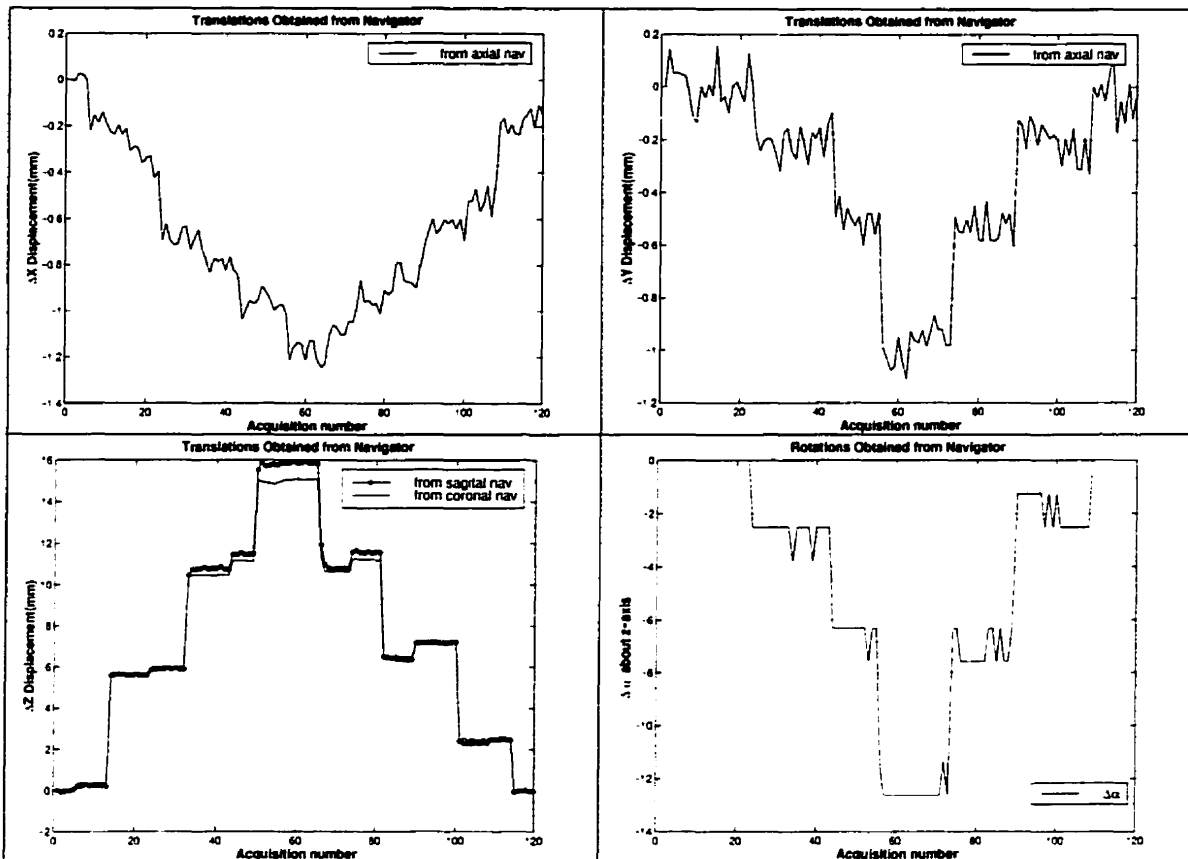


Figure 7.19: Estimation of the parameters of complex motion. The displacement of the object in dx and dy direction are insignificant (a,b). The difference in the amplitude of large motion ($>15\text{mm}$) detected by coronal versus sagittal navigators may reflect the delay between these two acquisitions (c). The accuracy of axial rotation detection, minus the quantization errors, was not affected by the longitudinal displacement (d).

7.3 In-Vivo Human Experiments

The purpose of these experiments was to test the sensitivity of the navigator echoes to gross patient movement and to examine the possibility of using the orbital navigators for monitoring the motion induced during the respiratory cycle.

7.3.1 Gross subject motion

7.3.1.1 Methods

The subject was asked to make sagittal movements by bending her knees to a relatively constant position. A knee rest was used to help the subject regulate her movements as much as possible. Multiple frames (120 frames) of single slice images of the head were obtained from EPI acquisition in sagittal direction in one second intervals, while the subject was moving after each 10 frames.

7.3.1.2 Results

Figure 7.20 illustrates the estimated parameters of the subject motion. Small rotation angles in the sagittal plane correspond to the small nodding movements of the head in this direction. Motion correction based on these estimated parameters on the time series reduces the standard deviation between the magnitude of the difference images from 18.9 before correction to 8.9 after correction (Figure 7.21). The rms of the intensity difference is also reduced from 39.3 to 32.5, after correction. An example of the difference image obtained before and after motion correction is presented in Figure 7.22.

7.3.1.3 Discussion

Stable measurements of the subject periodic motion illustrated in Figure 7.20 provide grounds for the application of this method in inter-view displacement correction. Although navigator echoes are measured independently of the image acquisition and in theory they can measure the intra-view motion, the displacement measurements will not render useful in case of shape distortion due to movement during the EPI acquisition. The correction algorithm used to produce the difference images can be improved by cubic interpolation or spline resampling in order to further reduce the rms of the difference image intensity.

7.3.2 Monitoring the respiratory cycle

7.3.2.1 Method

The subject was asked to hold their breath for as long as possible (~20 sec) at the beginning of the acquisition and to breathe regularly for the rest of the experiment. As illustrated in Figure 7.23, taking a deep breath can induce a motion as large as 2 mm in the anterior-posterior direction. Small but significantly consistent displacements that correlated with the respiratory cycle were observed. To verify the correlation of respiratory induced motion with the image intensity variations a vector of pixel intensity was obtained across the 100 frames. The correlation coefficient between the intensity vectors and the motion vector across frames was obtained at each pixel.

7.3.2.2 Result

Interestingly, the correlation coefficient map showed higher correlation in the medial frontal regions (Figure 7.24). Based on this map, the brain image was segmented

into four regions and a vector of the mean intensity of each segment was obtained. As illustrated in Figure 7.25, the intensity variations in segment 2 resemble the periodic pattern of the respiratory induced motion (Figure 7.23). Cross covariance functions between the mean intensity vectors of each segment with the motion vector (Figure 7.26) show a greater correlation between the signal variations in segments 1 and 2.

7.3.2.3 Discussion

With the highest correlation on the order of 50%, no conclusions about these observations can be made. Statistical analysis of the confidence interval (CI) are complicated by the fact that the respiratory induced motion does not have a normal distribution. The first hypothesis would be that breathing results in variations in the field homogeneity and thus results in small phase fluctuations that translate into small displacements calculated by the phase analysis algorithm of the navigator echo technique. As the anatomical image (Figure 7.24) and results of Figure 7.25(c) reveal, the lowest correlation coefficient is observed in segment 4 that includes the nasal cavities while the highest correlation belonged to segments 1 and especially, 2 that have more structure and include parts of the ventricles. Based on this observation it may be speculated that the higher sensitivity of these regions to respiratory induced phase variations is a result of brain dilation due to CSF pulsation and since these areas encompass the large ventricles, the displacements are larger than in S3 region. One great potential of navigator based motion detection would be to obtain the parameters of motion between different slices of a whole brain image from which a vector field representing the direction and speed of brain dilation can be deduced.

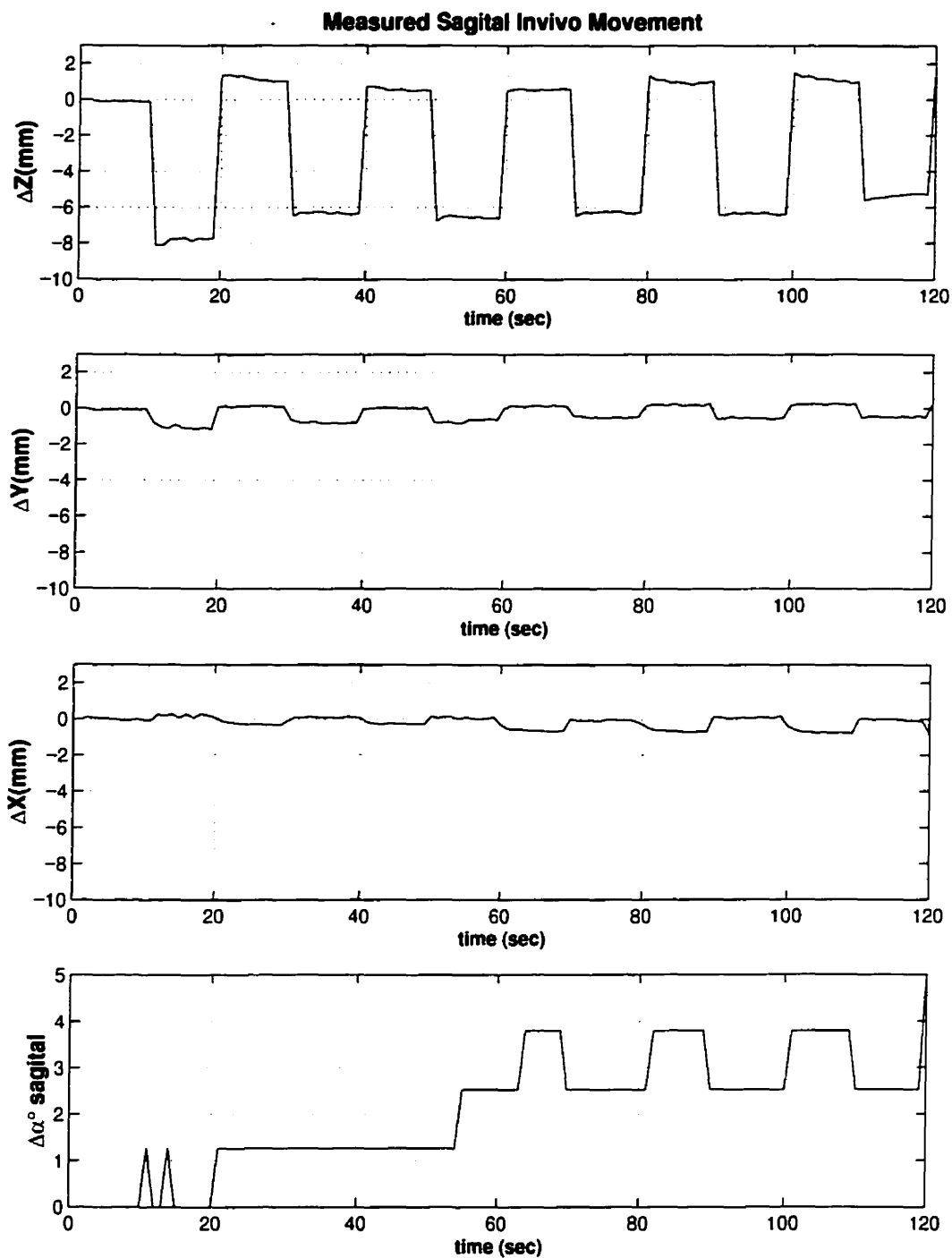
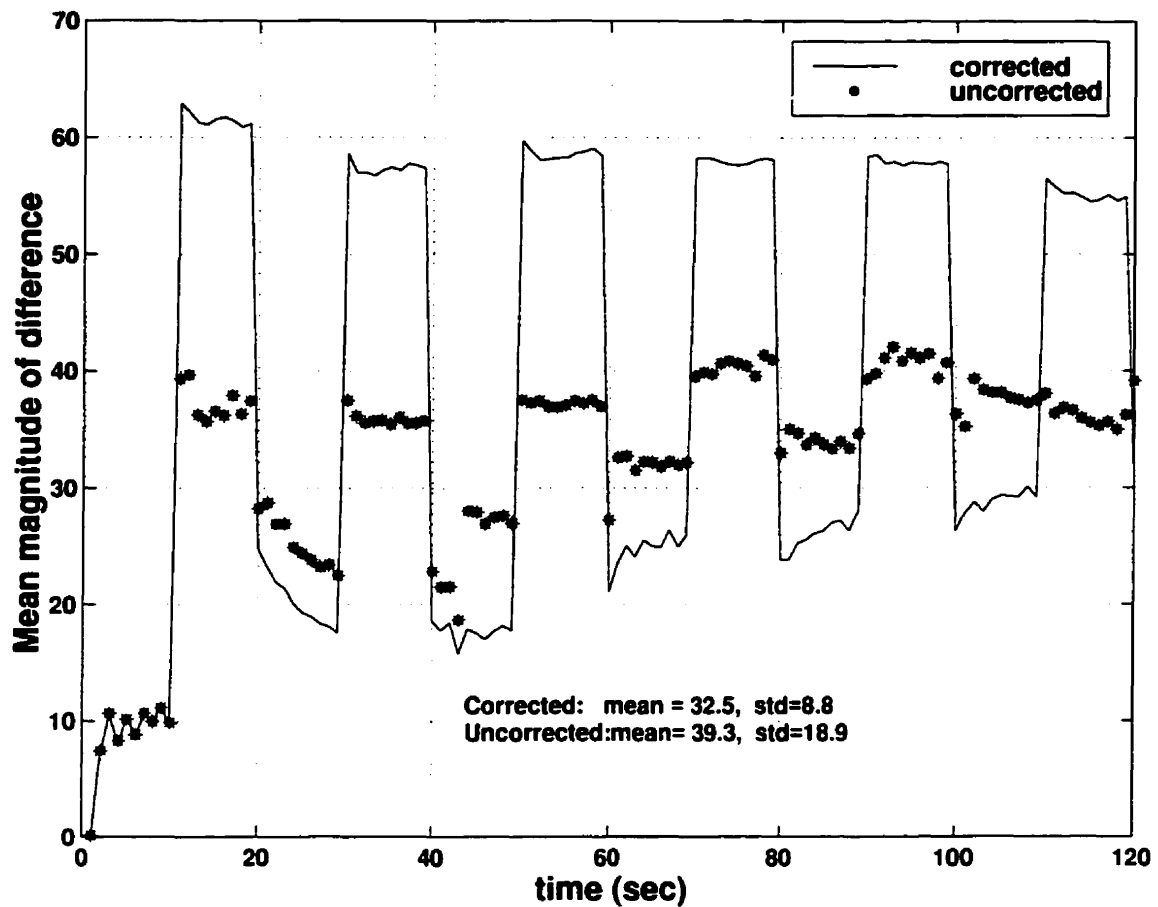
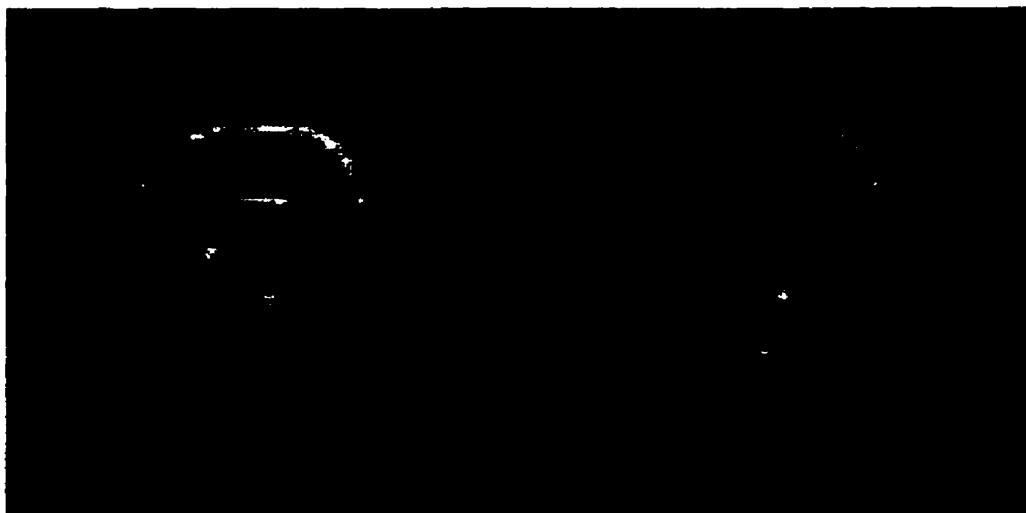


Figure 7:20 Measurements of sagittal movements of the subject inside the magnet. The subject moved in 10-second intervals. The rotations in sagittal plane represent the small nodding movements of the head.



7.21 The effectiveness of motion correction is represented in terms of the mean of the magnitude of the error obtained from subtraction images, before and after correction.



7.22 An example of the difference images before and after correction. The corrections were performed by the method of phase demodulation.

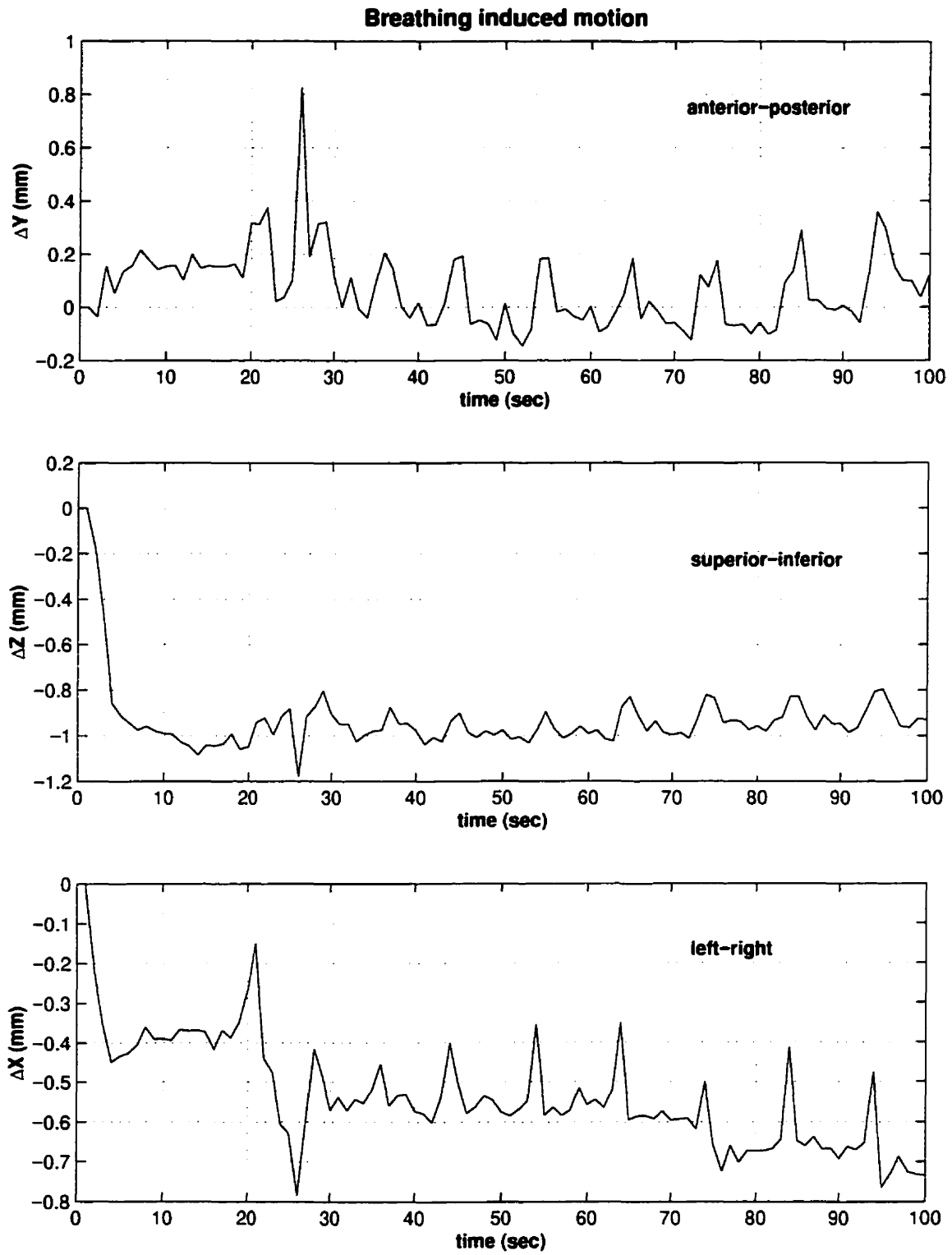
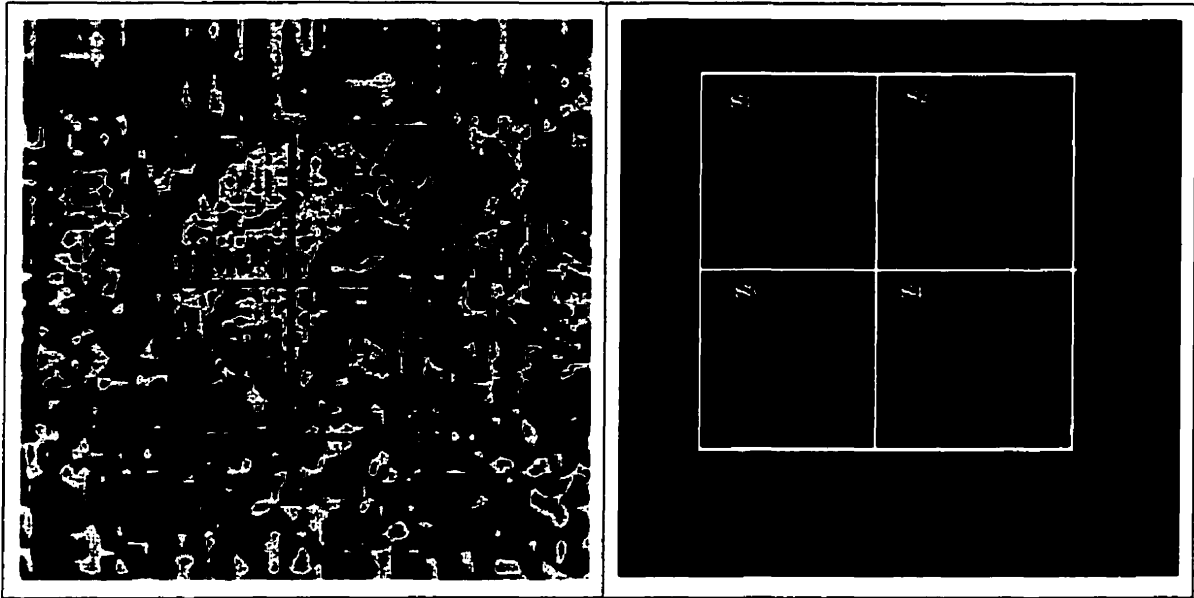
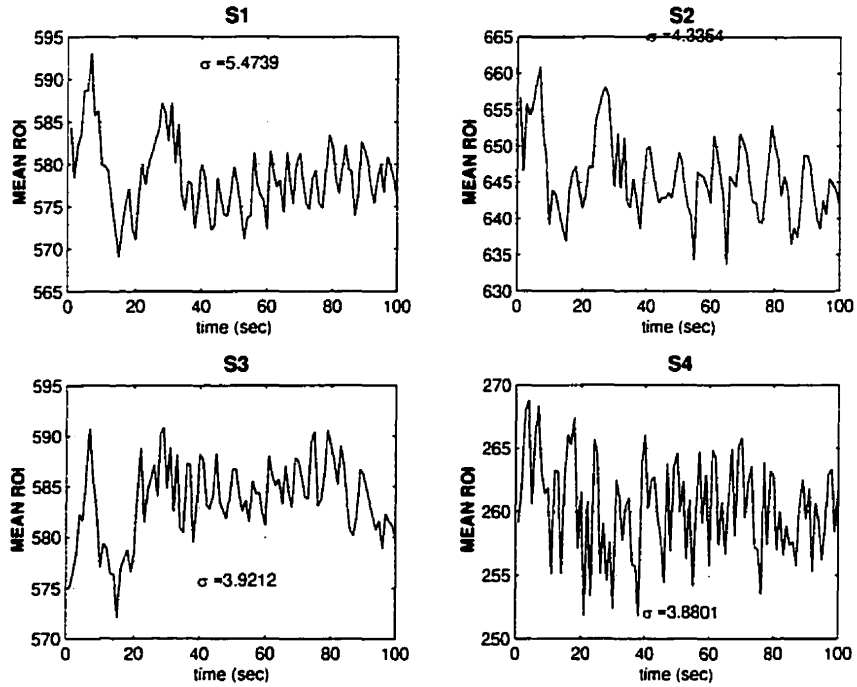


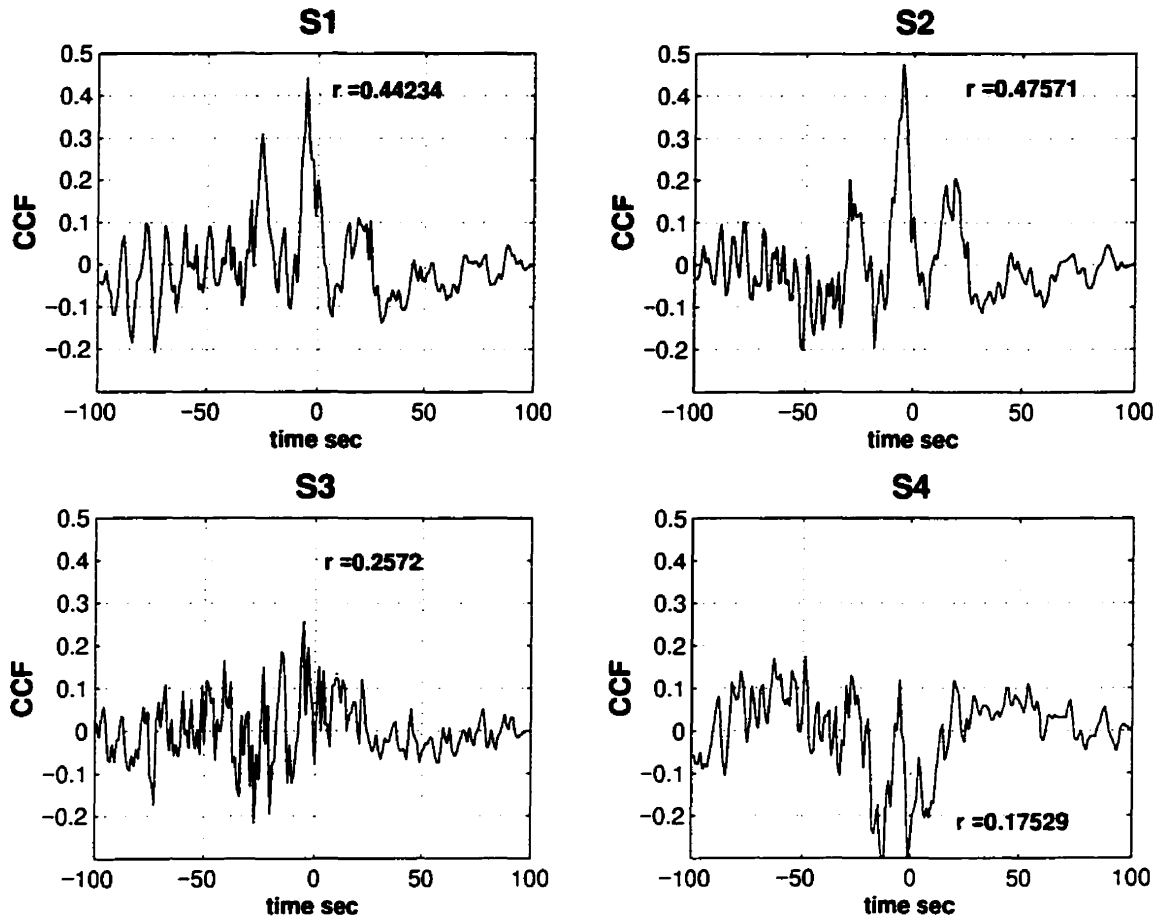
Figure 7.23: Small motion of brain during respiration. The subject was asked to hold her breath for the first 20 measurements.



7.24 (a) Correlation coefficient map. Different anatomical segments over which the correlation of the mean of the image intensity with respiratory cycle were tested are illustrated.



(b) The mean of intensity of 100 frames is plotted separately. Segment 2 shows a periodic pattern of intensity variation among frames while the variations of segment 4 are on the order of noise.



(c) Covariance functions of intensity variations (Figure 7.24 b) and magnitude sum of all displacements indicates ~40% correlation between the intensity variations of segments 1 and 2.

Chapter 8

CONCLUSION

8.1 Summary

A novel 3D orbital navigator pulse sequence was designed and implemented to address the problem of inter-view motion in an EPI sequence. The most important parameters in the design of the navigator echoes were its SNR and speed. To comply with the speed requirements of fMRI (~100 ms per frame), the navigator echoes must not have significantly affected the EPI acquisition time; this necessitated that the volume excitation, formation and the sampling of the orbital trajectories be complete in a few milliseconds.

We proposed that, instead of selective excitations in three orthogonal planes, a single, non-selective low angle rectangular RF pulse be used to excite the spin volume, after which the continuous gradient echoes are formed and sampled immediately, in order to minimize the signal loss due to T2 decay. This design not only reduced the navigator echo time by an order of three, but also avoided slice specific saturation effects that degrade the homogeneity of the image intensity, an effect highly undesirable in fMRI. However, since the timing constraints do not allow enough delay between the navigator and the EPI echoes for complete magnetization recovery, a global reduction of signal

intensity is inevitable. Having examined the image intensity variation with the angle of the navigator excitation versus the SNR of the navigator signal, a 20° RF pulse was chosen.

The second design issue was the determination of the optimal radius of the orbital navigator trajectories. While higher radii of k-space contain more spatial features than are essential for motion measurements, they have lower SNR. A k-space orbital radius of 22.139 ($\sim 7/\text{FOV}$) was found to provide sufficient SNR and phase stability at all azimuth angles.

The stability of the motion estimation algorithms were tested by means of numerical simulation of the Fourier shift and rotation theorems. It was found that the displacement algorithm is robust in the presence of noise while it results in quantized errors in the rotation measurements. Because of the torque generated through-plane displacements during large angle rotation in phantom experiments, the Fourier rotation theorem did not hold beyond 30° . In general, phantom experiments provided accurate measurements of displacement in the range of $\sim 1.5\text{-}30$ mm (rms error = 0.37 mm), and rotations between $5^\circ\text{-}31^\circ$ (rms error = 0.35°); beyond this displacement range, the phantom would move out of FOV and the torque or imperfections in the center of the orbital gradient field would change the shape of the magnitude of the navigators thus making the measurements of rotation inaccurate and unstable.

Preliminary in-vivo experiments were performed to test the sensitivity of the navigator echoes to human subject gross and respiratory induced movements. The technique provided an efficient way of detecting translations and rotations as the subject executed periodical sagittal movements inside the magnet. Furthermore, the usefulness of navigator measurements as a means of monitoring respiratory cycle was demonstrated and correlation coefficient maps of image intensity variation with the respiratory movements were obtained. Interestingly, it was observed that the respiratory motion does not uniformly correlate with the global intensity variations across the image. This observation opens the door to further research about the statistical significance of anatomically variant correlation of the motion with the image intensity.

8.2 Future Work

The present design of the orbital navigators does not provide accurate measurement of the motion beyond the planes of the navigator trajectories. Spiral navigator trajectories - given the high gradient performance of the MRI scanner presently available - can increase the degrees of freedom in estimation of motion parameters. A potential source of error in correct implementation of navigator echoes is the non-ideal gradient performance that could shift the center of the orbital trajectory from its expected hermitian symmetry. A calibration mechanism that accounts for gradient imperfections would increase the accuracy of measurements.

The displacement correction implemented in this thesis are based on Fourier shift theorem that is largely independent of the image pixel size. The image resampling based on linear interpolation that is used for correction of rotation can be improved by cubic interpolation or spline resampling techniques.

The potential usefulness of navigator-based motion correction in fMRI is yet to be fully tested, especially for monitoring the stimulus correlated motion, eye movements and respiratory induced motion. However, based on the fundamental experiments conducted here, positive results are confidently predicted.

As the current MR system will be soon upgraded, the real-time capabilities of the new system will make navigators indispensable to motion tracking that enables re-adjustment of the slice position during acquisition of a moving structure.

Over all, this thesis has demonstrated the potential of the navigator-based motion compensation to become a routine protocol in EPI acquisitions for the present fMRI studies.

REFERENCES

1. Bushberg, J.T., et al., *Magnetic Resonance Imaging*, in *THE ESSENTIALS of MEDICAL IMAGING*. 1994, Williams & Wilkins: bALTIMORE, pHILADELPHIA, Hong Kong, London, Munich, Sydney, Tokyo. p. 291-366.
2. Nishimura, D.G., *PRINCIPLES of MAGNETIC RESONANCE IMAGING*. 1996: Stanford University.
3. Clarke, D.D. and L. Sokoloff, *BASIC NEUROCHEMISTRY*, ed. G. Seigel, L. and B.W. Agranoff. 1994, New Yourk: Raven. 660-680.
4. Fox, P.T. and M.E. Raichle, *Focal physiological uncoupling of cerebral blood flow and oxidative metabolism during somatosensory stimulation in human subjects*. Proc Natl Acad Sci U S A, 1986. 83(4): p. 1140-4.
5. Fox, P.T., et al., *Nonoxidative glucose consumption during focal physiologic neural activity*. Science, 1988. 241(4864): p. 462-4.
6. Buxton, R.B. and L.R. Frank, *A model for the coupling between cerebral blood flow and oxygen metabolism during neural stimulation*. J Cereb Blood Flow Metab, 1997. 17(1): p. 64-72.
7. Davis, T.L., et al., *Calibrated functional MRI: mapping the dynamics of oxidative metabolism*. Proc Natl Acad Sci U S A, 1998. 95(4): p. 1834-9.
8. Hoge, R.D., et al., *Investigation of BOLD signal dependence on cerebral blood flow and oxygen consumption: the deoxyhemoglobin dilution model*. Magn Reson Med, 1999. 42(5): p. 849-63.
9. Hoge, R.D., et al., *Linear coupling between cerebral blood flow and oxygen consumption in activated human cortex*. Proc Natl Acad Sci U S A, 1999. 96(16): p. 9403-8.
10. Silverthorn, D.U., *An integrated approach to human physiology*. 1998, New Jersey: Prentice Hall.
11. Sanders, J.A. and W.W. Orrison, *Functional Magnetic resonance Imaging*, in *Functional Brain Imaging*, W.W. Orrison, et al., Editors. 1995, Mosby: St Louis, Baltimore, ... p. 239-326.

12. Haacke, E.M., et al., *MAGNETIC RESONANCE IMAGING, Physical Principles and Sequence Design*. 1999, New York: Wiley-Liss.
13. Moonen, C.T.W. and P.A. Bandettini, eds. *Functional MRI*. Medical Radiology, ed. A.L. Beart, F.H.W. Heuck, and J.E. Youker. 1998.
14. Ogawa, S. and T.M. Lee, *Magnetic resonance imaging of blood vessels at high fields: in vivo and in vitro measurements and image simulation*. *Magn Reson Med*, 1990. 16(1): p. 9-18.
15. Glover, G.H., *Gradient Echo Imaging*, in *THE PHYSICS OF MRI*, M.J. Bronskill and P. Sprawls, Editors. 1992, American association of physicists in medicine. p. 188-205.
16. Axel, L., *Blood flow effects in magnetic resonance imaging*. *AJR Am J Roentgenol*, 1984. 143(6): p. 1157-66.
17. Fisel, C.R., et al., *MR contrast due to microscopically heterogeneous magnetic susceptibility: numerical simulations and applications to cerebral physiology*. *Magn Reson Med*, 1991. 17(2) p. 336-47.
18. Bandettini, P.A., et al. *Simultaneous mapping of activation induced delta-R-2 and Delta-R2-star in the human brain using a combined GE and SE pulse sequence*. in *12th annual SMRM meeting*. 1993. New York.
19. Ogawa, S., D.W. Tank, and M. R. *Level dependent T2-star rate estimated with a simple biophysical model*. in *12th annual SMRM meeting*. 1993. New York.
20. Wu, D.H., J.S. Lewin, and J.L. Duerk, *Inadequacy of motion correction algorithms in functional MRI: role of susceptibility-induced artifacts*. *J Magn Reson Imaging*, 1997. 7(2): p. 365-70.
21. Jezzard, P. *Intrinsic Magnetic Field Distortions Caused by Head Motion in Functional Magnetic Resonance Imaging*. in *ISMRM, Eighth meeting*. 1999. Denver, CO.
22. Hajnal, J.V., et al., *Artifacts due to stimulus correlated motion in functional imaging of the brain*. *Magn Reson Med*, 1994. 31(3): p. 283-91.
23. Raj, D., et al. *The Role of Physiological Noise in fMRI*. in *Workshop, Understanding the BOLD Phenomena and its Applications*. 2000. Raleigh-Durham, North Carolina.
24. Noll, D.C. and W. Schneider. *Respiration Artifacts in Functional Brain Imaging: Source of Signal Variation and Compensation Strategies*. in *SMR second meeting*. 1994. San Francisco, CA, USA.
25. Ryner, L.N., et al. *Widespread Respiration-Correlated Signal Changes in BOLD*

fMRI of Resting Brain. in ISMRM, Eighth meeting. 2000. Denver, CO.

26. Chen, W., et al. *A robust Device for Monitoring Head Movements during Functional MRI studies*. in SMR/ESMRMB Joint meeting. 1995.
27. Felmlee, J.P., et al., *Adaptive motion compensation in MRI: accuracy of motion measurement*. Magn Reson Med, 1991. 18(1): p. 207-13.
28. Hedley, M. and H. Yan, *Motion artifact suppression: a review of post-processing techniques*. Magn Reson Imaging, 1992. 10(4): p. 627-35.
29. Macgowan, C.K. and M.L. Wood, *Phase-encode reordering to minimize errors caused by motion*. Magn Reson Med, 1996. 35(3): p. 391-8.
30. Ehman, R.L. and J.P. Felmlee, *Flow artifact reduction in MRI: a review of the roles of gradient moment nulling and spatial presaturation*. Magn Reson Med, 1990. 14(2): p. 293-307.
31. Wood, M.L. and R.M. Henkelman, *MR image artifacts from periodic motion*. Med Phys, 1985. 12(2): p. 143-51.
32. Le, T.H. and X. Hu, *Retrospective estimation and correction of physiological artifacts in fMRI by direct extraction of physiological activity from MR data*. Magn Reson Med, 1996. 35(3): p. 290-8.
33. Langenberger, K.W. and E. Moser, *Nonlinear motion artifact reduction in event-triggered gradient-echo FMRI*. Magn Reson Imaging, 1997. 15(2): p. 163-7.
34. Glover, G.H. and A.T. Lee, *Motion artifacts in fMRI: comparison of 2DFT with PR and spiral scan methods*. Magn Reson Med, 1995. 33(5): p. 624-35.
35. Hu, X., et al., *Retrospective estimation and correction of physiological fluctuation in functional MRI*. Magn Reson Med, 1995. 34(2): p. 201-12.
36. Chen, W. and X.H. Zhu, *Suppression of physiological eye movement artifacts in functional MRI using slab presaturation*. Magn Reson Med, 1997. 38(4): p. 546-50.
37. Korin, H.W., et al., *Altered phase-encoding order for reduced sensitivity to motion in three-dimensional MR imaging*. J Magn Reson Imaging, 1992. 2(6): p. 687-93.
38. Wang, Y., et al., *Algorithms for extracting motion information from navigator echoes*. Magn Reson Med, 1996. 36(1): p. 117-23.
39. Felblinger, J. and C. Boesch, *Amplitude demodulation of the electrocardiogram signal (ECG) for respiration monitoring and compensation during MR examinations*. Magn Reson Med, 1997. 38(1): p. 129-36.

40. Wood, M.L., M.J. Shivji, and P.L. Stanchev, *Planar-motion correction with use of K-space data acquired in Fourier MR imaging*. J Magn Reson Imaging, 1995. 5(1): p. 57-64.
41. Duerk, J.L. and O.P. Simonetti, *Theoretical aspects of motion sensitivity and compensation in echo-planar imaging*. J Magn Reson Imaging, 1991. 1(6): p. 643-50.
42. Bruning, R., et al., *[Echo-planar imaging of the brain]*. Radiologe, 1995. 35(12): p. 902-10.
43. Runge, V.M. and M.L. Wood, *Fast imaging and other motion artifact reduction schemes: a pictorial overview*. Magn Reson Imaging, 1988. 6(5): p. 595-607.
44. Haacke, E.M. and J.L. Patrick, *Reducing motion artifacts in two-dimensional Fourier transform imaging*. Magn Reson Imaging, 1986. 4(4): p. 359-76.
45. Wood, M.L., V.M. Runge, and R.M. Henkelman, *Overcoming motion in abdominal MR imaging*. AJR Am J Roentgenol, 1988. 150(3): p. 513-22.
46. Korin, H.W., et al., *Adaptive technique for three-dimensional MR imaging of moving structures*. Radiology, 1990. 177(1): p. 217-21.
47. Ehman, R.L. and J.P. Felmlee, *Adaptive technique for high-definition MR imaging of moving structures*. Radiology, 1989. 173(1): p. 255-63.
48. Felmlee, J.P., et al., *Adaptive motion compensation in MR imaging without use of navigator echoes*. Radiology, 1991. 179(1): p. 139-42.
49. Biswal, B., A.E. DeYoe, and J.S. Hyde, *Reduction of physiological fluctuations in fMRI using digital filters*. Magn Reson Med, 1996. 35(1): p. 107-13.
50. Pattany, P.M., et al., *Motion artifact suppression technique (MAST) for MR imaging*. J Comput Assist Tomogr, 1987. 11(3): p. 369-77.
51. Duerk, J.L., et al., *Multiecho multimoment refocussing of motion in magnetic resonance imaging: MEM-MO-RE*. Magn Reson Imaging, 1990. 8(5): p. 535-41.
52. Duerk, J.L., O.P. Simonetti, and G.C. Hurst, *Modified gradients for motion suppression: variable echo time and variable bandwidth*. Magn Reson Imaging, 1990. 8(2): p. 141-51.
53. Urchuk, S.N. and D.B. Plewes, *Mechanisms of flow-induced signal loss in MR angiography*. J Magn Reson Imaging, 1992. 2(4): p. 453-62.
54. Bailes, D.R., et al., *Respiratory ordered phase encoding (ROPE): a method for reducing respiratory motion artefacts in MR imaging*. J Comput Assist Tomogr, 1985. 9(4): p. 835-8.

55. Kim, W.S., et al., *Extraction of cardiac and respiratory motion cycles by use of projection data and its applications to NMR imaging*. Magn Reson Med, 1990. 13(1): p. 25-37.
56. Glover, G.H. and J.M. Pauly, *Projection reconstruction techniques for reduction of motion effects in MRI*. Magn Reson Med, 1992. 28(2): p. 275-89.
57. Kruger, D.G., et al., *An orthogonal correlation algorithm for ghost reduction in MRI*. Magn Reson Med, 1997. 38(4): p. 678-86.
58. Wood, M.L. and Q.S. Xiang. *Motion Artifacts and Remedies*. in *1992 AAPM Summer School Proceedings*. 1992: American Association of Physicists in Medicine.
59. Ehman, R.L., et al., *Magnetic resonance imaging with respiratory gating: techniques and advantages*. AJR Am J Roentgenol, 1984. 143(6): p. 1175-82.
60. Lanzer, P., et al., *Cardiac imaging using gated magnetic resonance*. Radiology, 1984. 150(1): p. 121-7.
61. Korin, H.W., et al., *Compensation for effects of linear motion in MR imaging*. Magn Reson Med, 1989. 12(1): p. 99-113.
62. Hedley, M. and H. Yan, *An algorithm for the suppression of translational motion artifacts in MRI*. Australas Phys Eng Sci Med, 1990. 13(4): p. 177-84.
63. Zoroofi, R., et al., *An Improved Method for MRI Artifact Correction due to Translational Motion in the Imaging Plane*. IEEE Trans Med Imaging, 1995. 14(3): p. 471-479.
64. Lauzon, M.L. and B.K. Rutt, *Generalized K-space analysis and correction of motion effects in MR imaging*. Magn Reson Med, 1993. 30(4): p. 438-46.
65. Zang, L.H., et al., *Correction of translational motion artifacts in multi-slice spin-echo imaging using self-calibration*. Magn Reson Med, 1993. 29(3): p. 327-34.
66. Gull, S. and G. Daniell, *Image Reconstruction from incomplete and noisy data*. Nature, 1978. 272: p. 686-690.
67. Atkinson, D., et al., *Automatic correction of motion artifacts in magnetic resonance images using an entropy focus criterion*. IEEE Trans Med Imaging, 1997. 16(6): p. 903-10.
68. Atkinson, D., et al., *Automatic compensation of motion artifacts in MRI*. Magn Reson Med, 1999. 41(1): p. 163-70.
69. Kim, B., et al., *Mutual information for automated unwarping of rat brain autoradiographs*. Neuroimage, 1997. 5(1): p. 31-40.

70. McGee, K.P., et al., *Image metric-based correction (autocorrection) of motion effects: analysis of image metrics*. J Magn Reson Imaging, 2000. 11(2): p. 174-81.
71. Price, J.H. and D.A. Gough, *Comparison of phase-contrast and fluorescence digital autofocus for scanning microscopy*. Cytometry, 1994. 16(4): p. 283-97.
72. Sachs, T.S., et al., *The diminishing variance algorithm for real-time reduction of motion artifacts in MRI*. Magn Reson Med, 1995. 34(3): p. 412-22.
73. Mathiak, K. and S. Posse, *Evaluation of motion and realignment for functional magnetic resonance imaging in real time*. Magn Reson Med, 2001. 45(1): p. 167-71.
74. Korin, H.W., et al., *Spatial-frequency-tuned markers and adaptive correction for rotational motion*. Magn Reson Med, 1995. 33(5): p. 663-9.
75. Fu, Z.W., et al., *Orbital navigator echoes for motion measurements in magnetic resonance imaging*. Magn Reson Med, 1995. 34(5): p. 746-53.
76. Welch, E.B., et al. *Spherical Navigator Echoes for 3-D Rigid Body Motion Detection*. in *9th ISMRM-FSMRMB joint annual meeting*. 2001. Glasgow.
77. Ordidge, R.J., et al., *Correction of motional artifacts in diffusion-weighted MR images using navigator echoes*. Magn Reson Imaging, 1994. 12(3): p. 455-60.
78. Anderson, A.W. and J.C. Gore, *Analysis and correction of motion artifacts in diffusion weighted imaging*. Magn Reson Med, 1994. 32(3): p. 379-87.
79. de Crespigny, A.J., et al., *Navigated diffusion imaging of normal and ischemic human brain*. Magn Reson Med, 1995. 33(5): p. 720-8.
80. Ulug, A.M., P.B. Barker, and P.C. van Zijl, *Correction of motional artifacts in diffusion-weighted images using a reference phase map*. Magn Reson Med, 1995. 34(3): p. 476-80.
81. Butts, K., et al., *Diffusion-weighted interleaved echo-planar imaging with a pair of orthogonal navigator echoes*. Magn Reson Med, 1996. 35(5): p. 763-70.
82. Anderson, A.W. and J.C. Gore. *Using Spiral Navigator Echoes to Correct for Motion in Diffusion Weighted Imaging*. in *joint meeting SMR and ESMRMB*. 1995. Nice, France.
83. Butts, K., et al., *Isotropic diffusion-weighted and spiral-navigated interleaved EPI for routine imaging of acute stroke*. Magn Reson Med, 1997. 38(5): p. 741-9.
84. Mori, S. and P.C. van Zijl, *A motion correction scheme by twin-echo navigation for diffusion-weighted magnetic resonance imaging with multiple RF echo acquisition*. Magn Reson Med, 1998. 40(4): p. 511-6.

85. Norris, D.G. and W. Driesel, *Online motion correction for diffusion-weighted imaging using navigator echoes: Application to RARE imaging without sensitivity loss*. Magn Reson Med, 2001. 45(5): p. 729-33.
86. Hu, X. and S.G. Kim, *Reduction of signal fluctuation in functional MRI using navigator echoes*. Magn Reson Med, 1994. 31(5): p. 495-503.
87. Lee, C.C., et al., *Real-time adaptive motion correction in functional MRI*. Magn Reson Med, 1996. 36(3): p. 436-44.
88. Lee, C.C., et al., *A prospective approach to correct for inter-image head rotation in fMRI*. Magn Reson Med, 1998. 39(2): p. 234-43.
89. Ward, H.A., et al., *Prospective multiaxial motion correction for fMRI*. Magn Reson Med, 2000. 43(3): p. 459-69.
90. Brummer, M.E., et al. *Reduction of respiratory Motion Artifacts in Coronary MRA using Navigator Echoes*. in *SMR/ESMRMB joint meeting*. 1995. Nice, France.
91. Wang, Y., et al., *Navigator-echo-based real-time respiratory gating and triggering for reduction of respiration effects in three-dimensional coronary MR angiography*. Radiology, 1996. 198(1): p. 55-60.
92. Wirestam, R., et al. *Improvement in brain-motion measurements using navigator-echo techniques*. in *SMR /ESMRMB Joint meeting*. 1995. Nice, France.
93. van der Veen, J.W.C. *Characterization of brain motion with a 3D navigator and reduction of motion artifacts in PRESTO*. in *ISMRM Fifth scientific meeting*. 1997. Vancouver, BC, Canada.
94. Butts, K., A. de Crespigny, and M. Moseley. *Diffusion-Weighted Interleaved EOI with Navigation for Stroke Imaging*. in *joint meeting SMR and ESMRMB*. 1995. Nice, France.
95. Thedens, D.R. and D.G. Nishimura. *Respiratory Motion Compensation with a Self-Navigated Trajectory*. in *ISMRM Seventh scientific meeting*. 1999. Philadelphia, PA.
96. Nehrke, K. and P. Bornert. *Study of Respiratory Motion of the Heart using Multiple Navigator Pulses*. in *ISMRM Eight scientific meeting*. 2000. Denver, CO, USA.
97. Wirestam, R., et al., *Quantification of low-velocity motion using a navigator-echo supported MR velocity-mapping technique: application to intracranial dynamics in volunteers and patients with brain tumours*. Magn Reson Imaging, 1997. 15(1): p. 1-11.
98. Collins, D.L., et al., *Automatic 3D intersubject registration of MR volumetric data in standardized Talairach space*. J Comput Assist Tomogr, 1994. 18(2): p. 192-205.